Submitted to Physical Review

LBL-997
Preprint

ANALYSIS OF TWO-PRONG EVENTS IN PROTON-PROTON INTERACTIONS AT 6.6 GeV/c

Eugene Colton, Z. Ming Ma,
Gerald A. Smith, and Peter E. Schlein

July 1972

AEC Contract No. W-7405-eng-48

LBL-997

DISCLAIMER

LBL 997

ANALYSIS OF TWO-PRONG EVENTS IN PROTON-PROTON INTERACTIONS AT 6.6 GeV/c*

Eugene Colton

Lawrence Berkeley Laboratory
University of California, Berkeley 94720

and

Z. Ming Ma and Gerald A. Smith

Department of Physics
Michigan State University
East Lansing, Michigan 48823

and

Peter E. Schlein

Department of Physics
University of California
Los Angeles, CA. 90024

July, 1972

ABSTRACT

A detailed analysis is presented of the reactions $pp \to pp$, $pp \to pp\pi^0$, and $pp \to p\pi^+n$. The production cross sections are found to be 11.47 ± 0.33 mb, 2.54 ± 0.16 mb, and 5.73 ± 0.35 mb, respectively. The t dependence of elastic scattering can be described by the form $\exp(7.9t)$ over the range $0.05 < -t < 0.50$ GeV . The single particle distributions for the single-pion production processes are presented. Further detailed analyses are presented which demonstrate that pion-exchange phenomenology, both elementary and Reggeized, can account for the gross features of the peripheral $pp \to p\pi^+n$ data for $M(p\pi^+) < 2.4$ GeV. Isospin 1/2 isobars are produced by some other processes in the channel $pp \to pN^{*+}$, especially when the invariant mass of the pion with the unrelated proton is large. We discuss the properties of these isobars.

I. INTRODUCTION

In this work we report our analysis of elastic scattering and single pion production in proton-proton collisions at 6.6 GeV/c. Analyses at other beam momenta in the range 2.8 to 28.5 GeV/c have already been presented.[1] This analysis is based on studies of the reactions

$$pp \rightarrow pp \qquad (1.1)$$

$$pp \rightarrow pp \qquad (1.2)$$

and $$pp \rightarrow p\pi^+ n \qquad (1.3)$$

We study the elastic scattering process (1.1) in order to obtain the total and differential cross sections. The reaction (1.2) and (1.3) data are analysed primarily to obtain clues to the identity of the dynamical single-pion production mechanism. In addition, we present the data in as complete a form as possible because of their size and clear utility to theoretical analyses.

Within our analysis we extend our earlier pole-extrapolation results[2] of reaction (1.3) to an invariant $p\pi^+$ mass of 2.02 GeV. We indicate in detail how our techniques can be applied to obtain dependable results in pion-producing reactions, e.g., $\pi\pi$ or $K\pi$ scattering cross sections from $\pi p \rightarrow \pi\pi N$ or $Kp \rightarrow K\pi N$ data. We also summarize our earlier work on a narrow $N^+(1470)$,[3] and Isotopic-spin separations,[4] using the data of reactions (1.2) and (1.3).

In Sec. II we discuss the beam, scanning, and measuring procedures. The subject of elastic scattering is treated in Sec. III; our procedure for correcting for missed events is described. The kinematic separation of

reactions (1.2) and (1.3) is treated in Sec. IVA. Cross section calculations and their dependence upon laboratory beam momenta are presented in Sec. IVB. Legendre series parametrizations of the single-particle center of mass angular distributions are carried out in Sec. IVC.

Reaction (1.3) is studied in detail in Sec. V. Single-particle distributions of the c.m. momenta and four-momentum transfer squared (t) are examined in Sec. VA. The Dalitz plot and its projections are presented in Sec. VB. Detailed two-dimensional studies of the Chew-Low distributions of the π^+p and π^+n systems are put forth in Secs. VC and VD, respectively. The $pp \to \Delta^{++}(1238)n$ t distribution and decay density matrix elements are presented in Sec. VE; a possible production mechanism is suggested. The expanded pole-extrapolation analysis is detailed in Sec. VF for peripheral neutron production; reasonable π^+p elastic scattering cross sections are obtained. In Sec. VG a detailed peripheral analysis is presented for the data in three $M(p\pi^+)$ bins; corresponding predictions of several theoretical models are exhibited.

The work of Refs. 3 and 4 is discussed in Secs. VIA and VIB, respectively. Our conclusions are stated in Sec. VII. Finally an appendix is included which lists the formulas used to generate the theoretical distributions which are shown in Sec. VG.

II. EXPERIMENTAL PROCEDURES

The events were photographed in the LRL 72-in liquid-hydrogen bubble chamber, which was exposed to the external proton beam[5] from the Bevatron. The separated 6.6 GeV/c beam had a momentum bite of ±0.15% and possessed a small π^+ contamination of less than 0.1%.[6]

Portions of the film were scanned twice for events with two-prong topology. Approximately thirty-eight thousand of these events were measured on the LRL Spiral Reader and UCLA SMP machines. Kinematic fits of the data were attempted to the following hypotheses:

$$pp \rightarrow pp + MM \tag{2.1}$$

$$pp \rightarrow p\pi^+ + MM \tag{2.2}$$

$$pp \rightarrow d\pi^+ \tag{2.3}$$

$$pp \rightarrow d\pi^+\pi^0 \tag{2.4}$$

$$pp \rightarrow d\pi^+ + MM \quad . \tag{2.5}$$

Of course, fits were also attempted to hypotheses (1.1), (1.2) and (1.3). Processes (2.1), (2.2), and (2.5) represent unconstrained missing mass calculations. An analysis of the events representing reactions (2.1) and (2.2) was reported earlier[7] and will not be discussed here. No further work was performed upon reactions (2.3) and (2.4). However, an upper limit of 10 μb was estimated earlier[8] for the production cross section for reaction (2.3).

III. ELASTIC SCATTERING

One quarter of all pictures used in this experiment were doubly scanned. The difference between the two scans was resolved in a third scan. The efficiency after two scans was 0.998. Although all events found within a 150 cm long fiducial volume were measured, an examination of the vertex location for those accepted events revealed a significantly lower passing rate for events found near the up- or downstream end of the volume. For the purpose of calculating cross sections, we have used only the doubly-scanned sample found within the middle 60 cm of the fiducial volume. The reduced sample corresponds to 6.91 μb/event.

A second measurement pass was made on the doubly scanned rolls. We have assumed a 100% passing rate for the elastic scattering events after two measurements. For this reduced sample, we have 1227 examples of elastic scatters. In order for an event to be classed as an elastic scatter, it must fit the nominally four-constraint hypothesis of reaction (1.1) with kinematic chi-squared probability (CL) greater than 10^{-5}.

In searching for possible systematic biases in scanning and measuring, we have examined the dip angle distribution for the recoil proton in the laboratory. The dip angle, ϕ, is defined as arc tan (P_z/P_x), where the y-axis runs along the chamber and is approximately parallel to the direction of the beam track and the z-axis is parallel to the magnetic field and perpendicular to the film plane. In Figs. 1(a), 1(b), 1(c), and 1(d) we display the experimental ϕ distributions for elastic scattering events produced with four-momentum transfer squared $|t|$ in the regions 0-0.05 GeV^2, 0.05 - 0.10 GeV^2, 0.10 - 0.15 GeV^2, and 0.15 - 0.20 GeV^2, respectively. Dips, which increase with decreasing $|t|$, are observed at 90° and 270° corresponding to events for which the recoil proton is parallel to the optical path of the

cameras. This group of events constitutes a sample of missing events which cannot be accounted for by assuming a random scanning loss. To compensate for this loss, two methods of correction have been attempted. First, percentage losses have been calculated assuming that the ϕ distribution should be isotropic and that no loss is present within the regions of $\phi = 0° \pm 8°$ and $180° \pm 8°$. Second, the data have been fitted to the form $F(\phi) = a + b\,|\cos\phi|$. In this case, the number of corrected events is given by $2\pi(a + b)$. The two methods have been found to be consistent within statistics. Results from the second method have been used. The solid curves drawn in Fig. 1 represent the above expansion for $F(\phi)$, using for a and b, the best fit values obtained in the least-squares fits to the data in Fig. 1.

To carry out the correction we assign a weight to each event, equal to the inverse of the percentage of events found in scanning for that particular $|t|$ bin. Average weights between $|t| = 0$ and 0.2 GeV^2 in bins of 0.05 GeV^2 are 1.44 ± 0.06, 1.17 ± 0.07, 1.13 ± 0.09 and 1.12 ± 0.11. For $|t| > 0.2$ GeV^2, a single weight is calculated for that sample and is equal to 1.08 ± 0.07. The differential cross sections have been thus corrected and are shown in Fig. 2, with numerical values tabulated in Table I.

It is apparent that the event loss in the first $|t|$ bin ($|t| \leq 0.05$ GeV^2) is still present, and is due to the extreme peripheral events in which the fast proton carries virtually all of the available beam momentum, rendering the recoiling proton undetectable in the bubble chamber. We feel with confidence that the data for $|t|$ greater than 0.05 GeV^2 are free of biases.

The corrected differential cross sections have been fitted to a phenomenological form

$$\frac{d\sigma}{dt} = \left.\frac{d\sigma}{dt}\right|_{t=0} e^{bt} \qquad (3.1)$$

for $0.05 < -t < 0.5$ GeV^2 by means of a least-square method. The fitted slope parameter, b, is 7.94 ± 0.26 GeV^{-2} and the intercept at t=0 is 89.8 ± 5.9 mb/GeV^2. These values are consistent with those observed at nearby beam momenta.[9] Our value of b (the slope parameter) can be associated with the optical-model impact parameter R by the relation

$$R = 2\sqrt{b}\,\hbar c \qquad (3.2)$$

and we find $R = (1.12 \pm 0.02) \times 10^{-13}$ cm.

Using the phenomenological expression for $d\sigma/dt$ [Eq. (3.1)], we estimate the event loss, for $-t < 0.05$ GeV^2, and thus obtain a value of 11.47 ± 0.33 mb for the total pp elastic scattering cross section at 6.6 GeV/c. Further, using the known[10] total pp cross section in this momentum region we find our t = 0 intercept [from Eq. (3.1)] corresponds to a value of 0.26 ± 0.13 for $|\alpha|$, the absolute value of the real to imaginary amplitude. This value for $|\alpha|$ is consistent with the value of 0.33 obtained by Foley et al.[11]

IV. ONE CONSTRAINT HYPOTHESES

A. Kinematic Separation

Candidates for reactions (1.2) and (1.3) must first fit the corresponding hypotheses with kinematic chi-squared probability (CL) $\geq 10^{-5}$. In addition, no four-constraint fits [e.g., (1.1) or (2.3) with CL $\geq 10^{-5}$] should be made simultaneously with the one-constraint fit. Further, for an event to be accepted as the type (1.2)/(1.3) the sum of chi-squared probabilities of kinematic and ionization fits for reaction (1.2)/(1.3) must be greater than than for reaction (1.3)/(1.2). In this way we obtained a total sample of 2591 events of the type $pp \to pp\pi^0$.

In the case of reaction (1.3) still another requirement is imposed: If the event was measured on the Spiral Reader and the neutron from the $p\pi^+n$ fit propagates in the backward hemisphere in the center of mass (c.m.) system, then the fit is accepted if the outgoing proton c.m. cosine is greater than -0.8. This procedure effectively removes the gross contamination from the reaction $pp \to p\pi^+n\pi^0$. We believe that the events accepted as examples of reaction (1.3) are really 97% pure $pp \to p\pi^+n$ with a 3% contamination from $pp \to p\pi^+n\pi^0$ and reaction (1.2). These percentages are based mainly on the degree of symmetry of the single particle c.m. angular distributions (which are displayed in Fig. 7). Finally, in order to achieve a narrow spectrum in c.m. energy, we require the fitted beam momentum in the $p\pi^+n$ fit to be between 6.38 and 6.78 GeV/c at the interaction vertex; this final cut reduces the sample to 6424 events of the type $pp \to p\pi^+n$ at 6.6 GeV/c.

B. Production Cross Section Determination

The experimental missing-mass-squared distribution for the 2591 events accepted to be examples of reaction (1.2) is displayed in Fig. 3. The distribution is expected to be symmetric about the π^0 mass squared [μ^2]. The slight excess on the high side of the π^0 signal is interpreted to be due to the $2\pi^0$ state; thus we folded the distribution around μ^2 in order to evaluate the cross section. The asymmetric excess corresponding to 264 events is shaded in Fig. 3. We thus obtain a value of 2.54 ± 0.16 mb for the cross section for $pp \rightarrow pp\pi^0$ at 6.6 GeV/c. This result is consistent with values obtained in other experiments[1] at nearby incident beam momenta. Figure 4 displays the experimental cross section for reaction (1.2) (plotted on a log-log scale) as a function of beam momentum.

The production cross section for reaction (1.3) is found to be 5.73 ± 0.35 mb. This number is consistent with values obtained in other experiments[1] at nearby incident beam momenta. Figure 5 displays the experimental cross section for reaction (1.3) (plotted on a log-log scale) as a function of beam momentum. A least-squares fit of the data points in Fig. 5 to the assumed form $\sigma = a(|P_{Lab}|)^b$ yielded a chi-squared (χ^2) of 22.5 (CL ∿ 1%) and best fit values of 45.9 ± 2.1 mb, and -1.06 ± 0.03 for the parameters a and b, respectively. The straight line drawn through the data in Fig. 5 represents the expansion $\sigma = 45.9\ (|P_{Lab}|)^{-1.06}$ mb.

C. c.m. Angular Distributions

The single particle c.m. angular distributions for 2542 $pp \to pp\pi^0$ and the 6424 $pp \to p\pi^+n$ events are exhibited in Figs. 6 and 7, respectively. In each case the angle referred to is measured between the incoming beam proton and the denoted outgoing particle. These distributions have been fitted to the normalized expression

$$\frac{1}{N}\frac{dN}{d\Omega} = \sum_{L=0}^{L_m} A_L Y_L^0 (\cos\theta) \qquad (4.1)$$

where Y_L^0 is a spherical harmonic function, and L_m represents the maximum L value needed to describe the distribution adequately (CL > 1%). The proton distribution in Fig. 6(a) requires terms to $L_m = 14$, while the π^0 distribution in Fig. 6(b) requires at least $L_m = 7$. In the case of reaction (1.3), the proton [Fig. 7(a)] and neutron [Fig. 7(b)] distributions each require $L_m = 16$, whereas the π^+ distribution [Fig. 7(c)] needs $L_m = 12$.

The forward-backward asymmetry, given by the relation

$$\alpha = \frac{N_F - N_B}{N_F + N_B} \qquad (4.2)$$

is given in Table II for each outgoing particle in reactions (1.2) and (1.3). Deviations from zero for the reaction (1.2) data are due mainly to contamination from the reaction $pp \to pp\pi^0\pi^0$ (see Sec. IV.B above). The small values observed for α for the distributions of reaction (1.3) are due to a combination of statistics and small contaminations (see Sec. IV.A above).

V. FURTHER ANALYSES OF $pp \to p\pi^+n$

A. Single-Particle Distributions

The Peyrou plots of proton, neutron, and π^+ are presented in Figs. 8(a)-8(c), respectively. The corresponding one-dimensional projections are presented in Fig. 9. Figures 9(a)-9(c) display the c.m. transverse momenta , while the folded, normalized longitudinal momenta are plotted in Figs. 9(d)-9(f). The normalized longitudinal momentum of a particle is defined by

$$X = \frac{P_L}{P_{max}} \tag{5.1}$$

where P_{max} is the momentum when the opposing two-particle system recoils with minimum invariant mass. The averaged values of the transverse and longitudinal momenta, and $|X|$ are listed in Table III for each outgoing particle. The nucleons prefer production with simultaneously large values of c.m. longitudinal momenta and small values of transverse momenta; thus, the nucleons prefer emission in fast forward/backward cones of small apex angle about the beam direction. The π^+ prefers equatorial emission in the c.m. with low momentum. For further comparison we show in Figs. 10(a)-10(c) distributions of the averaged transverse momentum $\langle P_T \rangle$ plotted vs. X; the reductions near $X = \pm 1$ are kinematic in origin, while effects near $X = 0$ are dynamically caused.

The overall behavior exhibited in the distributions in Figs. 8-10 is summarized in the longitudinal phase-space plot[12] displayed in Fig. 11. The outer borders of the hexagon represent the limiting case of infinite energy and no transverse momenta. For each event the c.m. longitudinal

momenta measured perpendicularly from the signed diagonal lines for p, n, and π^+ intersect at a single point on the plot. The largest concentrations of events occur with simultaneously large and small magnitudes of nucleon and pion momenta, respectively.

The momentum-transfer distributions of proton, neutron, and π^+ are given in Figs. 12(a) - 12(c), respectively. For reaction (1.3) we define the momentum transfer squared (t) to be

$$t_o = -(P_i - P_o)^2 \tag{5.2}$$

where the P's are four vectors, and i and o refer to an incident proton and an outgoing particle, respectively. The proton and neutron t distributions are folded in Figs. 12(a) and 12(b). For each outgoing nucleon there are two values of t which can be calculated with respect to an incident proton; we use the lower of the two values. This procedure associates an outgoing nucleon with the incident proton which propagates in the same hemisphere in the c.m. system.

Breaks are observed in the t_p distribution [Fig. 12(a)] at 0.7 and 1.8 GeV^2 and in the t_n distribution [Fig. 12(b)] at 0.5 GeV^2. The data on each side of the breaks have been fitted separately to the form $dN/dt = Ae^{yt}$; the resulting confidence levels and best fit parameters are listed in Table IVA. The data for $t_p < 1.8$ GeV^2 and $t_n < 3.0$ GeV^2 have also been fitted to the sum of two exponentials

$$\frac{dN}{dt} = Ae^{yt} + Be^{zt} \tag{5.3}$$

The results of these fits are given in Table IVB. The curves drawn in Figs. 12(a) and 12(b) represent the formula (5.3) using the best fit

values for A, B, y, and z as obtained in the latter least-squares fits. The preference for low-momentum transfer indicates that peripheral (i.e., large-impact parameter) production mechanisms play a major role in these events.

B. Mass Dependences

The Dalitz plot of $M^2(p\pi^+)$ vs. $M^2(\pi^+n)$ is presented in Fig. 13 for the 6424 examples of reaction (1.3); the kinematical boundary corresponds to the central value of c.m. energy (3.772 GeV). Figure 13 is not uniformly populated; the data concentrate at low values of nucleon-pion mass squared. In particular, the dark vertical band indicates production of the $\Delta^{++}(1238)$ resonance in the reaction

$$pp \rightarrow \Delta^{++}(1238)\ n \qquad (5.4)$$

The projections of $M(p\pi^+)$ and $M(\pi^+n)$ are shown in Fig. 14, together with M(pn). The spectrum of Fig. 14(a) exhibits the strong $\Delta^{++}(1238)$ signal; approximately 35% of the events are produced via reaction (5.4).[13] Another enhanced region in Fig. 14(a) stretches from 1.6 to 2.05 GeV. The π^+n mass spectrum, exhibited in Fig. 14(b), possesses a small enhancement at the $\Delta^+(1238)$ position and a broader enhanced region from 1.4 to 1.75 GeV; above 1.75 GeV no significant structure is apparent. The pn mass spectrum in Fig. 14(c) is broadly enhanced at large masses and can be understood in terms of the peripheral nature of the outgoing nucleons.

C. Study of the Chew-Low Distribution of the π^+p System

The Chew-Low plot of $M(p\pi^+)$ vs. t_n is presented in Fig. 15. The heavy concentration of points at low t_n illustrates the highly peripheral nature of the data. In particular, the $\Delta^{++}(1238)$ events are almost entirely produced with small values of t_n.[14] The projections of $p\pi^+$ mass in four ranges of t_n are exhibited in Figs. 16(a)-16(d). These spectra are presented in order to isolate the peripheral components of the enhancements observed in Fig. 14(a), and perhaps to expose new enhancements. No enhancements other than the $\Delta^{++}(1238)$ are present in Figs. 16(a)-16(d).

The t_n projections of Fig. 15 for the 15 denoted ranges of $M(p\pi^+)$ are displayed in Figs. 17(a)-17(o). All of the distributions peak at low values of t_n. Least-squares fits of the data in Figs. 17(a)-17(o) to the assumed form $\exp(a+bt_n+ct_n^2)$ have been performed; the resulting confidence levels and best-fit parameters are listed in Table V. Column 2 lists the range of t_n over which the data were fit; the lower limit of t_n represents the first $[M(p\pi^+),t_n]$ box not cut by the lower kinematical boundary of the Chew-Low contour. All of the fits represented in Table V yield acceptable confidence levels (Col. 3) except for the 1.84-1.96 GeV $M(p\pi^+)$ bin which has CL < 1%. The curves drawn in Figs. 17(a)-17(o) represent the expansion $\exp(a+bt_n+ct_n^2)$, using the best fit values for the parameters a, b, and c.

The best fit values of b and c are plotted in Figs. 18(a) and 18(b), respectively, as a function of $M(p\pi^+)$. Both distributions have a similar shape: They remain roughly constant up to approximately 1.4 GeV and then decrease slowly with increasing mass.

D. Study of the Chew-Low Distribution of the π^+n System

The Chew-Low plot of $M(\pi^+n)$ vs. t_p is presented in Fig. 19. For $M(\pi^+n) < 2.4$ GeV the data concentrate near the lower boundary of the contour; for $M(\pi^+n) < 1.8$ GeV the concentration is especially intense. The projections of π^+n mass in four ranges of t_p are exhibited in Figs. 20(a)-20(d). In Fig. 20(a) the distribution peaks toward low values of $M(\pi^+n)$. The structure flattens in Figs. 20(b)-20(d) and some enhancements are observed: Small bumps are present at the position of the $\Delta^+(1238)$ resonance, and near 1.45 and 1.7 GeV.

The t_p projections of Fig. 19 for the 15 denoted ranges of $M(\pi^+n)$ are displayed in Figs. 21(a)-21(o). All of the distributions peak at low values of t_p. Least-squares fits of the data in Fig. 21 to the assumed form $\exp(a+bt_p+ct_p^2)$ have been performed; the resulting confidence level and best fit parameters are listed in Table VI. Column 2 lists the range of t_p over which the data were fit; the lower limit of t_p represents the first $[M(\pi^+n),t_p]$ box not cut by the lower kinematical boundary of the Chew-Low contour. All of the fits represented in Table VI. yield acceptable confidence levels. The curves drawn in Figs. 21(a)-21(o) represent the expansion $\exp(a+bt_p+ct_p^2)$, using the best fit values for the parameters a, b, and c.

The best fit values of the parameters b and c are plotted in Figs. 22(a) and 22(b), respectively, as a function of $M(\pi^+n)$. Both distributions seem to behave similarly with mass, as was observed in Fig. 18; the behavior appears to be quadratic here, however. Least-squares fits of the data in Fig. 22 to the assumed

quadratic forms $x+yM+zM^2$ have been performed; the resulting confidence levels and best fit parameters are listed in Table VII. The curves drawn in Figs. 22(a) and 22(b) represent the expansion $x+yM+zM^2$, using the best fit values for the parameters x, y, and z.

E. Study of $\Delta^{++}(1238)$ Production

As stated above in Sec. VB, reaction (5.4) accounts for 35% of the reaction (1.3) data at 6.6 GeV/c. In order to assure an enriched sample of $\Delta^{++}(1238)$ events for further study, we select resonant systems by an invariant mass slice, viz.,

$$1.14 < M(p\pi^+) < 1.42 \text{ GeV} \quad . \tag{5.5}$$

The t_n distribution ($d\sigma/dt$) for the events satisfying the cut (5.5) is displayed in Fig. 23 for $t_n < 4.0$ GeV^2. Numerical values are listed in Table VIII.[15] A least-squares fit of the data in Fig. 23 to the sum of two exponentials [Eq.(5.3)] has been performed for $0.02 < t_n < 4.0$ GeV^2. The fit yields a χ^2 of 47.6 for 41 degrees of freedom. Best fit values for the parameters A, B, y, and z are 15.0 ± 0.6 mb/GeV^2, 0.9 ± 0.1 mb/GeV^2, -10.5 ± 0.3 GeV^{-2}, and -1.9 ± 0.1 GeV^{-2}, respectively.

Further information can be obtained about the $\Delta(1238)$ resonance production by studying the decay of the isobar into $p\pi^+$. The decay of a spin-3/2 isobar into a spin-1/2 nucleon and a spin-0 pion is given by the normalized distribution[16]

$$W(\theta,\phi) = \frac{1}{4\pi}\left\{1 + \sqrt{\frac{4\pi}{5}}\,(1-4\rho_{33})\,Y_2^0 - 8\sqrt{\frac{2\pi}{5}}\,(\mathrm{Re}\rho_{3,-1}\,\mathrm{Re}Y_2^2 - \mathrm{Re}\rho_{3,1}\,\mathrm{Re}Y_2^1)\right\} \tag{5.6}$$

where the Y_L^M are spherical harmonic functions with arguments θ and ϕ. θ and ϕ represent the polar and azimuthal angles, respectively, of the decay nucleon expressed in the standard[17] t-channel coordinate system. The ρ_{ij} are the decay density matrix elements. Orthonormality of the Y_L^M functions leads to the determination of the density matrix elements:

$$\rho_{33} = 0.5 - \rho_{11} = \frac{1}{4}\left(1 - \sqrt{20\pi}\,\langle Y_2^0\rangle\right)$$

$$\mathrm{Re}\rho_{3,-1} = -\sqrt{\frac{5\pi}{2}}\,\langle \mathrm{Re}Y_2^1\rangle \qquad (5.7)$$

and

$$\mathrm{Re}\rho_{3,1} = \sqrt{\frac{5\pi}{2}}\,\langle \mathrm{Re}Y_2^2\rangle$$

The density matrix elements are plotted in Figs. 24(a)-24(c) as a function of t_n for $t_n < 1.0$ GeV^2. Numerical values are listed in Table IX. The t-channel coordinate system is depicted in Fig. 24(d). The ρ_{33} and $-\mathrm{Re}\rho_{3,1}$ elements are small and positive, whereas the $\mathrm{Re}\rho_{3,-1}$ are small and consistent with zero, for all $t_n < 1.0$ GeV^2.

Serious interpretation of the reaction (5.4) data is complicated by the presence of a high background content in the Δ^{++} band in the lower-left corner of the Dalitz plot exhibited in Fig. 13. This background (possibly interfering) arises from low-mass π^+n resonances created via e.g., the process depicted inset in Fig. 20(a). Another complication is the presence of partial waves other than $J^P = 3/2^+$ contributing to the polar angular distribution of $\cos\theta$. With regard to interpretation, a simple one-pion-exchange process such as depicted inset in Fig. 16(a), predicts a peripheral t dependence, and zero for the three density matrix elements given by (5.7). However, the consideration of absorption effects[18] modifying the one-pion-exchange can explain the t dependence of the density matrix elements [see,

e.g., Ref. 1 (5.5 GeV/c data)].

F. Pole Extrapolation to Obtain the π^+p Elastic Scattering Cross Section

In this subsection we attempt to show that the peripheral or low-momentum transfer data of reaction (1.3) can be grossly explained by the exchange process inset in Fig. 16(a) with single π^+ exchange. First we compare the angular distributions of scattering [at the upper vertex of the process inset in Fig. 16(a)], evaluated in the π^+p rest system, with known π^+p elastic scattering angular distributions in order to show that they are similar. Pole extrapolation techniques are then used to obtain π^+p elastic scattering cross sections which are in reasonable agreement with known π^+p cross sections over a wide range of $M(p\pi^+)$.

The preference for low momentum transfer to the outgoing nucleons suggests that peripheral or single-particle exchange processes play a major role in producing the final state of reaction (1.3). The simplest processes are depicted in Figs. 16(a) and 20(a). If the exchanged particles are off-shell pions, we would expect the process shown in Fig. 16(a) to dominate strongly because of (a) I-spin considerations at the lower vertex, and (b) the comparative strengths of π^+p elastic and π^0p charge-exchange scattering.

We have verified that this is the case by examining the moments of the cosine distribution of polar angle θ in the t-channel system.[17] In Figs. 25(a)-25(h) we show the A_ℓ/A_0 moments for $\ell \leq 8$ as a function of $p\pi^+$ effective mass for peripheral $p\pi^+$ systems, e.g., $|\cos\theta_n| > 0.965$.[19] The

moments are defined as

$$\frac{A_\ell}{A_0} = (2\ell + 1) \langle P_\ell(\cos\theta) \rangle \tag{5.8}$$

with the uncertainty given by

$$\delta \left(\frac{A_\ell}{A_0}\right) = \frac{(2\ell + 1)}{\sqrt{N}} \left[\langle P_\ell^2 \rangle - \langle P_\ell \rangle^2 \right]^{1/2} \tag{5.9}$$

where P_ℓ represents the ℓth Legendre polynomial,[20] and N is the number of events in the $p\pi^+$ mass bin. The solid curves drawn in Fig. 25 represent the known (on-mass-shell) π^+p elastic scattering moments which were constructed from the CERN phase shifts.[21] The agreement between the data and curves is rather good in Fig. 25. However, there are discrepancies in the A_1/A_0 moment near threshold,[22] A_2/A_0 moment below 1.4 GeV.[23]

Apart from these minor discrepancies the scattering at the upper vertex of the diagram inset in Fig. 16(a) appears to be similar to real π^+p elastic scattering.

The pole extrapolation procedure which we now present is an outgrowth of our earlier analysis,[2] which only studied reaction (5.4). We now extend the analysis to $M(p\pi^+) = 2.02$ GeV. In addition, we now use only data with $t_n < 0.15$ GeV^2. For reaction (1.3) the pole or Chew-Low formula[24] (for the process inset in Fig. 16(a) with π^+ exchange) is given by

$$\lim_{t \to -\mu^2} \frac{d^2\sigma}{dtdM} = \frac{2}{4\pi m_p^2 P_{Lab}^2} \frac{g^2}{4\pi} \frac{t}{(t+\mu^2)^2} \left[M^2 Q\sigma(M)\right] \tag{5.10}$$

after integration over the decay angles in the $p\pi^+$ rest system. M, m_p, and μ are the $p\pi^+$, proton and pion masses, respectively; P_{Lab} is the laboratory

beam momentum, $g^2/4\pi = 29.2$, Q is the momentum in the $p\pi^+$ rest system, $t(=t_n)$ is the four-momentum transfer squared to the neutron, and $\sigma(M)$ is the on-shell π^+p elastic scattering cross section.

Following Ma et al.,[2] the conventional method of pole extrapolation to obtain the elastic cross section $\sigma(x\pi^+ \to x\pi^+)$ from a reaction of the type $xp \to x\pi^+n$ is to fit the ratio

$$\text{"t}\sigma\text{"} = \frac{t(d\sigma/dt)_{exp.}}{(d\sigma/dt)_{pole\text{-}eq.}} \tag{5.11}$$

to a polynomial in t. [When this ratio is properly extrapolated to the pion pole, it is equal to $-\mu^2 \times$ (on-shell $x\pi^+$ cross section).] Here $(d\sigma/dt)_{exp.}$ is the experimental differential cross section integrated over a mass bin of width ΔM. $(d\sigma/dt)_{pole\text{-}eq.}$ is the right-hand side of Eq. (5.10) evaluated assuming $\sigma(M) = 1$ mb and integrated over ΔM. A polynomial form $a+bt+ct^2+\ldots+$ is then fitted to the experimental "tσ" points, statistics usually preventing the use of higher powers than quadratic. Because of the low statistics and relatively low beam momenta used thus far for extrapolation analyses, the data are not sensitive to the presence of a small non-zero constant term a. Thus a is usually constrained to be zero.[25]

We have followed this procedure[26] and fit our "tσ" points to the polynomial $bt + ct^2$ to obtain $\sigma(\pi^+p \to \pi^+p)$ in seventeen $M(p\pi^+)$ bins spanning the range 1.12 - 2.02 GeV. The fit results are listed in two tables:
(a) Column 4 of Table X for the $\Delta^{++}(1238)$ region ($1.12 < M(p\pi^+) < 1.42$ GeV).
(b) Column 5 of Table XI for the high $M(p\pi^+)$ region ($1.42 < M(p\pi^+) < 2.02$ GeV).
The fits to the "tσ" points are acceptable in both $M(p\pi^+)$ regions (confidence

levels of 15% and 57%, respectively). The extrapolated π^+p cross sections are shown plotted in Fig. 26(a) as a function of $M(p\pi^+)$; the solid curve represents the known[27] π^+p elastic scattering cross section behavior. In the $\Delta^{++}(1238)$ region the extrapolated π^+p cross sections are in poor agreement [considering the size of the error bars in Fig. 26(a)] with the on-shell values shown (the χ^2 for this equality is 20.6 for nine degrees of freedom -- CL $\sim$ 1.5%). The difficulty is that the low-mass extrapolated cross sections are too large; this results in a too narrow width for the $\Delta^{++}(1238)$ (FWHM $\sim$ 0.085 GeV). In the high $M(p\pi^+)$ region the extrapolated π^+p cross sections appear to be in satisfactory agreement with the known on-shell values (the χ^2 for this equality is 11.1 for eight degrees of freedom -- CL $\sim$ 20%).

The shortcoming in the conventional pole extrapolation described above (worst in the $\Delta^{++}(1238)$ region) is that considerably more data are needed to determine the higher order coefficients and/or constant term which are evidently required for a perfect extrapolation. This necessity for a more complex extrapolating function arises because the normalizing function used in the denominator of Eq. (5.11) has a t dependence quite different from that of the numerator [of Eq. (5.11)]. If one could choose a normalizing function which has very nearly the same t dependence as $(d\sigma/dt)_{exp.}$ (and which reduces to the pole formula as $t \to -\mu^2$), then a less complex function of t would be required to fit the "$t\sigma$" points. Thus, if the normalizing function has exactly the t dependence of $(d\sigma/dt)_{exp.}$, then "$t\sigma$" will be linear in t and have a slope equal to the on-shell cross section. In view of this point, it seems evident that use of the pole formula as a normalizing function [in Eq. (5.11)] unnecessarily increases the complexity of the required extrapolation function.

Recent successes[22,28-30] in fitting the Chew-Low distributions of a large class of reactions using the Dürr-Pilkuhn[31] modified pole equation (DP-OPE) prompt us to suggest that DP-OPE would be a far superior choice of normalizing function than the pole equation itself. In fact we show in the next subsection the good agreement between the predictions of DP-OPE and the peripheral data for reaction (1.3) at 6.6 GeV/c. The modifications to the pole equation (5.10) are represented by the following vertex correction factors for $pp \to \Delta^{++}(1238)n$:

$$t \to t\left(\frac{1+R_n^2 q^2}{1+R_n^2 q_t^2}\right) \tag{5.12}$$

$$Q\sigma(M) \to Q\left(\frac{(M+m_p)^2+t}{(M+m_p)^2-\mu^2}\right)\left(\frac{Q_t}{Q}\right)^2\left(\frac{1+R_\Delta^2 Q^2}{1+R_\Delta^2 Q_t^2}\right)\sigma(M) \tag{5.13}$$

The latter expression (5.13) assumes a dominant p3/2 cross section only. Q_t (Q) are the incoming (outgoing) proton momenta in the Δ^{++} rest system. Similarly q_t^2 is the momentum squared of the incident proton as seen in the neutron rest frame and q^2 is this quantity taken on-shell. In addition to these DP vertex factors, which are both mass and t dependent, we also use the "universal" weakly t-dependent form factor[32] $G(t)^2 = [(2.3 - \mu^2)/(2.3 + t)]^2$ which Wolf[28] found was necessary in order to obtain good fits to the experimental distributions.

We have calculated the "tσ" points using DP-OPE as a normalizing function, i.e.,

$$\text{"t}\sigma\text{"} = \frac{t(d\sigma/dt)_{exp.}}{(d\sigma/dt)_{DP\text{-}OPE}} \tag{5.14}$$

and display them in Figs. 27(a)-27(q) as a function of t in the seventeen indicated $M(p\pi^+)$ bins. In calculating the normalizing denominator we assumed Wolf's values for $R_n(2.66\ GeV^{-1})$ and $R_\Delta(4.0\ GeV^{-1})$. The cross section $\sigma(M)$ on the R.H.S. of Eq. (5.13) was set to 1 mb. Least-squares fits of the data in Fig. 27 to the assumed forms bt and $bt+ct^2$ have been performed. The results of the fits are listed[33] in Tables X and XI; the solid curves drawn in Figs. 27(a)-27(i) represent the linear expansion "$t\sigma$" = bt using for b the best fit values listed in col. 3 of Table X. The curves appearing in Figs. 27(j)-27(q) represent the linear (bt) and quadratic ($bt+ct^2$) expansions for "$t\sigma$" using the best fit values for the parameters b and c. The points plotted at $t = -\mu^2$ in each of the component parts of Fig. 27 represent the extrapolated value of the function whose curve passes through the central value.

The linear forms describe the "$t\sigma$" points well in both $M(p\pi^+)$ regions (CL values of 10% and 45%, respectively) as the quadratic forms do also (CL values of 15% and 50%, respectively). The extrapolated π^+p cross sections are shown plotted in Fig. 26(b) as a function of $M(p\pi^+)$; the solid curve represents the known[27] π^+p elastic scattering cross section behavior. The solid dots represent the "$t\sigma$" = bt fit results and the open circle points represent the results of the quadratic fits. In the $\Delta^{++}(1238)$ region the extrapolated π^+p cross sections from the bt fits are in satisfactory agreement with the on-shell values shown (the χ^2 for this equality is 8.1 for nine degrees of freedom -- CL $\sim$ 52%). In addition, the resulting width or FWHM of 0.100 GeV is in satisfactory agreement with the width (FWHM $\sim$ 0.100 GeV) of the averaged on-shell π^+p cross section. In the high $M(p\pi^+)$ region the

extrapolated π^+p cross sections from the linear and quadratic fits yield CL values of less than 1% and nearly 80%, respectively, that they are equal to the known on-shell cross sections.

The pole extrapolation analyses indicate that: (a) In the $\Delta^{++}(1238)$ region, the conventional method of using the pole equation as the normalizing function in the extrapolation yields unreliable cross-section results when the "tσ" = $bt+ct^2$ expansion is used. In contrast, DP-OPE provides a normalizing function which is so close to the real data that for the statistics presently available to us, no terms besides linear are necessary in the expansion in order to yield extrapolated π^+p cross sections which are in good agreement with the expected values. Conversely DP-OPE appears to give a close description of the mass and t dependence of peripheral data for reaction (5.4). This latter point will be explicitly demonstrated in the next sub-section. (b) In the high $M(p\pi^+)$ region, both conventional and DP-OPE normalizing functions lead to reasonable extrapolations when the "tσ" = $bt+ct^2$ expansion is used. Fitting the "tσ" points in Figs. 27(j)-27(q) with a linear (bt) expansion leads to slightly unreasonable extrapolated π^+p cross sections. Conversely, DP-OPE [with only the process depicted in Fig. 16(a)] cannot precisely describe the peripheral data for reaction (1.3) for $M(p\pi^+) > 1.42$ GeV.

G. Analysis of the Peripheral $pp \to p\pi^+n$ Data

In this subsection the data for reaction (1.3) are separated into three regions of $M(p\pi^+)$ which have different characteristics and contain nearly equal numbers of events. Differential distributions of $M(p\pi^+)$, $M(\pi^+n)$, t_n, and t_p are first presented for each set of data. The corresponding peripheral distributions are also presented; these distributions, as well as additional graphs of the outgoing-nucleon angles and momentum transfer to the outgoing π^+ are then compared to the predictions of several pion-exchange models.

In the first case we attempt to describe the peripheral data of reaction (1.3) by means of an incoherent superposition[34] of the amplitudes corresponding to the one-pion-exchange diagrams labeled A and B in Fig. 28. The off-mass-shell vertex functions are related to the on-shell values by the Dürr-Pilkuhn[31] (DP-OPE) factors which we have used above in Sec. VF. The predictions of the DP-OPE model are absolute in that no free parameters are needed; values of the radii parameters were taken from other analyses.[28,29] When applicable we also compare the peripheral distributions to the normalized predictions of the Double-Regge-Pole (DRP) Model of Bali et al.,[35] utilizing only Pomeronchuk and pion exchange;[36] the process is depicted as diagram C in Fig. 28. We utilize several forms for the DRP matrix element. In addition, two free parameters are used in The DRP calculations: α', the slope of the pion trajectory, and s_0, the scale constant. The two parameters are varied in order to obtain best visual fits to the shapes of the experimental distributions. We find that values of $\alpha' = 1.0\ \text{GeV}^{-2}$ and $s_0 = 0.75\ \text{GeV}^2$ yield the best results. Both the detailed DP-OPE and DRP

calculations were carried out by means of a Monte-Carlo program;[37] the equations are outlined in the Appendix.

In Table XII we summarize the results of this subsection. For each $M(p\pi^+)$ range quoted in column 1 we list: (a) the number of events and the corresponding experimental cross section; (b) the t_n and t_p ranges allowed in the peripheral sample of data, as well as the numbers of events and the corresponding experimental cross section; (c) the peripheral cross-section predictions of the DP-OPE and DRP models; A and B refer to the contributions from processes A and B (in Fig. 28), respectively. Cases C and D refer to two choices for the DRP matrix element and are discussed below and in the Appendix.

The experimental differential distributions $d\sigma/dM(p\pi^+)$, $d\sigma/dM(\pi^+n)$, $d\sigma/dt_n$, and $d\sigma/dt_p$ are presented in parts (a)-(d), respectively, of Figs. 29-31 for the three respective $M(p\pi^+)$ ranges listed in Table XII. The t_n and t_p distributions in Figs. 29-31 peak at low values, thus displaying the generally peripheral nature of the data. The cross-hatched areas in Figs. 29-31 represent the events passing the peripheral selections listed in Table XII. The particular peripheral selections were chosen so as to separate the events in the peripheral forward peaks of the t distributions from the remaining data and to allow comparison with the predictions of the DP-OPE and DRP models in their domain of validity. The curves in Figs. 29-31 represent the predictions of the DP-OPE (solid curves) and DRP (dashed curves) models; the DRP curves are normalized to enclose an area equal to the peripheral experimental cross sections (which are listed in column 7 of Table XII). Fits of the DRP model to the peripheral data in Fig. 29 were not performed due to the dominance of the quasi-two-body reaction (5.4), and low $M(p\pi^+)$ values involved.[36]

Figure 29(a) indicates that reaction (5.4) dominates low $M(p\pi^+)$ data; however, several enhancements are present in Fig. 29(b) in the 1.2 - 1.3 and 1.4 - 1.6 GeV regions, possibly representing small amounts of $\Delta^+(1238)$ and $N^{*+}(1512)$ resonance production. The peripheral data of Fig. 29 appear to be well described in both shape and normalization by the DP-OPE predictions; the experimental cross section of 1.67 ± 0.11 mb compares extremely well with the predicted value (sum of processes A and B) of 1.65 mb. The only discrepancy appears to be an excess of events in the above mentioned $\Delta^+(1238)$ [$\sim$3.4 standard deviations (s.d)] and $N^{*+}(1512)$ ($\sim$2.6 s.d.) regions.

For the intermediate $M(p\pi^+)$ region the unshaded (uncut) $M(p\pi^+)$ spectrum [in Fig. 30(a)] appears relatively featureless. The $d\sigma/dM(\pi^+n)$ spectrum in Fig. 30(b) displays enhancements at the positions of the well known $\Delta^+(1238)$, $N^{*+}(1512)$, and $N^{*+}(1688)$[38] positions. In addition, a large peak appears at high mass near 2.8 GeV; this peak appears to be associated with the slightly enhanced region in Fig. 30(a) from 1.7 - 2.0 GeV, and with higher momentum transfers. The distributions of momentum transfer, $d\sigma/dt_n$ and $d\sigma/dt_p$ in Figs. 30(c) and 30(d), respectively, are dominated by peripheral forward peaks, which grade into more gently sloping distributions beginning at 0.6 GeV^2; furthermore, the $d\sigma/dt_p$ distribution is nearly flat for $0.7 < t_p < 1.8$ GeV^2.

The cross-hatched data in Fig. 30 continue to display the low-mass bumps in the $M(\pi^+n)$ spectrum; the high-mass effects are removed by the t cuts. The peripheral data again appear to be well described in both shape and normalization by the DP-OPE predictions; the experimental cross section

of 1.03 ± 0.07 mb compares well with the predicted value of 1.0 mb. Several discrepancies existing between the shaded data and solid curves are excesses of data below 1.5 GeV in the $M(p\pi^+)$ projection (∿5 s.d.), and at the $N^{*+}(1512)$ (∿1.5 s.d.) and $N^{*+}(1688)$ (∿2.6 s.d.) positions in the $M(\pi^+n)$ projection. The dashed curves appearing in Fig. 30 represent the normalized predictions of the DRP model, using for the quantity X in Eq.(A9) the expression

$$X = t_n \left[\frac{\Gamma(1)\ \Gamma(3/2+\alpha)}{\Gamma(3/2)\ \Gamma(1+\alpha)}\right]^2 \qquad \text{(A10)}$$

where Γ represents Euler's gamma function. The use of this particular value for X, which we refer to as Case D, yields an integrated theoretical cross section of 1.65 mb. The DRP model apparently forms a slightly poorer approximation to the shapes of the peripheral distributions in Fig. 30 than does the DP-OPE model. In particular, the discrepancy in the $M(p\pi^+)$ projection is more pronounced, and the $N^{*+}(1512)$ and $N^{*+}(1688)$ bumps exceed the dashed curves by slightly more than they do the solid curves.

Figure 31(b) displays two well-defined enhancements in the region of 1.46 and 1.65 GeV; the latter appears to be wider than the $N^{*+}(1688)$ bumps observed in Fig. 30(b). The peripheral cuts severely reduce the $M(\pi^+n)$ projection for $M(\pi^+n) > 1.5$ GeV. The experimental cross section of 0.69 ± 0.05 mb can be compared to the DP-OPE prediction of 0.57 mb and to the DRP prediction of 0.18 mb using μ^2 for the quantity X in Eq.(A9), where μ is the charged-pion rest mass. Figures 31(a), 31(c), and 31(d) indicate agreement in shape between both the DP-OPE and DRP model predictions and the peripheral data; the solid curves are slightly low in each case. Figure 31(b)

exhibits the apparent cause of the low DP-OPE predicted normalization: the solid curve agrees well with the data everywhere except in the region from 1.3 to 1.5 GeV, where the data exceed the curve by approximately 8 s.d. The shape of the dashed (normalized) curve in Fig. 31(b) is similar to that of the data, however.

Further comparisons between the peripheral data and the predictions of the DP-OPE and DRP models are exhibited in Figs. 32-34. The distributions in parts (a)-(f) are of $\cos\theta_p$, $\cos\theta_n$, ϕ_p, ϕ_n, $t_{p_p\pi^+}$ and $t_{p_n\pi^+}$, respectively, where $\theta_p(\theta_n)$ is the angle between the appropriate incoming proton and the outgoing proton(neutron) evaluated in the $\pi^+p(\pi^+n)$ rest system. The ϕ angles represent the corresponding azimuthal angles in the standard t-channel (Gottfried-Jackson) coordinate system.[39] The momentum transfers from the two incoming protons to the π^+ are represented by $t_{p_p\pi^+}$ and $t_{p_n\pi^+}$, respectively. In general, the data and curves agree fairly well. The important discrepancies are the slightly low normalization of the solid curves in Fig. 34, the slightly incorrect shapes of the dashed curves in Figs. 33(e) and 33(f), and the shape of the solid curve in Fig. 32(a).

The comparison of the DP-OPE (assuming processes A and B in Fig. 28) model with the peripheral data of reaction (1.3)(described above), indicates general agreement in shape. The absolute normalization of the DP-OPE predictions agree quite well with the experimental values except in the $M(p\pi^+) > 2.0$ GeV data with $1.3 < M(\pi^+n) < 1.5$ GeV, thus suggesting the presence of a significant non-OPE process there.[40] These results are noteworthy in that no parameters were varied in order to obtain agreement; values of the radii parameters (for DP-OPE) were taken from analyses

of other reactions.[28,29] In addition, the off-mass-shell angular distributions at the four-body vertices of processes A and B in Fig. 28, which are required in the calculations, were simply approximated by the on-shell values.[21] This approximation works well everywhere except as shown in Fig. 32(a).

The DRP formulas (assuming process C in Fig. 28) always yield cross sections significantly different from the experimental values so the predictions are normalized to the experimental cross sections. Therefore, the DRP results are ambiguous; but they are encouraging in that they generally reproduce the shapes of the peripheral data. Presumably subjects like the explicit t dependence of the residue function[41] and the Toller angle[42] dependence (assumed nil in this work) should be also considered, in connection with the absolute normalization.

The analyses of the peripheral data for reaction (1.3) indicate that pion-exchange phenomenology (including absorption) can account for the gross features in all $M(p\pi^+)$ regions. There appears to be some evidence for production of N^{*+} resonances in $pp \to pN^{*+}$ by other exchange(s), however.

VI. COLLECTIVE STUDIES OF REACTIONS (1.2) AND (1.3)

A. I-spin 1/2 Nucleon Resonance Production

In this subsection we discuss the reaction (1.3) data with $M(p\pi^+)$ > 2.4 GeV. We recall that in Sec. VG the peripheral data in Fig. 31(b) exceeded the OPE-model predictions for $1.3 < M(\pi^+n) < 1.5$ GeV. Furthermore, a significant signal was also observed near 1.65 GeV in the unshaded $M(\pi^+n)$ distribution. We examine these two signals in some detail here. The reaction (1.2) data are also considered in the same light for the purpose of establishing the identity and isospin(I) of the above mentioned two enhancements. In Sec. VIB we explicitly demonstrate the I = 1/2 nature of the enhancements by means of a somewhat different approach.

The $p\pi^0$ and π^+n mass distributions are displayed in Figs. 35(a) and 35(b), respectively, for the 2591 examples of reaction (1.2), and for a partial sample of 5324 reaction (1.3) events. Both distributions peak at low-mass values and exhibit structure atop a large background. The large background is due to, e.g., process A in Fig. 28 [for reaction (1.3)]. This background is decreased by requiring $M(p\pi^+) > 2.4$ GeV; this restricts t_n to values greater than 0.26 GeV^2, thus minimizing the OPE contribution corresponding to process A. In Fig. 36(a) we display the $M(\pi^+n)$ spectrum for $M(p\pi^+) > 2.4$ GeV; significant structure is again observed near 1.45 and 1.65 GeV. Similarly, we show in Fig. 36(b) the $M(p_i\pi^0)$ histogram for events with $M(p_j\pi^0) > 2.4$ GeV ($i \neq j$). The sum of both component figures is displayed in Fig. 36(c). The combined signal in the 1.425 - 1.5 GeV mass region is $\sim$6 s.d. above the background level.

To determine the parameters of the two enhancements in Fig. 36(c), we utilize the least-squares method and fit the data to an incoherent sum of a quadratic background and two s-wave Breit-Wigner functions. The explicit Breit-Wigner form used is

$$f_{BW} \equiv \frac{1}{[(M-M_i)/.5\Gamma_i]^2 + 1} \tag{6.1}$$

where M is the mass of the πN system, M_i is the central mass value of the i^{th} resonance, and Γ_i is the corresponding full width at half maximum (FWHM). The best-fit masses and widths thus obtained are $M_1 = 1.462 \pm 0.006$ GeV, $\Gamma_1 = 0.054 \pm 0.012$ GeV, $M_2 = 1.65 \pm 0.01$ GeV, and $\Gamma_2 = 0.094 \pm 0.020$ GeV. The width parameters are sensitive to the background level; thus the quoted errors include an additional uncertainty due to our choice of background. The experimental resolution in this mass region is 0.023 GeV FWHM, thus indicating that the natural widths for M_1 and M_2 are $0.049 \pm .012$ and $0.091 \pm .020$ GeV, respectively.

The fitted values of M_1, M_2, Γ_1, and Γ_2 have been used to determine the amount of the resonances present in reactions (1.2) and (1.3) separately. Since identical mass cuts have been made for both reactions, we may reasonably expect that the relative rates of a given resonance in Figs. 36(a) and 36(b) are the same as those without cuts. One notes that the mass cut discussed previously excludes any possibility of double counting for reaction (1.2) in the region of the peaks since events with both $M(p\pi^0)$ combinations below 2.4 GeV are not included in the fits. The resultant branching ratios are given in Table XIII. Since identical sets of exchange

diagrams are accessible for reactions (1.2) and (1.3), the relative rate of production for a given resonance depends only on the isotopic spin of the resonance in question. We conclude that the enhancements at 1.462 and 1.650 GeV are I = 1/2 states. It is interesting to point out that while the resonance parameters for the 1.650 GeV enhancement agree well with other published bubble chamber data in three body modes,[43] our result on the 1.462 GeV resonance is considerably narrower than other published results in this mass region.

The decay angular distribution of the $N^+(1462)$ is distorted due to the mass cut quoted above. Thus we have not been able to measure its spin and parity. However, if a $J^P = 1/2^+$ assignment is assumed for this enhancement, we can estimate the cross-sections for the processes

$$\begin{array}{l} pp \rightarrow pN^+(1462) \\ \qquad\quad \big\lfloor\!\rightarrow n\pi^+ \end{array} , \qquad (6.2)$$

and

$$\begin{array}{l} pN^+(1462) \\ \big\lfloor\!\rightarrow p\pi^0 . \end{array} \qquad (6.3)$$

The loss of events due to the mass cut has been estimated using the Monte-Carlo method and an isotropic decay angular distribution. The cross-sections for reactions (6.1) and (6.2) are estimated to be 0.29 ±.06 and 0.15 ± .03 mb, respectively, or a total cross-section of 0.44 ± .07 mb for the process $pp \rightarrow pN^+(1462)$, $N^+(1462 \rightarrow N\pi$(all charges).

Next, we have examined the four momentum transfer distributions to the $N^+(1462)$, which is defined by a band from 1.402 to 1.510 GeV. In Fig. 37(a) all events are used; samples from reactions (1.2) and (1.3) have been added

after careful examination to ascertain that no statistically significant difference exists in their t distributions. Figure 37(b) shows the t distribution of a subsample of data for which the mass of the pion with the unrelated nucleon is greater than 2.4 GeV. In both cases, the data are fitted to the form $e^{bt + ct^2}$ for $0.05 \leq t \leq 0.5$ GeV^2. The lower limit is chosen to avoid a turnover of the t distribution due to the kinematical boundary. The resultant parameters are given in Table XIV. As may be seen, the slope parameter b is inconsistent with a value of $\sim$20 GeV^{-2} as reported in counter and spark chamber measurements.[44] Since we believe that the $N^+(1462)$ has an identical set of quantum numbers as the proton, we may also expect similarities between reactions (6.2), (6.3) and (1.1). Our slope parameter b agrees well with the value of 7.94 ± 0.26 GeV^{-2} for reaction (1.1) at 6.6 GeV/c.

B. Separation of I-spin 1/2 and 3/2 πN Systems

In order to perform an isotopic-spin separation in $pp \to N\pi N$ reactions the outgoing pi meson must be associated with one of the outgoing nucleons. Following earlier analyses[45,46] we assign the π to a nucleon which is referred to as N_1, such that $N_1\pi$ has the minimum invariant mass (MIM), i.e., $M(N_1\pi) < M(N_2\pi)$. The MIM separation method suffers from a slight ambuigity problem when both invariant masses are small. We neglect this effect. The use of this criterion for separation yields [for $\sigma(pp \to N_1\pi N_2)$]

$$\begin{aligned} \sigma_1 &\equiv \sigma(pp \to p\pi^+n) = 2.94 \pm 0.19 \text{ mb} \\ \sigma_2 &\equiv \sigma(pp \to n\pi^+p) = 2.79 \pm 0.18 \text{ mb} \\ \sigma_3 &\equiv \sigma(pp \to p\pi^0p) = 2.54 \pm 0.16 \text{ mb} \end{aligned} \qquad (6.4)$$

In order to separate the different isopopic spin contributions to reactions (6.4) we define $|A_{2I}|^2$ to be the integrated cross section for producing the $N_1\pi$ system with isotopic-spin I. Then from charge independence and Bøggild et al.,[46] we have

$$
\begin{aligned}
|A_3|^2 &\equiv (4/3)\sigma_1 = 3.92 \pm 0.25 \text{ mb} \\
|A_1|^2 &\equiv \sigma_3 + \sigma_2 - (1/3)\sigma_1 = 4.35 \pm 0.38 \text{ mb} \qquad (6.5) \\
\mathrm{Re}(A_1^* A_3) &\equiv (1/\sqrt{2})[2\sigma_3 - \sigma_2 - (1/3)\sigma_1] = 0.92 \pm 0.23 \text{ mb} .
\end{aligned}
$$

We have shown earlier[4] that the ratio of $|A_1|$ to $|A_3|$ increases with increasing beam momentum. The $d\sigma/dM(N_1\pi)$ projections of $|A_3|^2$, $|A_1|^2$, and $\mathrm{Re}(A_1 A_3^*)$ are plotted in Figs. 38(a), 38(b), and 38(c), respectively. Of course, the I = 3/2 mass distribution is dominated by the $\Delta^{++}(1238)$ with little significant structure at higher mass values. The I = 1/2 mass distribution displays the peaks near 1.45 and 1.65 GeV, which we analyzed above in Sec. VIA. The interference term shows structure in the $\Delta(1238)$ region.

Turning now to the question of the dominant exchange responsible for the $|A_3|^2$ and $|A_1|^2$ cross sections, we have shown (in Sec. VF) that OPE is dominant in reaction (5.4) and that significant OPE contributions exist also at higher $M(p\pi^+)$ values. Thus we conclude that the $|A_3|^2$ cross section is dominantly due to OPE, in agreement with Bøggild et al.[47] In the case of the $|A_1|^2$, it was shown earlier,[46] by means of energy independence arguments, that Pomeron exchange appears to be dominant at 19 GeV/c. If the I=1/2 cross section is due mainly to Pomeron exchange at both 6.6 and 19 GeV/c, then the ratio of these cross sections should closely approximate the square of the ratio of the pp total cross sections,[48] which is roughly $(41/39)^2 = 1.11$. The ratio $|A_1|^2_{6.6} / |A_1|^2_{19} = 4.35/2.3 = 1.89 \pm 0.30$

was obtained using our result and that of Bøggild et al.[46] The two ratios differ by roughly 2.5 standard deviations, suggesting energy non-independence of $|A_1|^2$ in going from 6.6 to 19 GeV/c. Therefore Pomeron exchange appears not to be dominant in producing I = 1/2 Nπ systems at 6.6 GeV/c. In fact, Rushbrooke[49] has shown, using pp and pd data at 6.92 GeV/c, that the Pomeron-exchange contribution amounts to (36^{+7}_{-11})% of the total reaction amplitude.[50] A similar calculation using our pp data (at 6.6 GeV/c) together with the 6.92 GeV/c pd data[49] indicates a 33% contribution.

VII. CONCLUSION

Our study of $pp \to pp$ yields 11.47 ± 0.33 mb for the elastic cross section at 6.6 GeV/c. In addition, the scattering is dominantly peripheral with a slope of 7.94 ± 0.26 GeV^{-2} for the t distribution over the range $0.05 < |t| < 0.50$ GeV^2. This slope corresponds to an optical model radius of $(1.12 \pm 0.02) \times 10^{-13}$ cm. Using the optical theorem with the known value for the total proton-proton cross section, we find a value of 0.26 ± 0.13 for the absolute ratio of the real to the imaginary part of the forward scattering amplitude $|\alpha|$, in agreement with other workers.[11]

The production cross sections for the single-pion production reactions $pp \to pp\pi^0$ and $pp \to p\pi^+n$ are found to be 2.54 ± 0.16 mb and 5.73 ± 0.35 mb, respectively. Cross sections for the latter process are found to be consistent with a $|P_{Lab}|^{-1.06}$ dependence over the range 2.8 - 28.5 GeV/c. The nucleon c.m. angular distributions are steeply peaked and require Legendre terms to $L \sim 15$ for an adequate description; the pion distributions require fewer terms. The single-particle nucleon t distributions for reaction (1.3) indicate changes in slope in t_p at 0.7 and 1.8 GeV^2, and in t_n at 0.5 GeV^2. Fits to the form Ae^{-yt} in the $0.05 < t < 0.50$ GeV^2 region yield values of $y = 4.4$ GeV^{-2} for both the t_p and t_n distributions; these values are less steep than the slope found in reaction (1.1) (7.9 GeV^{-2}) for the same t interval.

Resonance production is present in the $N\pi$ systems of the $pp \to N\pi N$ data. In particular, the process $pp \to \Delta^{++}(1238)n$ accounts for 35% of the reaction (1.3) data. The differential cross section $d\sigma/dt_n$ is described well by the sum of two exponentials with fitted slopes 10.5 ± 0.3 GeV^{-2} and 1.9 ± 0.1 GeV^{-2}

over the region $0.02 < |t_n| < 4.0$ GeV^2. Both the t_n and the $\Delta^{++}(1238)$ decay distributions are consistent with a one-pion-exchange production process, modified by absorptive effects.

In fact, pion-exchange phenomenology can account for the gross features of the peripheral $pp \to p\pi^+n$ data for $M(p\pi^+) < 2.4$ GeV. We have demonstrated this in several ways: (a) the angular distributions of scattering, at the upper vertex of the process inset in Fig. 16(a), are similar to real π^+p elastic scattering angular distributions; (b) modified pole-extrapolation techniques yield the correct π^+p elastic scattering cross sections over the $1.08 < M(p\pi^+) < 2.02$ GeV range; (c) fairly good agreement, in both shape and normalization, is obtained in comparisons of the experimental distributions to the predictions of several theoretical models utilizing pion-exchange contributions, both Reggeized and elementary. Furthermore, these models allow for the production of Δ^+ and N^{*+} resonances by π^0 exchange in, e.g., the process depicted inset in Fig. 20(a).

Isospin 1/2 isobars are produced in $pp \to pN^{*+}$ reactions by some non-OPE process in both the reaction (1.2) and (1.3) events, especially when the effective mass of the pion with the unrelated proton is large (e.g., $M(p\pi) > 2.4$ GeV). Best fit masses of 1.462 ± 0.006 GeV and 1.65 ± 0.01 GeV and corresponding widths of 0.049 ± 0.012 GeV and 0.091 ± 0.020 GeV are obtained for the isobars. A cross section of 0.44 ± 0.07 mb is found for $pp \to pN^+(1462)$ assuming an isotropic decay distribution; furthermore the t dependence is similar to that of reaction (1.1), suggesting the proton quantum numbers for the $N^+(1462)$.

ACKNOWLEDGMENT

We wish to thank H. K. Ticho and S. Wojcicki for their participation in the early stages of this experiment and W. Chinowsky, who designed and built the P65 beam. We also thank Emilio Segrè for his continuing support. This experiment would not have been possible without the efforts of Robert Watt and the entire crew of the 72-in. bubble chamber. We also thank Suzie Sayre for typing this work. Finally, the work of the scanners, programmers, draftsmen, and photographers of both the Lawrence Berkeley Laboratory and Michigan State University is gratefully acknowledged.

APPENDIX

PION-EXCHANGE PREDICTIONS FOR THE PERIPHERAL DATA OF REACTION (1.3)

In this section the explicit predictions of the Dürr-Pilkuhn[31] modified one-pion exchange (DP-OPE) and Double-Regge-Pole[35] (DRP) models are written out for the peripheral data of reaction (1.3).

The cross section σ for any scattering process which yields the final state of reaction (1.3) can be expressed as[51]

$$\sigma = \frac{1}{(2\pi)^5 4m_p P_{Lab}} \int \sum |G|^2 \, dR_3(\sqrt{s}, m_p, m_{\pi^+}, m_n) \tag{A1}$$

where m_i is the rest mass of the i^{th} particle, P_{Lab} is the laboratory beam momentum, G is the invariant amplitude for the process, and R_3 represents Lorentz-invariant three-body phase space.[52]

A. DP-OPE Model with Processes A and B in Fig. 28

In this case

$$|G|^2 \approx 2(|G_A|^2 + |G_B|^2) \tag{A2}$$

if we assume[34] that the non-vanishing interference terms between diagrams corresponding to interchanges of incoming protons and/or outgoing nucleons between vertices are small. The form of $|G_A|^2$, for example, can be expressed as

$$\lim_{t \to -\mu^2} \sum |G_A|^2 = 64\pi^2 M^2 g^2 \frac{t}{(t+\mu^2)^2} \frac{Q_t}{Q} \frac{d\sigma}{d\Omega}(M,t) \tag{A3}$$

where M is the $p\pi^+$ effective mass, t is the momentum transfer squared to the outgoing neutron [defined as in Eq. (5.2)], $Q_t(Q)$ is the incoming (outgoing) momentum evaluated in the $p\pi^+$ rest system, $g^2 = 4\pi \times 29.2$, and $d\sigma(M,t)/d\Omega$ is the differential cross section for the scattering of the exchanged particle (of mass -t) off the incoming proton to yield the $p\pi^+$ system of mass M. Following DP,[31] Wolf,[28] and Colton et al.,[29] we modify (A3) for use in the physical region of t:

$$t \to t \left(\frac{c-\mu^2}{c+t}\right)^2 \left(\frac{1+R_n^2 q^2}{1+R_n^2 q_t^2}\right) \tag{A4a}$$

$$Q_t \frac{d\sigma(M,t)}{d\Omega} \to Q \frac{d\sigma(M,-\mu^2)}{d\Omega} \left[\frac{1}{\sigma(M)} \sum_{LJ} \sigma_{LJ} f_{LJ}\right] \tag{A4b}$$

for M < 1.6 GeV, and

$$Q_t \frac{d\sigma(M,t)}{d\Omega} \to Q \frac{d\sigma(M,-\mu^2)}{d\Omega} \tag{A4c}$$

for M > 1.6 GeV.[53]

In Eq. (A4a) q_t^2 is the square of the momentum of the incoming proton evaluated in the neutron rest system; q^2 is this quantity taken on-shell. Wolf's[28] values for c and R_n are used. In Eqs. (A4b) and (A4c) $d\sigma(M,-\mu^2)/d\Omega$ represents the on-mass-shell π^+p elastic differential cross section, $\sigma(M)$ is the total elastic cross section and $\sigma_{LJ}(M)$ is the corresponding cross section for scattering in the orbital and total angular momentum states L and J, respectively. These cross sections were calculated from the CERN phase shifts.[21] The f_{LJ} represent the DP modifications

using known[29] values for the free "radii" parameters. The summation in Eq. (A4b) is carried out to d3/2 partial waves.[54] Expressions similar to Eqs. (A3) and (A4) can also be written for $|G_B|^2$.

Integration of Eq. (A1) utilizing the assumptions of Eqs. (A2) - (A4), inclusive, yield the solid curves drawn in Figs. 29-34 as well as the cross section values for processes A and B (in Fig. 28) which are listed in Table XII.

B. DRP Model with Process C in Fig. 28

Following Berger[36] we write

$$\sum |G|^2 = \frac{(\pi\alpha')\ NX}{(1-\cos\pi\alpha_\pi)}\left(\frac{s_{n\pi}\cdots}{s_0}\right)^{2\alpha_\pi} H(t_n,t_p,\omega)\left(\frac{s_{p\pi}\cdots}{s_{10}}\right)^{2\alpha_p} H_p(t_p) \qquad (A5)$$

where α_i represents the trajectory function for the i exchange particle. Following Berger[55] we re-express the Pomeronchuk exchange as

$$\left(\frac{s_{p\pi}\cdots}{s_{10}}\right)^{2\alpha_p} H_p(t_p) \to 64\pi^2 M^2 \frac{d\sigma}{d\Omega}(M,-\mu^2) \qquad (A6)$$

The slope of the pion trajectory α' is defined by

$$\alpha_\pi = -\alpha'(t_n+\mu^2), \qquad (A7)$$

the $(s_{n\pi}\cdots)$ term is given by

$$(s_{n\pi}\cdots) = M^2(\pi^+n) + t_p - m_p^2 - \frac{1}{2}(\mu^2 + t_p + t_n) \qquad (A8)$$

As usual we neglect the dependence upon Toller angle ω.[42] The factor N in Eq. (A5) is chosen so that the expression (A5) will reduce to the OPE expression as $t_n \to -\mu^2$; thus $N = g^2$ where $g^2 = 4\pi \times 29.2$. The

working version of Eq. (A5) can be expressed as

$$\sum |G|^2 = \frac{(\pi\alpha')^2 g^2 X}{(1-\cos\pi\alpha_\pi)} \left(\frac{s_{n\pi\cdots}}{s_0}\right)^{2\alpha_\pi} 64\pi^2 M^2 \frac{d\sigma}{d\Omega}(M,-\mu^2) \qquad \text{(A9)}$$

The free parameters in the DRP calculations are α' and s_0; comparisons between the shapes of the data and the predictions of (A1) using (A9) for $\sum|G|^2$ indicate best values for α' and s_0 of 1.0 GeV^{-2} and 0.75 GeV^2, respectively. We use these values throughout in calculating the DRP predictions discussed in the text.

The quantity X appearing in Eq. (A9) was set to μ^2 by Berger[36] in his analysis of reaction (1.3) at 28.5 GeV/c for $M(p\pi^+) > 2.0$ GeV. We find that this choice does not represent the data well for $1.42 < M(p\pi^+) < 2.0$ GeV. In Fig. 39 are displayed the $d\sigma/dt_n$ distributions for the peripheral data in the indicated $M(p\pi^+)$ ranges. Case C (the solid curves) represent the normalized predictions of Eq. (A1) using (A9) with $X=\mu^2$. Case D, which we define by

$$X = t_n \left[\frac{\Gamma(1)\Gamma(3/2 + \alpha_\pi)}{\Gamma(3/2)\Gamma(1 + \alpha_\pi)}\right]^2 \qquad \text{(A10)}$$

represent the corresponding normalized predictions (dashed curves in Fig. 39). The ratio of Gamma functions emerges in the asymptotic expansion of the Legendre polynomial of the scattering angle cosine in the t channel.[41] Case D represents an alternate choice for the reduced residue function which describes the coupling of the Reggeized pion to the np vertex in Process C of Fig. 28.

Clearly the dashed curve (Case D) represents a much better approximation to the data in Fig. 39(a), while the solid curve (Case C) is slightly better in Fig. 39(b). Therefore, in the discussion of the peripheral data

for reaction (1.3) (Sec. VG), we use the form of Eq. (A10) for X in the intermediate $M(p\pi^+)$ region and Berger's[36] form (μ^2) in the high $M(p\pi^+)$ region. The dashed curves appearing in Figs. 30-34 represent the normalized predictions of Eq. (A1) using Eq. (A9) for $\sum |G|^2$ and the values of 1.0 GeV^{-2} and 0.75 Gev^2 for α' and s_0, respectively.

REFERENCES AND FOOTNOTES

*Work supported in part by the National Science Foundation (MSU) and by the U. S. Atomic Energy Commission (LBL, UCLA).

1. For analyses of elastic scattering and single-pion production in proton-proton collisions at other momenta, see, e.g.,
W. J. Fickinger, et al., Phys. Rev. 125, 2082 (1962) [2.80 GeV/c];
G. A. Smith, et al., Phys. Rev. 123, 2160 (1961) [3.67 GeV/c];
S. Colletti, et al., Nuovo Cimento 49, 3559 (1967) [4 GeV/c];
G. Alexander, et al., Phys. Rev. 154, 1284 (1967) [5.5 GeV/c];
T. H. Tan, et al., Phys. Letters 28B, 195 (1968) [6.0 GeV/c];
G. Alexander, et al., Phys. Rev. 173, 1322 (1968) [6.92 GeV/c];
J. Ginestet, et al., Nucl. Phys. B13, 283 (1969) [8.1 GeV/c];
S. P. Almeida, et al., Phys. Rev. 174, 1638 (1968) [10 GeV/c];
H. Bøggild, et al., Phys. Letters 30B, 369 (1969) [19 GeV/c];
W. E. Ellis, et al.,

2. Z. Ming Ma et al., Phys. Rev. Letters 23, 342 (1969).
3. Z. Ming Ma and Eugene Colton, Phys. Rev. Letters 26, 333 (1971).
4. Eugene Colton and Z. Ming Ma, Lawrence Berkeley Lab. Report No. LBL 390 (to be published in Il Nuovo Cimento A),1972.
5. W. A. Wenzel, Lawrence Radiation Laboratory Report No. UCRL-10868, 1963 (unpublished).
6. W. Chinowsky, et al., Phys. Rev. 165, 1466 (1968).
7. M. A. Abolins et al., Phys. Rev. Letters 25, 126 (1970).
8. Eugene Colton, University of California, Los Angeles, Report No. UCLA-1025, 1968 (unpublished) Sec. (V.E).

9. D. Harting et al., Nuovo Cimento 38, 60 (1965).

10. Particle Data Group Report No. UCRL 20000 NN, 1970 (unpublished).

11. K. J. Foley et al., Phys. Rev. Letters 19, 857 (1967).

12. L. Van Hove, Nucl. Phys. B9, 331 (1969).

13. See, e.g., E. Colton and A. R. Kirschbaum, Lawrence Berkeley Laboratory Report No. LBL 730 (to be published in Phys. Rev. D), 1972.

14. Eighty-six percent (86%) of the data for reaction (1.3) have $1.14 < M(p\pi^+) < 1.42$ GeV and $t_n < 0.4$ GeV^2.

15. The t dependence of Fig. 23 for $t > 1$ GeV^2 may be due entirely to background and not to reaction (5.4). See Fig. 16.

16. K. Gottfried and J. D. Jackson, Il Nuovo Cimento 33,309 (1964).

17. In the conventional t-channel coordinate system, the incident proton as seen in the $\Delta^{++}(1238)$ rest frame is taken as the polar or z-axis; the y axis is along the normal to the production plane $\hat{y} = \hat{n} \sim \hat{P}_p \times \hat{P}_\Delta$.

18. See, e.g., J. D. Jackson, invited paper to the Conference on High-Energy Two-Body Reactions held at the State University of New York, Stony Brook, New York, 1966 (unpublished).

19. θ_n is defined as in Fig. 7(b).

20. See, e.g., J. D. Jackson, Classical Electrodynamics, (John Wiley and Sons, Inc., New York, 1962), p. 57.

21. A. Donnachie, R. G. Kirsopp and C. Lovelace, CERN Report No. Th-838, Addendum, 1967 (unpublished).

22. This effect can be partly explained by off-mass-shell effects. See, e.g., Eugene Colton and Peter E. Schlein, in Proceedings of the Conference on $\pi\pi$ and $K\pi$ Interactions (Argonne National Laboratory. Argonne, Ill., 1969), P.1.

23. This effect may be analogous to the observed depolarization of the ρ^0 produced in $\pi^- p \to \rho^0 n$. In this case nonzero helicity states of the ρ^0, forbidden by simple OPE, but allowed by the absorption model, occur.

24. G. F. Chew and F. E. Low, Phys. Rev. 113, 1640 (1959).

25. See, e.g., J. P. Baton et al., Nucl. Phys. B3, 349 (1967).

26. We use the expression

$$\text{"t}\sigma\text{"} = \frac{c}{\int dt dM} \sum_{i=1}^{n} \left[\frac{t}{(d^2\sigma/dtdM)_{\text{pole eq.}}} \right]_i$$

to evaluate "tσ" for a given ΔtΔM bin. Here c = 5.73/6424 mb/event, the sum is over the events in the (t,M) bin and the bracketed quantity is evaluated for each event. The integral ∫dtdM is over that portion of the ΔtΔM bin in question which is included in the physical region of the Chew-Low plot.

27. For $M(p\pi^+) < 1.30$ GeV the $\pi^+ p$ elastic cross sections were obtained from e.g., A. A. Carter et al., Nucl Phys. B26, 445 (1971). For $M(p\pi^+) > 1.3$ GeV the cross sections were obtained from the CERN phase shifts (Ref. 21).

28. G. Wolf, Phys. Rev. Letters 19, 925 (1967).

29. E. Colton et al., Phys. Rev. D3, 1063 (1971). See also e.g., T. G. Trippe et al., Phys. Letters 28B, 203 (1968).

30. See. e.g., The Review talk by P. E. Schlein in Meson Spectroscopy, eds. C. Baltay and A.H. Rosenfeld (W. A. Benjamin, Inc., New York, 1968), p. 161.

31. H. P. Dürr and H. Pilkuhn, Nuovo Cimento 40A, 899 (1965).

32. This parametrization of the form factor G(t) was introduced by G. Goldhaber et al., Phys. Letters 6, 62 (1963).

33. The results of the "tσ" = $bt + ct^2$ fits are not listed in Table X since they are essentially no better than the linear fit results.

34. At this beam energy, the interference terms between diagrams differing only by interchanges in beam and target protons or outgoing nucleons are small; interference terms between diagrams differing by interchanges of the outgoing π^+ between vertices are identically zero because of the $g\gamma_5$ or pseudoscalar coupling at the NNπ vertices. See, e.g., J. D. Bjorken and S. D. Drell, Relativisitic Quantum Mechanics, (McGraw-Hill, New York, 1964), section on Feynman rules.

35. N. F. Bali et al., Phys. Rev. Letters 19, 614 (1967), See also Phys. Rev. 163 1572 (1967).

36. E. L. Berger, Phys. Rev. Letters 21, 701 (1968).

37. J. H. Friedman, Group A Programming Note P-189 (ReV), 1971 (unpublished).

38. We refer to the $N^{*+}(1688)$ as the enhancement near 1.7 GeV in the $M(\pi^+ n)$ spectrum. Actually three T = 1/2 and two T = 3/2 resonances are known to exist (from phase-shift analyses) in the region of 1.7 GeV. For their masses, partial wave structure, and decay modes, see, e.g., Rev. Mod. Phys. 43, S1 (1971).

39. The t-channel coordinate system uses for its y and z axes the normal to the production plane and the direction of the appropriate incoming proton as seen in the outgoing Nπ rest system, respectively.

40. Similar behavior has also been observed in the Nπ systems of the reactions $K^- p \to (K^*)^- (N\pi)^+$ at 3 GeV/c. See, e.g., E. Colton et al., Nucl. Phys. B17, 117 (1970).

41. See, e.g., L. Van Hove, CERN Report No. CERN 68-31, 1968 (unpublished).

42. The Toller angle ω is defined in the π^+ rest system by $\cos\omega = (\vec{P}_1 \times \vec{P}_p)\cdot(\vec{P}_2 \times \vec{P}_n) \,/\, |\vec{P}_1 \times \vec{P}_p||\vec{P}_2 \times \vec{P}_n|$ where the incoming proton momentum with the subscript 1 or 2 is crossed with the momentum of the appropriate outgoing proton or neutron, respectively.

43. See, e.g., R. Ehrlich et al., Phys. Rev. Letters 21, 1839 (1968).

44. G. Bellettini et al., Phys. Lett. 18, 167 (1965); E. W. Anderson et al., Phys. Rev. Lett. 16, 855 (1966); J. M. Blair et al., Phys. Rev. Lett. 17, 789 (1966); K. J. Foley et al., Phys. Rev. Lett. 19, 397 (1967).

45. G. Yekutieli et al., Nucl. Phys. B38, 605 (1972).

46. H. Bøggild et al., Phys. Letters 30B, 369 (1969).

47. H. Bøggild et al., Nucl. Phys. B32, 119 (1971).

48. If we invoke factorization and assume that the N_2 vertices are of the same type as exist in elastic scattering, then the total cross sections can be related to the I = 1/2 cross sections by the optical theorem.

49. J. G. Rushbrooke, Nuovo Cimento Lett. 2, 181 (1971).

50. The use of reactions (6.4) along with data for the process $pn \to pp\pi^-$ leads to a determination of the I = 0 exchange amplitude in $NN \to NN\pi$. See Ref. 49.

51. See, e.g., M. Jacob and G. Chew, Strong Interaction Physics, (Benjamin, New York, 1964), Chapter 1.

52. See, e.g., R. Hagedorn, Relativistic Kinematics, (Benjamin, New York, 1963), Sections 7-4 and 7-5.

53. For M < 1.6 GeV no off-shell corrections appear to be necessary; see Ref. 29.

54. Pion-Nucleon scattering cross sections can be adequately described by the first four partial waves for M < 1.6 GeV; see Refs. 21 and 29.

55. E. L. Berger et al., Phys. Rev. Letters 20, 964 (1968).

Table I. Proton-proton elastic scattering differential cross sections

-t range (GeV^2)	$d\sigma/dt$ (mb/GeV^2)
0.05 - 0.10	49.1 ± 3.2
0.10 - 0.15	33.9 ± 2.9
0.15 - 0.20	22.5 ± 2.4
0.20 - 0.25	15.2 ± 1.2
0.25 - 0.30	10.0 ± 0.8
0.30 - 0.35	6.76 ± 0.60
0.35 - 0.40	4.39 ± 0.43
0.40 - 0.45	3.20 ± 0.34
0.45 - 0.50	2.58 ± 0.29
0.50 - 0.60	1.54 ± 0.20
0.60 - 0.70	0.86 ± 0.13
0.70 - 0.80	0.41 ± 0.08
0.80 - 0.90	0.32 ± 0.07
0.90 - 1.0	0.16 ± 0.04
1.0 - 2.0	0.057 ± 0.019
2.0 - 3.0	0.010 ± 0.005
3.0 - 4.0	0.005 ± 0.003
4.0 - 5.0	0.002 ± 0.002

Table II. Forward-backward asymmetries of the c.m. angular distributions exhibited in Figs. 6 and 7.

Figure	Particle	N_F	N_B	α
6(a)	p	2330	2754	-0.083 ± 0.013
6(b)	π^0	1430	1112	0.125 ± 0.022
7(a)	p	2998	3426	-0.067 ± 0.012
7(b)	n	3255	3189	0.010 ± 0.013
7(c)	π^+	3080	3344	-0.041 ± 0.012

Table III. Averaged c.m. transverse, longitudinal, and normalized longitudinal momenta for the outgoing particles in $pp \rightarrow p\pi^+n$ at 6.6 GeV/c.

Particle	$\langle P_T \rangle$ (GeV/c)	$\langle P_L \rangle$ (GeV/c)	$\langle \lvert X \rvert \rangle$
p	0.407 ± 0.003	-0.030 ± 0.015	0.700 ± 0.003
n	0.391 ± 0.003	0.020 ± 0.015	0.691 ± 0.003
π^+	0.368 ± 0.003	0.010 ± 0.007	0.307 ± 0.003

Table IV.A Results of fits of the t_p and t_n distributions for reaction (1.3) to the form $dN/dt = Ae^{yt}$.

Distribution	t range (GeV^2)	CL(%)	A	y(GeV^{-2})
proton	0.05 - 0.7	9	2419 ± 71	- 4.4 ± 0.1
proton	0.7 - 1.8	55	189 ± 23	- 0.5 ± 0.1
proton	1.8 - 3.0	50	1473 ± 405	- 1.7 ± 0.1
neutron	0.05 - 0.5	< 1	2160 ± 81	- 4.4 ± 0.2
neutron	0.5 - 3.0	24	551 ± 27	- 1.4 ± 0.1

Table IV.B Results of fits of the t_p and t_n distributions for reaction (1.3) to the form $dN/dt = Ae^{yt} + Be^{zt}$

Quantity	Proton	Neutron
t range (GeV^2)	0.05 - 1.8	0.05 - 3.0
Con. Lev. (%)	35	15
A	2581 ± 87	2404 ± 175
B	107 ± 20	545 ± 32
y(GeV^{-2})	- 5.5 ± 0.2	-8.9 ± 0.7
z (GeV^{-2})	- 0.1 ± 0.1	- 1.4 ± 0.1

Table V. Results of fits of the experimental t_n distributions in $pp \rightarrow (p\pi^+)n$ to the assumed form $\exp(a+bt_n+ct_n^2)$.

$p\pi^+$ mass range (GeV)	t_n range (GeV^2)	CL (%)	Best fit parameters		
			a	b (GeV^{-2})	c (GeV^{-4})
1.08 - 1.16	.02 - .5	56	2.94 ± 0.35	-14.6 ± 4.3	19.8 ± 8.8
1.16 - 1.20	.02 - .5	50	4.02 ± 0.17	-12.6 ± 2.2	10.5 ± 4.8
1.20 - 1.24	.02 - .5	9	4.87 ± 0.11	-14.6 ± 1.4	13.0 ± 3.2
1.24 - 1.28	.02 - .5	85	4.43 ± 0.14	-12.4 ± 1.7	9.5 ± 3.7
1.28 - 1.32	.02 - .5	78	4.20 ± 0.15	-15.0 ± 2.1	15.5 ± 4.8
1.32 - 1.38	.02 - .5	11	4.20 ± 0.15	-16.0 ± 1.9	20.2 ± 4.1
1.38 - 1.48	.02 - .5	11	4.13 ± 0.15	-11.7 ± 2.0	10.6 ± 4.5
1.48 - 1.60	.04 - .7	70	3.76 ± 0.18	- 8.3 ± 1.4	5.3 ± 2.1
1.60 - 1.72	.04 - .7	25	4.16 ± 0.16	-12.3 ± 1.5	11.6 ± 2.3
1.72 - 1.84	.06 - .7	62	4.47 ± 0.18	-10.4 ± 1.4	7.2 ± 2.0
1.84 - 1.96	.08 -1.0	< 1	4.02 ± 0.19	- 6.9 ± 1.1	3.5 ± 1.1
1.96 - 2.08	.12 -1.0	65	3.98 ± 0.25	- 7.1 ± 1.2	4.1 ± 1.2
2.08 - 2.20	.16 -1.0	91	3.52 ± 0.33	- 4.8 ± 1.5	1.8 ± 1.4
2.20 - 2.40	.28 -1.0	2	4.53 ± 0.71	- 6.4 ± 2.7	2.8 ± 2.3
2.40 - 2.60	50 -1.0	10	5.70 ± 2.43	- 9.4 ± 6.8	4.6 ± 4.6

Table VI. Results of fits of the experimental t_p distributions in $pp \rightarrow p(\pi^+ n)$ to the assumed form $\exp(a+bt_p + ct_p^2)$

$\pi^+ n$ mass range (GeV)	t_p range (GeV^2)	CL (%)	Best fit parameters		
			a	b(GeV^{-2})	c(GeV^{-4})
1.08-1.16	.02-.5	40	4.03±0.21	-20.6±2.9	27.4±6.1
1.16-1.22	.02-.5	38	4.26±0.14	-15.9±2.0	18.2±5.1
1.22-1.28	.02-.5	7	4.31±0.15	-11.8±2.0	7.1±5.0
1.28-1.34	.02-.5	76	4.24±0.15	-11.1±2.2	4.5±5.8
1.34-1.40	.02-.5	99	3.97±0.15	-11.0±1.9	9.7±4.2
1.40-1.46	.02-.5	41	3.84±0.15	- 7.1±1.7	7.2±3.8
1.46-1.52	.02-.5	58	3.78±0.15	- 5.6±1.9	- 3.3±4.7
1.52-1.58	.02-.7	75	3.89±0.13	- 8.6±1.3	5.4±2.3
1.58-1.66	.04-.7	80	4.02±0.15	- 7.1±1.4	2.4±2.4
1.66-1.74	.04-.7	83	3.69±0.15	- 3.9±1.3	- 1.6±2.2
1.74-1.84	.06-.7	38	4.00±0.19	- 7.4±1.7	2.1±2.8
1.84-1.96	.08-.7	13	3.95±0.22	- 7.1±1.6	3.1±2.5
1.96-2.08	.12-.7	30	4.47±0.35	- 9.3±2.4	4.6±3.4
2.08-2.22	.16-.7	65	6.19±0.45	-17.8±2.7	14.3±3.5
2.22-2.40	.28-.8	60	7.40±1.18	-18.4±4.8	12.4±4.8

Table VII. Results of fits of the best fit -b and c parameters, displayed in Fig. 22, to the assumed form $x + yM + zM^2$. M represents π^+n effective mass.

		Best fit parameters		
Fit to parameter	CL (%)	x	y	z
-b	55	121.4 ± 14.7	-137.3 ± 18.3	40.8 ± 5.6
c	39	156.1 ± 26.2	-178.6 ± 30.8	51.4 ± 8.9

Table VIII. Differential cross sections for the data of reaction (1.3) which satisfy the cut (5.5).

t_n range (GeV^2)	$d\sigma/dt$ mb/GeV^2	t_n range (GeV^2)	$d\sigma/dt$ mb/GeV^2
< 0.02	12.71 ± 1.09	0.55 - 0.60	0.34 ± 0.08
0.02 - 0.04	12.84 ± 1.11	0.60 - 0.65	0.18 ± 0.06
0.04 - 0.06	11.60 ± 1.02	0.65 - 0.70	0.29 ± 0.07
0.06 - 0.08	7.76 ± 0.76	0.70 - 0.75	0.27 ± 0.07
0.08 - 0.10	7.09 ± 0.72	0.75 - 0.80	0.23 ± 0.07
0.10 - 0.12	4.64 ± 0.54	0.80 - 0.85	0.11 ± 0.04
0.12 - 0.14	3.79 ± 0.47	0.85 - 0.90	0.14 ± 0.05
0.14 - 0.16	4.10 ± 0.50	0.90 - 0.95	0.16 ± 0.05
0.16 - 0.18	2.32 ± 0.35	0.95 - 1.0	0.20 ± 0.06
0.18 - 0.20	2.36 ± 0.36	1.0 - 1.2	0.09 ± 0.02
0.20 - 0.22	2.36 ± 0.36	1.2 - 1.4	0.07 ± 0.02
0.22 - 0.24	1.74 ± 0.30	1.4 - 1.6	0.05 ± 0.02
0.24 - 0.26	1.83 ± 0.31	1.6 - 1.8	0.03 ± 0.01
0.26 - 0.28	1.47 ± 0.27	1.8 - 2.0	0.03 ± 0.01
0.28 - 0.30	1.43 ± 0.27	2.0 - 2.2	0.009 ± 0.006
0.30 - 0.32	1.16 ± 0.24	2.2 - 2.4	0.022 ± 0.010
0.32 - 0.34	1.43 ± 0.27	2.4 - 2.6	0.018 ± 0.009
0.34 - 0.36	1.03 ± 0.22	2.6 - 2.8	0.013 ± 0.008
0.36 - 0.38	1.07 ± 0.23	2.8 - 3.0	0.005 ± 0.005
0.38 - 0.40	0.76 ± 0.19	3.0 - 3.2	0.005 ± 0.005
0.40 - 0.45	0.80 ± 0.13	3.2 - 3.4	0.013 ± 0.008
0.45 - 0.50	0.57 ± 0.11	3.4 - 3.6	0.005 ± 0.005
0.50 - 0.55	0.36 ± 0.08	3.8 - 4.0	0.005 ± 0.005

Table IX. Decay density matrix elements of the $\Delta^{++}(1238)$ in reaction (5.4).

t range (GeV^2)	events	ρ_{33}	$-Re\,\rho_{31}$	$Re\rho_{3,-1}$
0 - .05	714	0.10 ± 0.02	0.16 ± 0.02	0.02 ± 0.02
0.05 - 0.10	452	0.12 ± 0.03	0.11 ± 0.03	-0.05 ± 0.03
0.10 - 0.15	221	0.21 ± 0.04	0.20 ± 0.04	-0.05 ± 0.04
0.15 - 0.20	165	0.06 ± 0.05	0.14 ± 0.04	0.02 ± 0.04
0.20 - 0.30	198	0.14 ± 0.04	0.06 ± 0.04	0.02 ± 0.04
0.30 - 0.50	199	0.16 ± 0.04	0.09 ± 0.04	0.00 ± 0.04
0.50 - 1.0	127	0.28 ± 0.05	0.04 ± 0.05	-0.03 ± 0.05

Table X. Results of fits of "tσ" points to the assumed forms for $1.12 < M(p\pi^+) < 1.42$ GeV.

π^+p mass range (GeV)	Averaged on-shell $\sigma(\pi^+p)$ (mb)	Extrapolated cross section σ_{π^+p} DP-OPE "tσ" = bt fit	Extrapolated cross section σ_{π^+p} Conventional "tσ" = bt + ct^2 fit
1.12 - 1.18	47	48 ± 5	107 ± 18
1.18 - 1.20	140	149 ± 15	169 ± 39
1.20 - 1.22	195	202 ± 16	255 ± 41
1.22 - 1.24	197	232 ± 17	265 ± 39
1.24 - 1.26	157	163 ± 14	222 ± 33
1.26 - 1.28	116	110 ± 11	106 ± 22
1.28 - 1.32	79	83 ± 7	83 ± 12
1.32 - 1.36	49	55 ± 5	52 ± 10
1.36 - 1.42	30	33 ± 3	29 ± 5
FWHM (GeV)	0.100	0.100	0.085
Fit to data	χ^2/DF (Prob.)	69/55(10%)	57/46 (15%)
Agreement with $\sigma_{\text{on-shell}}$	χ^2/DF (Prob.)	8.1/9(52%)	20.6/9 (~ 1.5%)

Table XI. Results of fits of "$t\sigma$" points to the assumed forms for $1.42 < M(p\pi^+) < 2.02$ GeV.

π^+p mass range (GeV)	Averaged on-shell $\sigma_{\pi+p}$(mb)	Extrapolated cross sections $\sigma_{\pi+p}$: DP-OPE "$t\sigma$" = bt fit	DP-OPE "$t\sigma$" = $bt+ct^2$ fit	Conventional "$t\sigma$" = $bt + ct^2$ fit
1.42 - 1.48	17.3	25.2 ± 2.5	23.3 ± 6.8	19.4 ± 4.3
1.48 - 1.54	11.1	15.3 ± 1.8	9.9 ± 4.3	10.0 ± 2.7
1.54 - 1.62	8.2	11.7 ± 1.3	10.1 ± 3.6	8.6 ± 2.2
1.62 - 1.70	11.4	13.9 ± 1.4	8.8 ± 4.4	8.0 ± 2.6
1.70 - 1.78	13.8	13.8 ± 1.3	9.0 ± 4.2	8.2 ± 2.4
1.78 - 1.86	16.6	15.5 ± 1.3	19.3 ± 5.1	13.4 ± 2.6
1.86 - 1.94	19.0	15.6 ± 1.4	25.7 ± 6.6	15.1 ± 3.2
1.94 - 2.02	16.2	13.3 ± 1.4	23.4 ± 8.6	13.4 ± 3.9
Fit to data	χ^2/DF(Prob.)	38.7/38(45%)	29.1/30(52%)	27.9/30 (57%)
Agreement with $\sigma_{\text{on-shell}}$	χ^2/DF(Prob.)	36.4/8(< 0.1%)	4.7/8(79%)	11.1/8 (20%)

Table XII. Comparison of Experimental and Theoretical Cross Sections for reaction (1.3)

$M(p\pi^+)$ region (GeV)	All data		Peripheral data							
	No. of events	Expt. cross section (mb)	t_n cut (GeV^2)	t_p cut (GeV^2)	No. of events	Expt. cross section (mb)	DP-OPE Int. cross section (mb) Proc. A	Proc B	DRP Int. cross section (mb) Case C	Case D
1.14 - 1.42	2166	1.93 ± 0.13	< 0.4	-	1872	1.67 ± 0.11	1.57	0.08	-	-
1.42 - 2.00	2121	1.89 ± 0.13	< 0.6	< 0.6	1151	1.03 ± 0.07	0.84	0.16	0.40	1.65
2.00 - 2.86	2137	1.91 ± 0.13	< 0.8	< 0.4	769	0.69 ± 0.05	0.48	0.09	0.18	1.07

Table XIII. Branching ratios of the enhancements near 1.46 and 1.65 GeV.

		R expected	
Mass (GeV)	$R(p\pi^0/\pi^+n)$	$I = \frac{1}{2}$	$I = \frac{3}{2}$
1.462	0.50 ± 0.08	0.5	2
1.65	0.77 ± 0.12	0.5	2

Table XIV. Best fit parameters obtained in fits of the Fig. 37 data to the assumed form $A \exp(bt + ct^2)$.

Data	b (GeV^{-2})	c (GeV^{-4})
Fig. 37(a)	-9.2 ± 1.5	6.7 ± 3.1
Fig. 37(b)	-7.7 ± 3.4	3.4 ± 7.0

FIGURE CAPTIONS

Fig. 1. Experimental distributions of $\phi[=\tan^{-1}(P_z/P_x)]$ for $pp \to pp$ events with four-momentum transfer squared $|t|$ in the ranges: (a) 0-.05 GeV^2, (b) 0.05-0.10 GeV^2, (c) 0.10-0.15 GeV^2, (d) 0.15-0.20 GeV^2. The smooth curves are $a + b|\cos\phi|$ where a and b are best fit values obtained in least-squares fits to the data.

Fig. 2. Elastic scattering differential cross section plotted as a function of t.

Fig. 3. Experimental missing-mass-squared distribution for the 2591 events accepted to be examples of reaction (1.2).

Fig. 4. Experimental cross section for reaction (1.2) as a function of beam momentum.

Fig. 5. Experimental cross section for reaction (1.3) as a function of beam momentum. The solid curve represents the expansion $\sigma = 45.9\ (|\vec{P}_{Lab}|)^{-1.06}$ mb.

Fig. 6. Single particle c.m. angular distributions for 2542 reaction (1.2) events. (a) proton, two points per event, (b) π^0.

Fig. 7. Single particle c.m. angular distributions for the 6424 reaction (1.3) events. (a) proton, (b) neutron, (c) π^+.

Fig. 8. Peyrou plots of c.m. longitudinal- vs. c.m. transverse momenta for the 6424 reaction (1.3) events. (a) proton, (b) neutron, (c) π^+

Fig. 9. (a)-(c) Projections of c.m. transverse momenta for the 6424 reaction (1.3) events. (d)-(f) corresponding projections of normalized longitudinal momenta, $X = P_L/P_{max}$ where P_{max} is the maximum allowed longitudinal momentum.

Fig. 10. Distributions of the averaged transverse momenta vs. X for the reaction (1.3) data (a) proton, (b) neutron, (c) π^+.

Fig. 11. Longitudinal phase-space plot (see Ref. 12) for the 6424 reaction (1.3) events. The hexagonal border represents the limiting case of no transverse momenta and infinite energy.

Fig. 12. Distributions of t, defined by Eq. (5.2), for the 6424 reaction (1.3) events. The curves in (a) and (b) represent the expansion (5.3) using the best-fit parameters obtained in least-squares fits to the data.

Fig. 13. Dalitz plot for the 6424 reaction (1.3) events.

Fig. 14. (a) $p\pi^+$, (b) π^+n, and (c) pn effective mass projections for the 6424 reaction (1.3) events.

Fig. 15. Chew-Low plot of $M(p\pi^+)$ vs. t_n for the 6424 reaction (1.3) events.

Fig. 16. $M(p\pi^+)$ projections of Fig. 15 for the four denoted ranges of t_n.

Fig. 17. t_n projections of Fig. 15 for the fifteen denoted ranges of $M(p\pi^+)$. The smooth curves represent the expansion $\exp(a+bt_n+ct_n^2)$ using for a, b, and c the best-fit values listed in columns 4, 5, and 6 of Table V, respectively.

Fig. 18. (a),(b): The best-fit values of the parameters (-b) and c, respectively, plotted as a function of $M(p\pi^+)$. The parameters are listed in columns 5 and 6 of Table V, respectively.

Fig. 19. Chew-Low plot of $M(\pi^+n)$ vs. t_p for the 6424 reaction (1.3) events.

Fig. 20. $M(\pi^+n)$ projections of Fig. 19 for the four denoted ranges of t_p.

Fig. 21. t_p projections of Fig. 19 for the fifteen denoted ranges of $M(\pi^+n)$. The smooth curves represent the expansion $\exp(a+bt_p+ct_p^2)$, using for a, b, and c the best-fit values listed in columns 4, 5, and 6 of Table VI, respectively.

Fig. 22. (a),(b): The best fit values of the parameters (-b) and c, respectively, plotted as a function of $M(\pi^+n)$. The parameters are listed in columns 5 and 6 of Table VI, respectively. The smooth curves drawn in parts (a) and (b) represent the expansion $x + yM + zM^2$, using for x, y, and z the best-fit values listed in Table VII.

Fig. 23. Differential cross section for reaction (5.4) plotted as a function of t_n. Only events with $1.14 < M(p\pi^+) < 1.42$ GeV are used.

Fig. 24. (a)-(c) Decay density matrix elements for the reaction (5.4) data, plotted as a function of t_n. (d) t-channel coordinate system (Ref. 17); $\vec{P}_{in}(\vec{P}_{out})$ represents the incoming (outgoing) proton as seen in the $\Delta^{++}(1238)$ rest system; $\vec{n}$ is the direction of the normal to the production plane for the overall scattering process.

Fig. 25. (a)-(h): A_ℓ/A_0 moments [defined in Eq. (5.8)] of the $p\pi^+$ quasi-elastic scattering angular distribution for $\ell \leq 8$, plotted as a function of $M(p\pi^+)$ for peripheral $p\pi^+$ systems with $|\cos\theta_n| > 0.965$. The solid curves represent the on-mass-shell $p\pi^+$ elastic scattering moments, which are calculated from the CERN phase shifts (Ref. 21).

Fig. 26. (a) Extrapolated $\pi^+ p$ elastic-scattering cross sections, obtained in least-squares fits of the experimental "$t\sigma$" points, calculated with Eq. (5.11), to the assumed form $bt + ct^2$. The values plotted are also listed in columns 4 and 5 of Tables X and XI, respectively. (b) Extrapolated $\pi^+ p$ elastic-scattering cross sections, obtained in least-squares fits of the experimental "$t\sigma$" points, calculated with Eq. (5.14), to the assumed forms bt (solid dots) and $bt + ct^2$ (open circle points). The values plotted are also listed in column 3 of Table X and columns 4 and 5 of Table XI. The solid curves drawn in both (a) and (b) represent the known (Ref. 27) $\pi^+ p$ elastic scattering cross section behavior.

Fig. 27. (a)-(i): Experimental "$t\sigma$" points, calculated using Eq. (5.14) for the nine indicated $M(p\pi^+)$ bins with $1.12 < M(p\pi^+) < 1.42$ GeV, and plotted as a function of t to the neutron. The line drawn in each component figure represents the form bt using for b the best fit value listed in column 3 of Table X; the points at $t = -\mu^2$ represent the extrapolated value of "$t\sigma$" or $-b\mu^2$.

Fig. 27. (j)-(q): Experimental "$t\sigma$" points, calculated using Eq. (5.14), for the eight indicated $M(p\pi^+)$ bins with $1.42 < M(p\pi^+) < 2.02$ GeV, and plotted as a function of t to the neutron. The curves drawn in each component figure represent the bt and $bt + ct^2$ forms using the best fit values for the parameters b and c; the points at $t = -\mu^2$ represent the extrapolated value of the function whose curve passes through the central value.

Fig. 28. Exchange diagrams for reaction (1.3): Processes A and B represent single π^+ and π^0 exchange, respectively. Process C represents a Double-Regge-Pole (Ref. 35) exchange process with Pomeranchuk (P) and π exchanges.

Fig. 29. (a)-(d) Experimental differential cross sections of $M(p\pi^+)$, $M(\pi^+n)$, t_n, and t_p, respectively, for the 2166 events of reaction (1.3) with $1.14 < M(p\pi^+) < 1.42$ GeV. The cross-hatched distributions are plotted for the 1872 events with $t_n < 0.4$ GeV^2. The solid curves represent the Dürr-Pilkuhn (DP-OPE) model predictions to the shaded data (See Section VG and the Appendix).

Fig. 30. (a)-(d) Experimental differential cross sections of $M(p\pi^+)$, $M(\pi^+n)$, t_n, and t_p, respectively, for the 2121 events of reaction (1.3) with $1.42 < M(p\pi^+) < 2.0$ GeV. The cross-hatched distributions are plotted for the 1151 events with both t_n and $t_p < 0.6$ GeV^2. The solid and dashed curves represent the DP-OPE and normalized Double-Regge-Pole (DRP) (Ref. 35) model predictions to the shaded data, respectively. (see Section VG and the Appendix).

Fig. 31. (a)-(d) Experimental differential cross sections of $M(p\pi^+)$, $M(\pi^+n)$, t_n, and t_p, respectively, for the 2137 events of reaction (1.3) with $M(p\pi^+) > 2.0$ GeV. The cross-hatched distributions are plotted for the 769 events with $t_n < 0.8$ GeV^2 and $t_p < 0.4$ GeV^2. The solid and dashed curves represent the DP-OPE and normalized DRP predictions to the shaded data, respectively (See Section VG and the Appendix).

Fig. 32. (a)-(f) Experimental differential cross sections of $\cos\theta_p$, $\cos\theta_n$, ϕ_p, ϕ_n, $t_{p_p\pi^+}$, and $t_{p_n\pi^+}$, respectively, for the 1872

events of reaction (1.3) with $1.14 < M(p\pi^+) < 1.42$ GeV and with $t_n < 0.4$ GeV^2. $(\theta_p, \phi_p)/(\theta_n,\phi_n)$ represent the (polar, azimuthal) angles of the proton/neutron in the π^+p/π^+n rest systems using the standard t-channel coordinate system (Ref. 39). $t_{p_i\pi^+}$ represents the momentum transfer to the outgoing π^+ from the incoming proton associated with the outgoing i^{th} nucleon. The solid curves represent the DP-OPE productions (see Sec. VG and the Appendix).

Fig. 33. (a)-(f) Experimental differential cross sections of $\cos\theta_p$, $\cos\theta_n$, ϕ_p, ϕ_n, $t_{p_p\pi^+}$, and $t_{p_n\pi^+}$, respectively, for the 1151 events of reaction (1.3) with $1.42 < M(p\pi^+) < 2.0$ GeV and with both t_n and $t_p < 0.6$ GeV^2. The plotted quantities are defined as in Fig. 32. The solid and dashed curves represent the DP-OPE and normalized DRP productions, respectively (see Sec. VG and the Appendix).

Fig. 34. (a)-(f) Experimental differential cross sections of $\cos\theta_p$, $\cos\theta_n$, ϕ_p, ϕ_n, $t_{p_p\pi^+}$, and $t_{p_n\pi^+}$, respectively, for the 769 events of reaction (1.3) with $M(p\pi^+) > 2.0$ GeV and with $t_n < 0.8$ GeV^2 and $t_p < 0.4$ GeV^2. The plotted quantities are defined as in Fig. 32. The solid and dashed curves represent the DP-OPE and normalized DRP predictions, respectively (see Sec. VG and the Appendix).

Fig. 35. (a) $M(p\pi^0)$ distribution for the 2591 reaction (1.2) events. Each event is plotted twice. (b) $M(\pi^+n)$ spectrum for a subsample of 5324 reaction (1.3) events.

Fig. 36. (a) $M(\pi^+n)$ spectrum for reaction (1.3) events with $M(p\pi^+) >$ 2.4 GeV. (b) $M(p_i\pi^0)$ distribution for reaction (1.2) events with $M(p_j\pi^0) > 2.4$ GeV ($i \neq j$). (c) The sum of (a) and (b). The solid curves represent fits to a quadratic background plus two Breit-Wigner functions (see Sec. VIA).

Fig. 37. t distributions of N*(1460) combinations for data with mass between 1.402 and 1.51 GeV. (a) all events (π^+n and $p\pi^0$); (b) events with a mass cut (>2.4 GeV) made on the other πN combination.

Fig. 38. $d\sigma/dM(N_1\pi)$ for $pp \to N_1\pi N_2$ at 6.6 GeV/c for $M(N_1\pi) < M(N_2\pi)$. (a) $|A_3|^2$, (b) $|A_1|^2$, (c) $Re(A_1A_3^*)$ where these quantities are calculated using Eq. (6.5).

Fig. 39. Experimental differential cross sections of t_n for data with: (a) $1.42 < M(p\pi^+) < 2.0$ GeV and $t_p < 0.6$ GeV^2; (b) $M(p\pi^+) >$ 2.0 GeV and $t_p < 0.4$ GeV^2. The solid (case C) and dashed (case D) curves represent the normalized DRP predictions using for the quantity X in Eq. (A9) the choices $t_n[\Gamma(1)\Gamma(3/2+\alpha)/\Gamma(3/2)\Gamma(1+\alpha)]^2$ and μ^2, respectively (see Appendix).

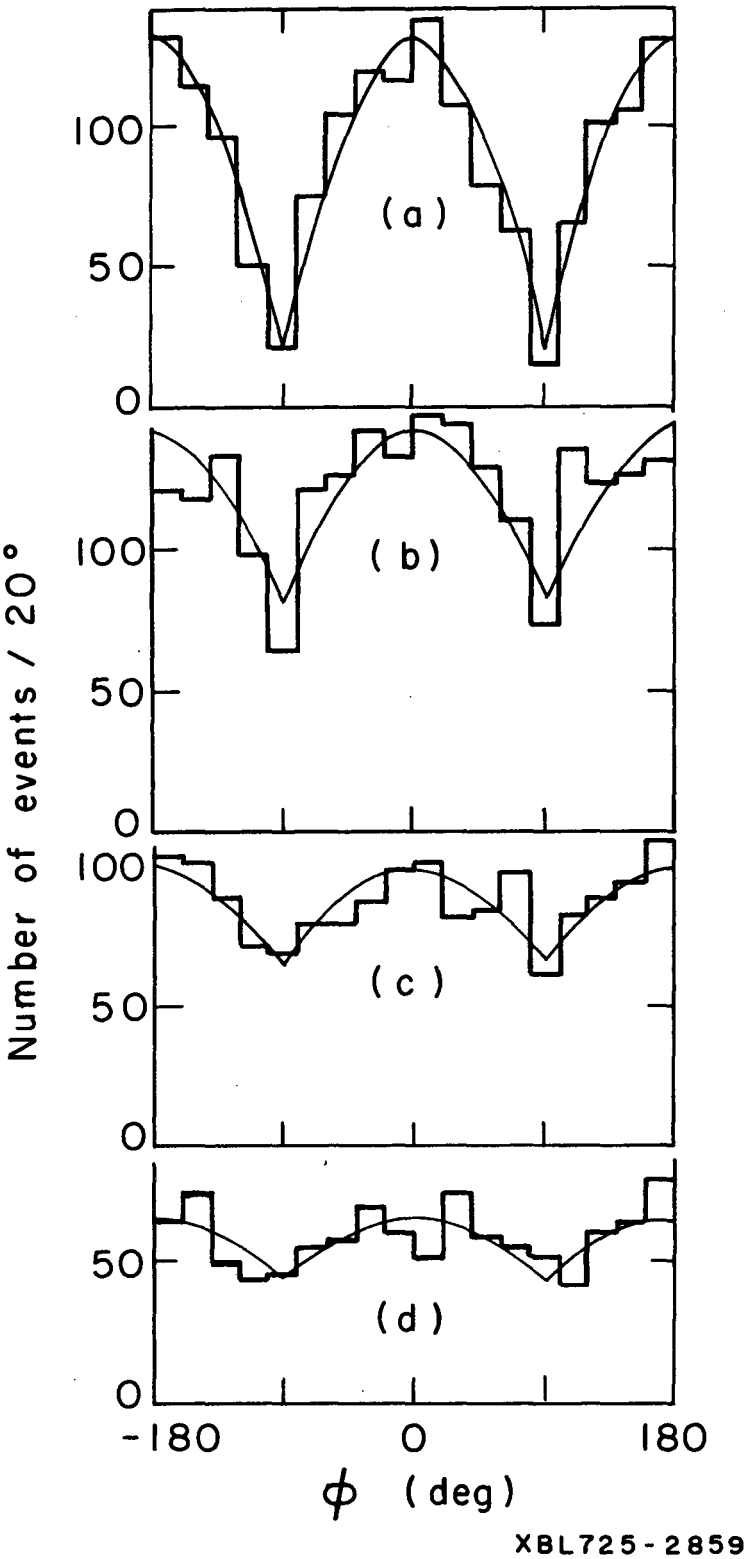
100
50
0
(a)
100
50
0
(b)
100
50
0
(c)
50
0
(d)
Number of events / 20°
-180
0
180
φ (deg)
XBL725-2859

FIGURE 1

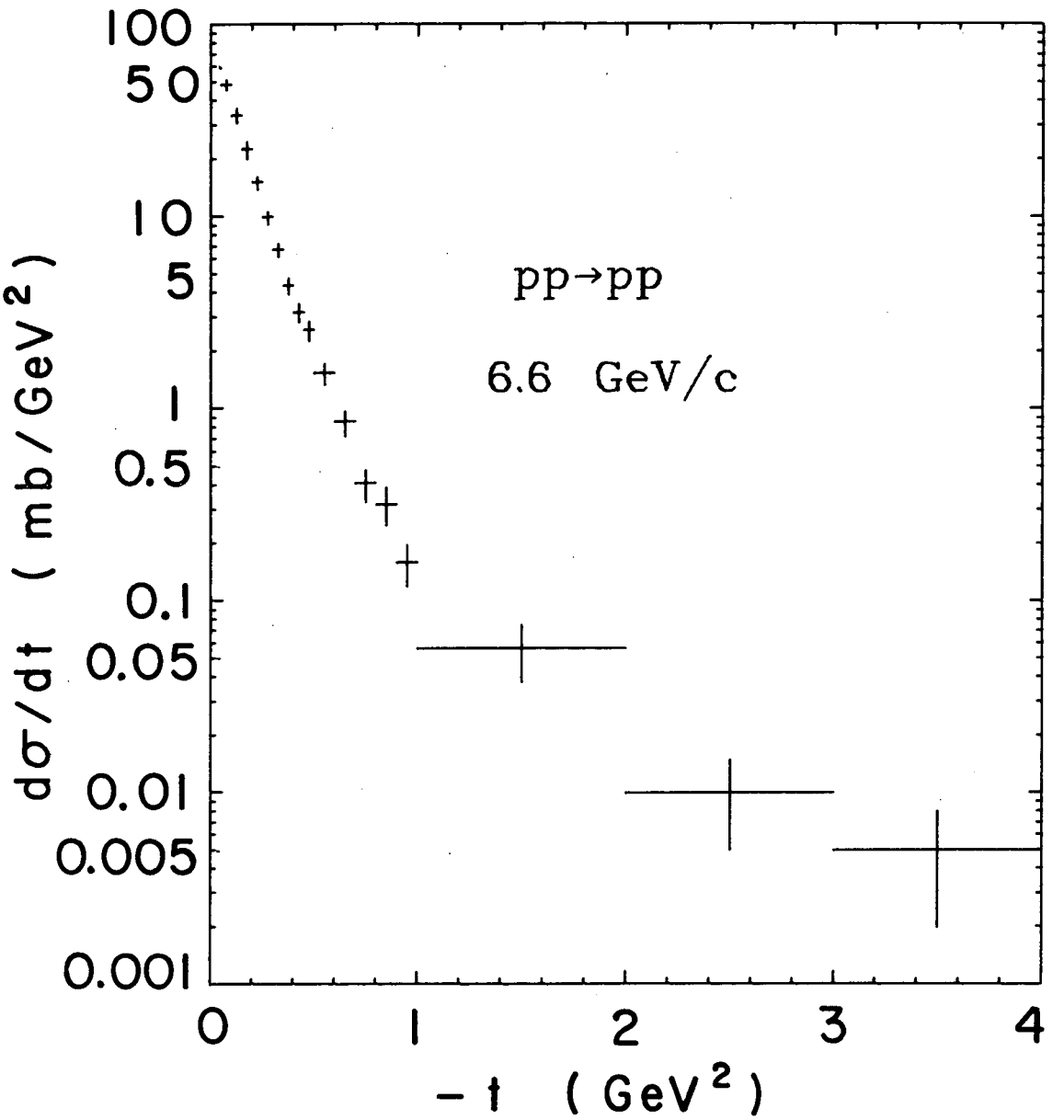

XBL725-2857

FIGURE 2

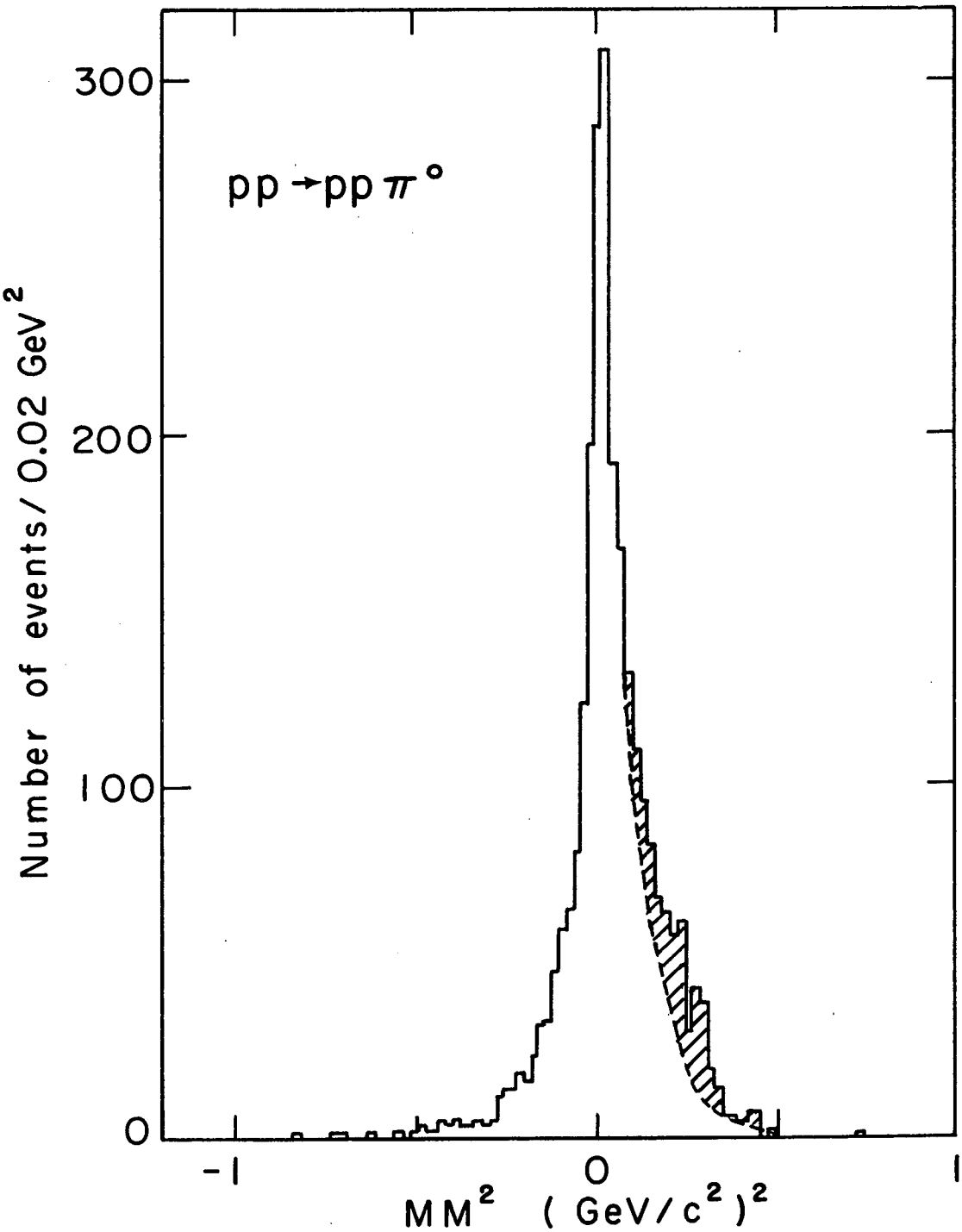

XBL725-2860

FIGURE 3

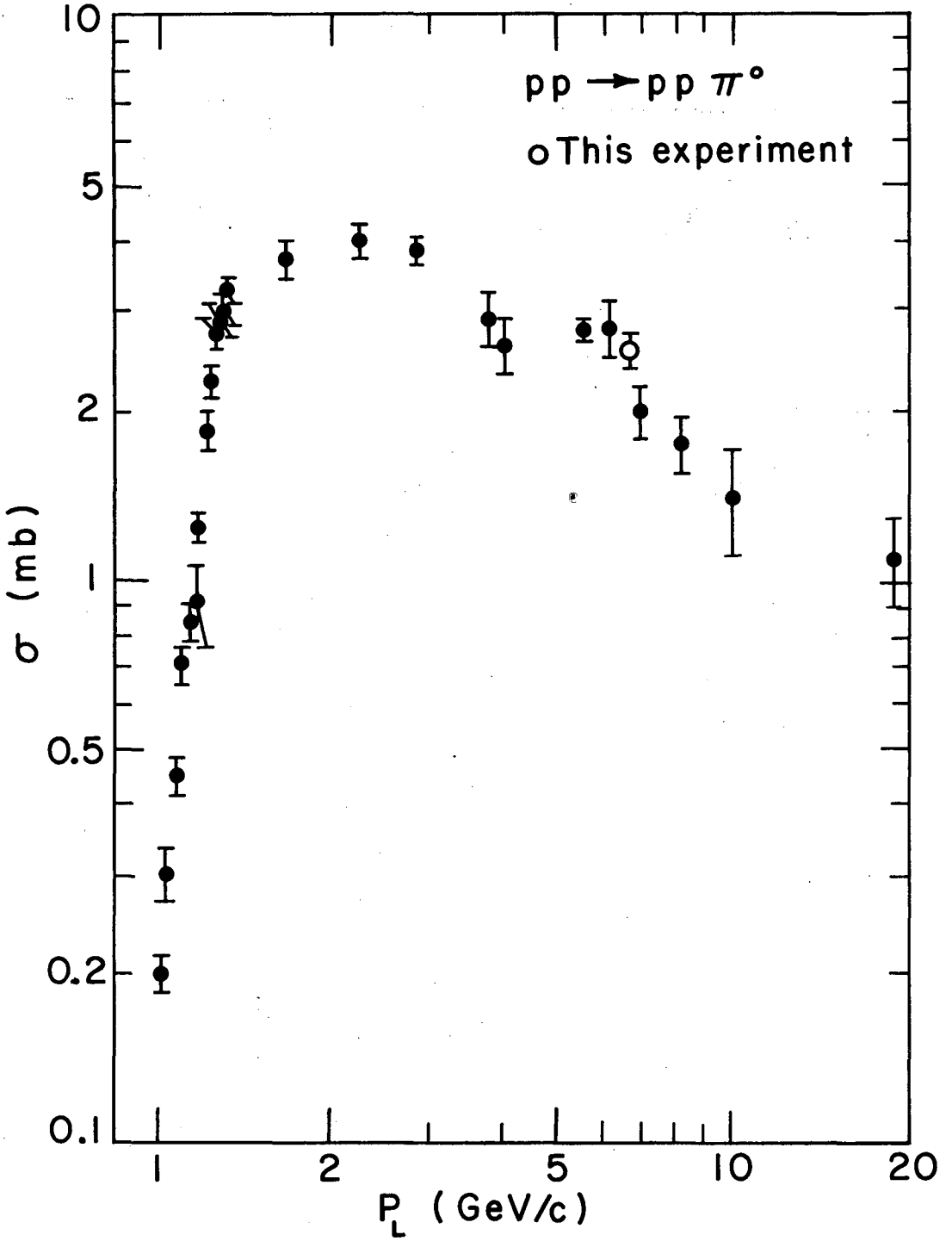

XBL725-2861

FIGURE 4

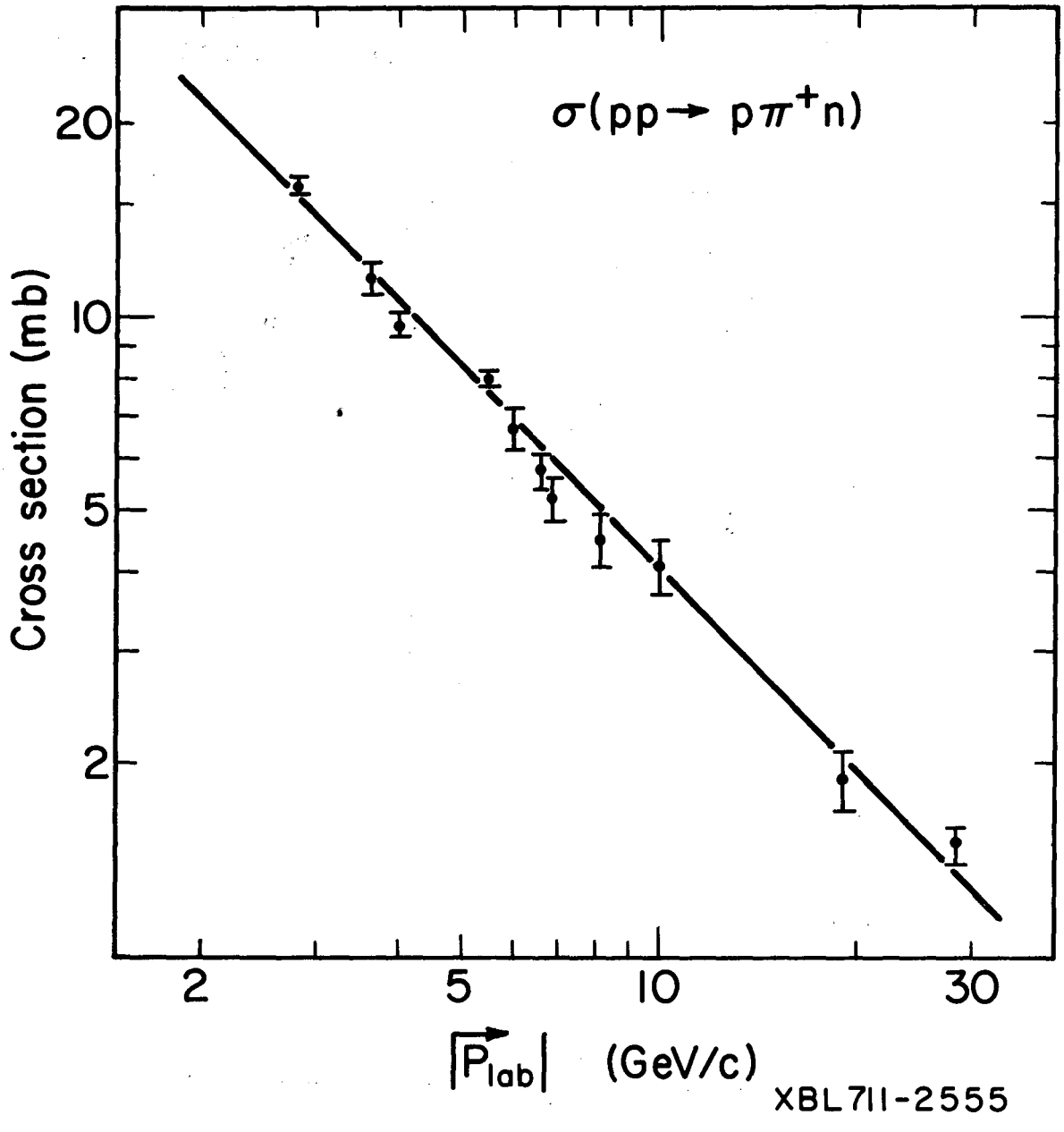
σ(pp→ pπ+n)
Cross section (mb)
20
10
5
2
2
5
10
30
|P⃗lab| (GeV/c)
XBL711-2555

FIGURE 5

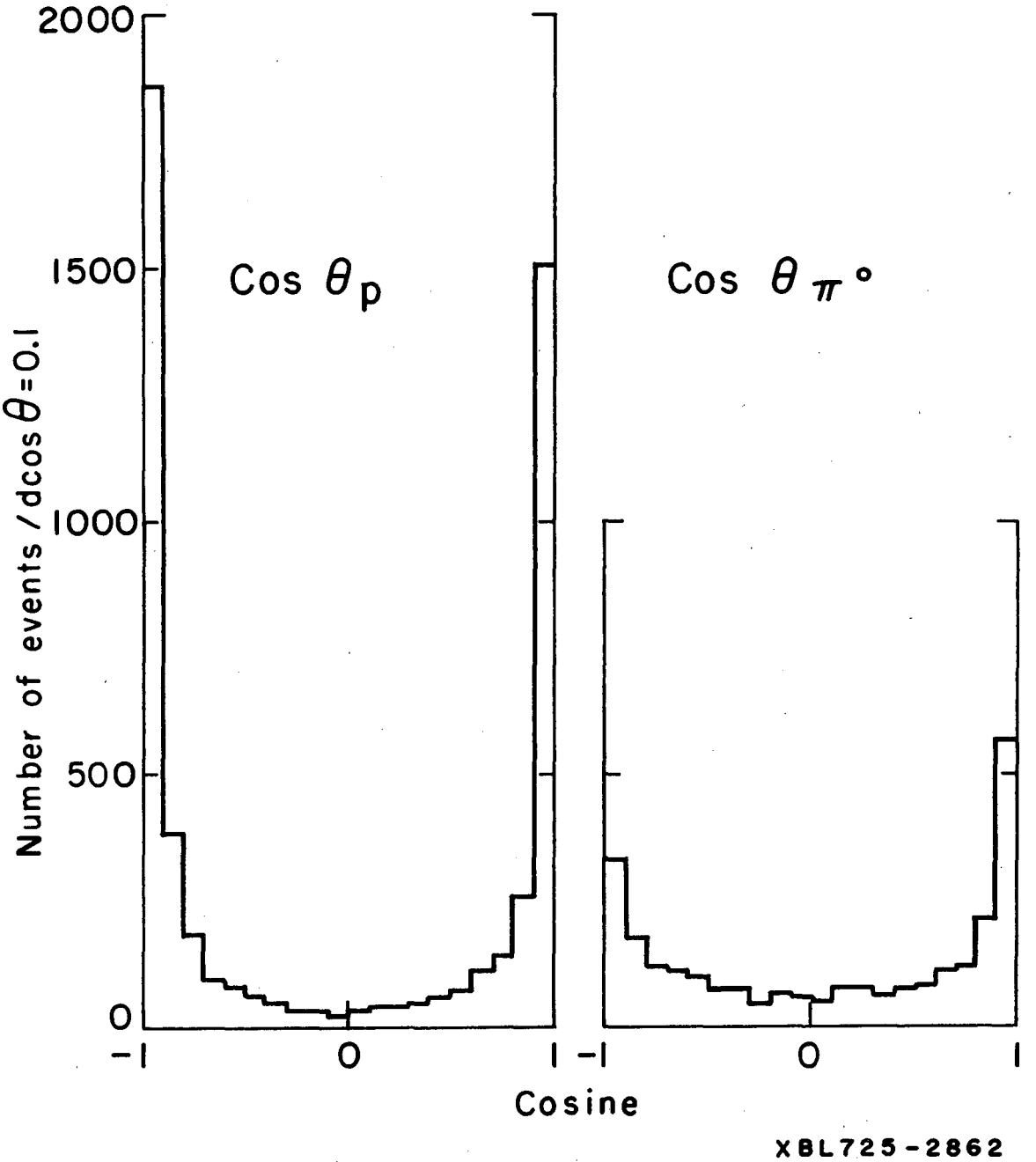
2000
1500
1000
500
0
Number of events / dcos θ=0.1
Cos θ p
Cos θ π°
-1
0
1
-1
0
1
Cosine
XBL725-2862

FIGURE 6

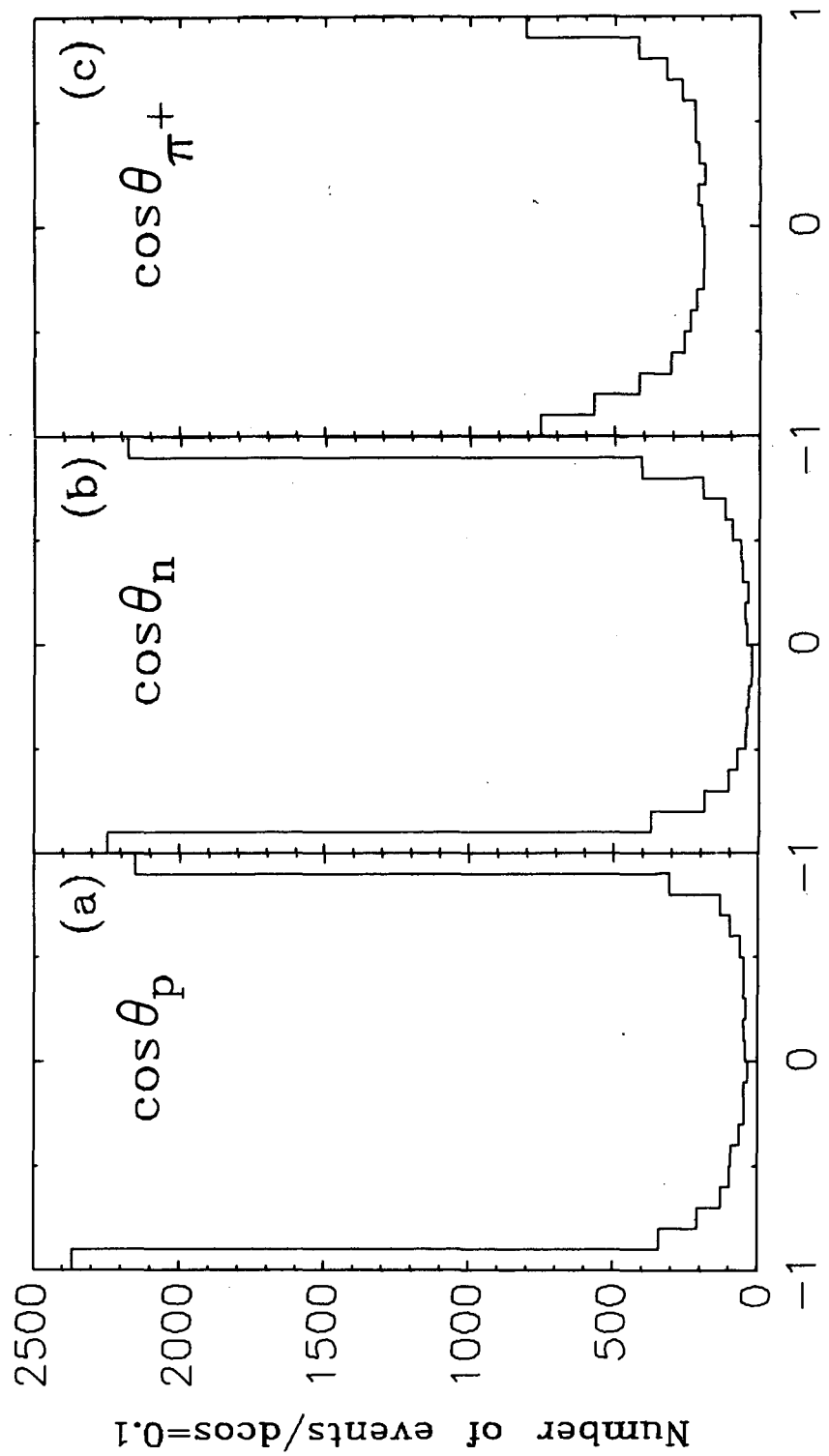

XBL711-2567

FIGURE 7

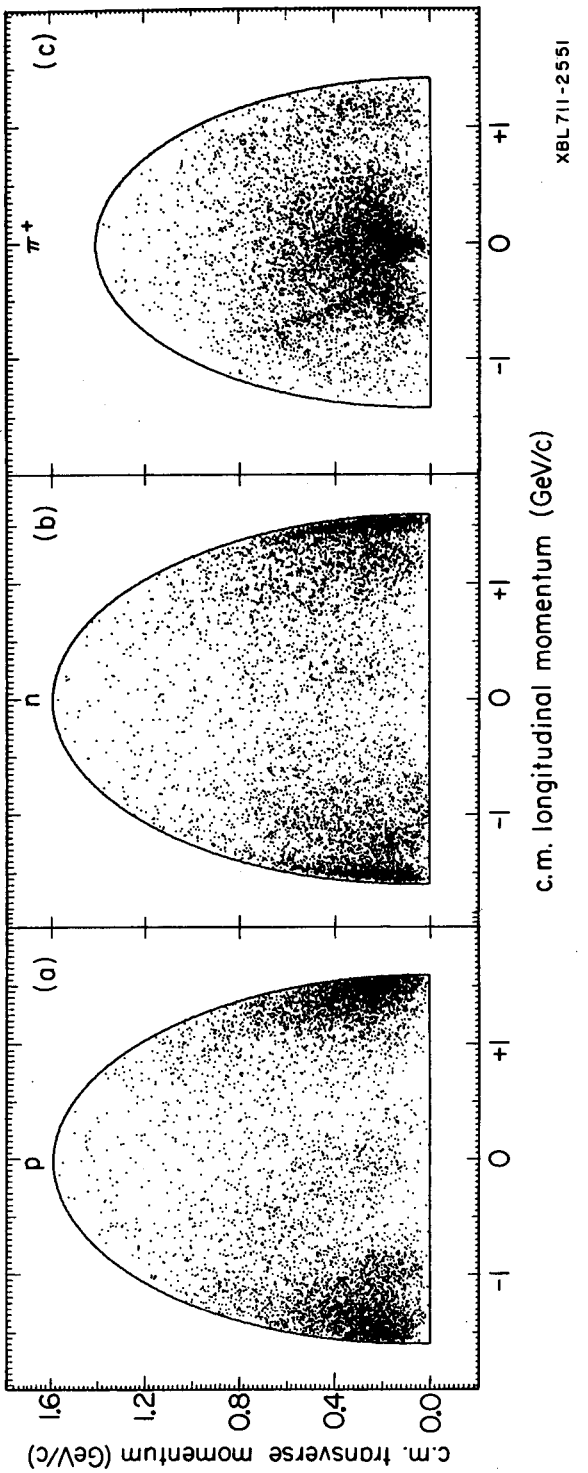
c.m. transverse momentum (GeV/c)
0.0
0.4
0.8
1.2
1.6
(a)
p
(b)
n
(c)
π^+
−1
0
+1
c.m. longitudinal momentum (GeV/c)
XBL711-2551

FIGURE 8

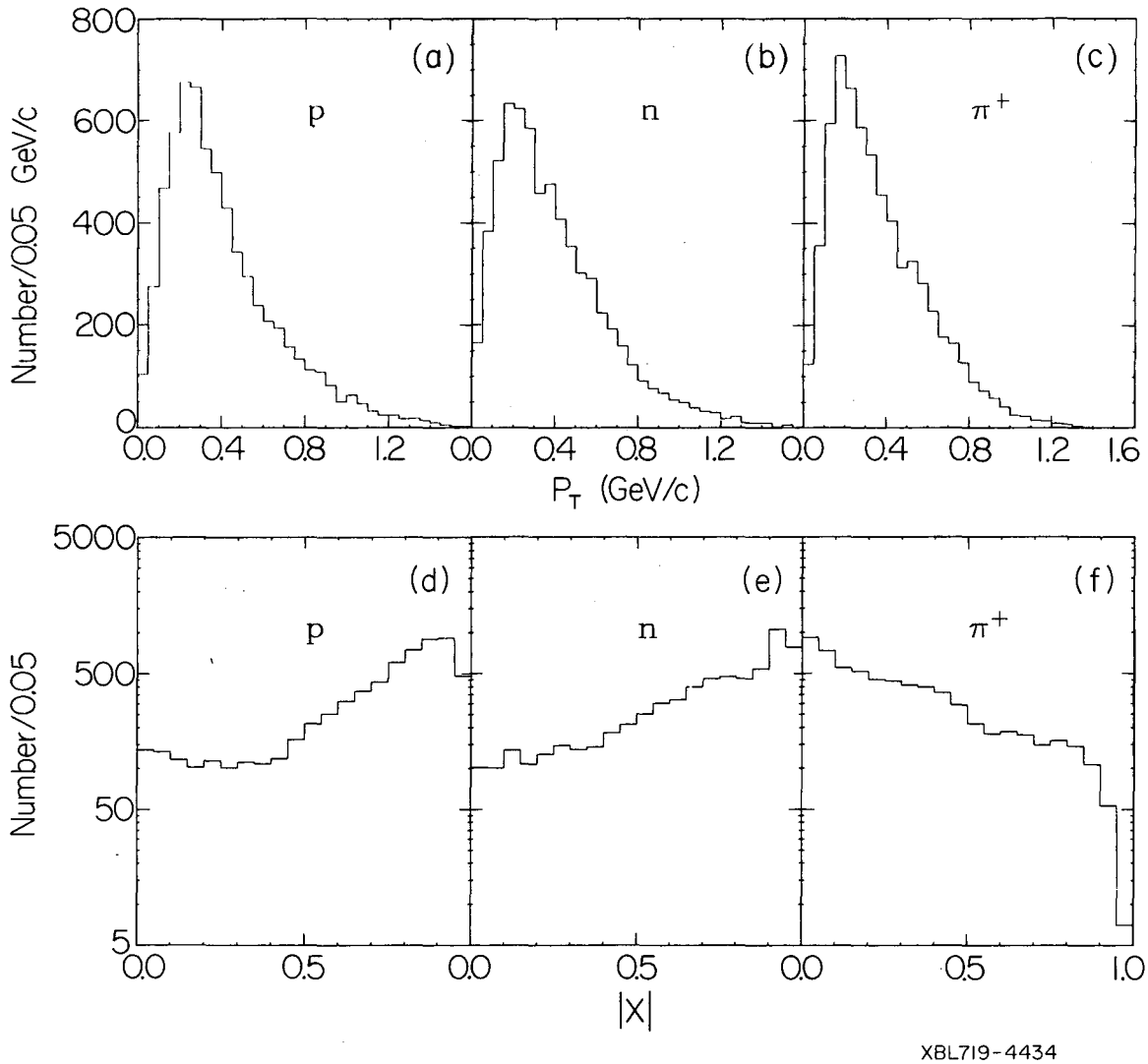
(a)
p
(b)
n
(c)
π^+
Number/0.05 GeV/c
800
600
400
200
0
0.0
0.4
0.8
1.2
1.6
P_T (GeV/c)
(d)
p
(e)
n
(f)
π^+
Number/0.05
5000
500
50
5
0.5
1.0
|X|
XBL719-4434

FIGURE 9

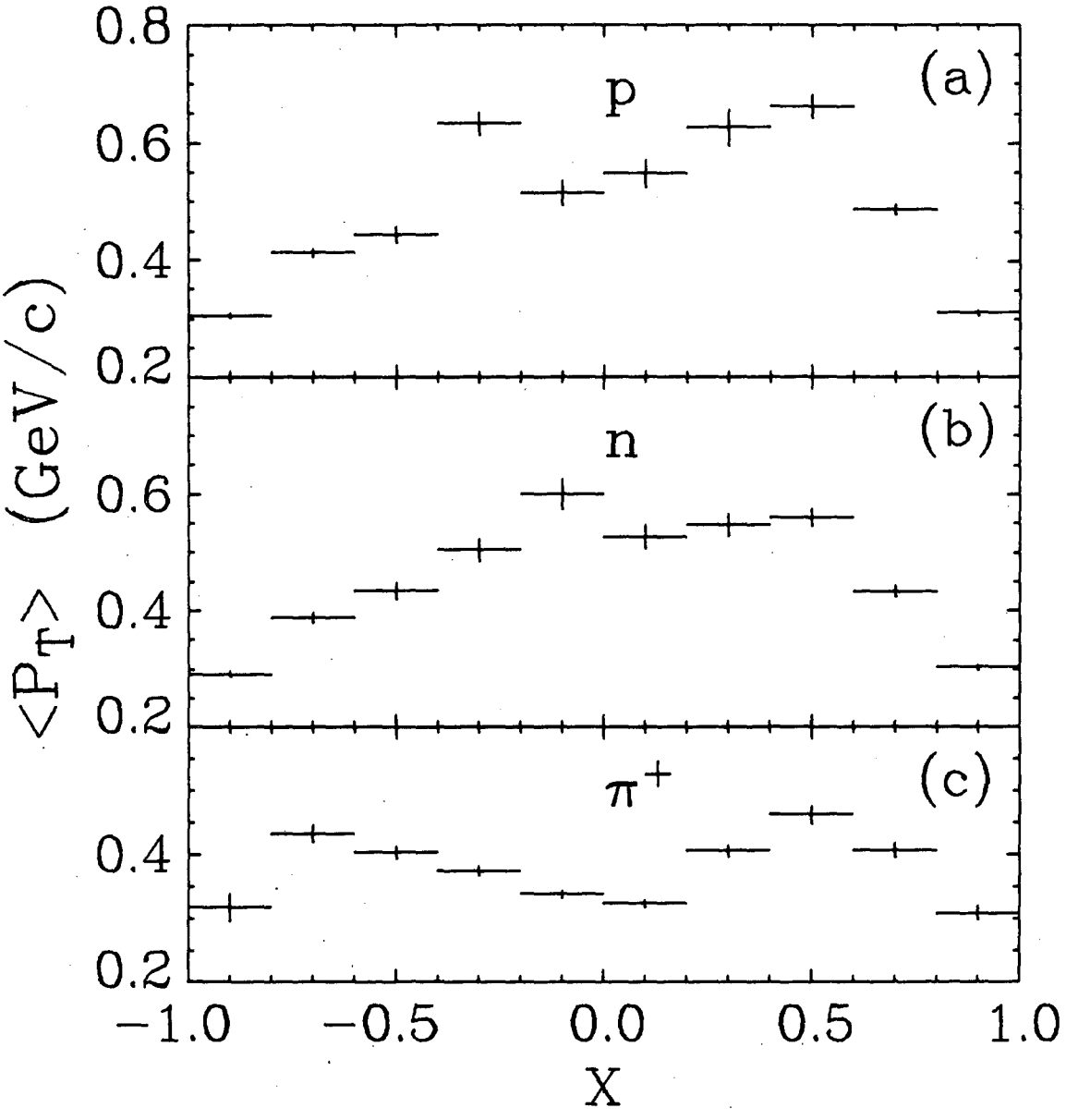

FIGURE 10

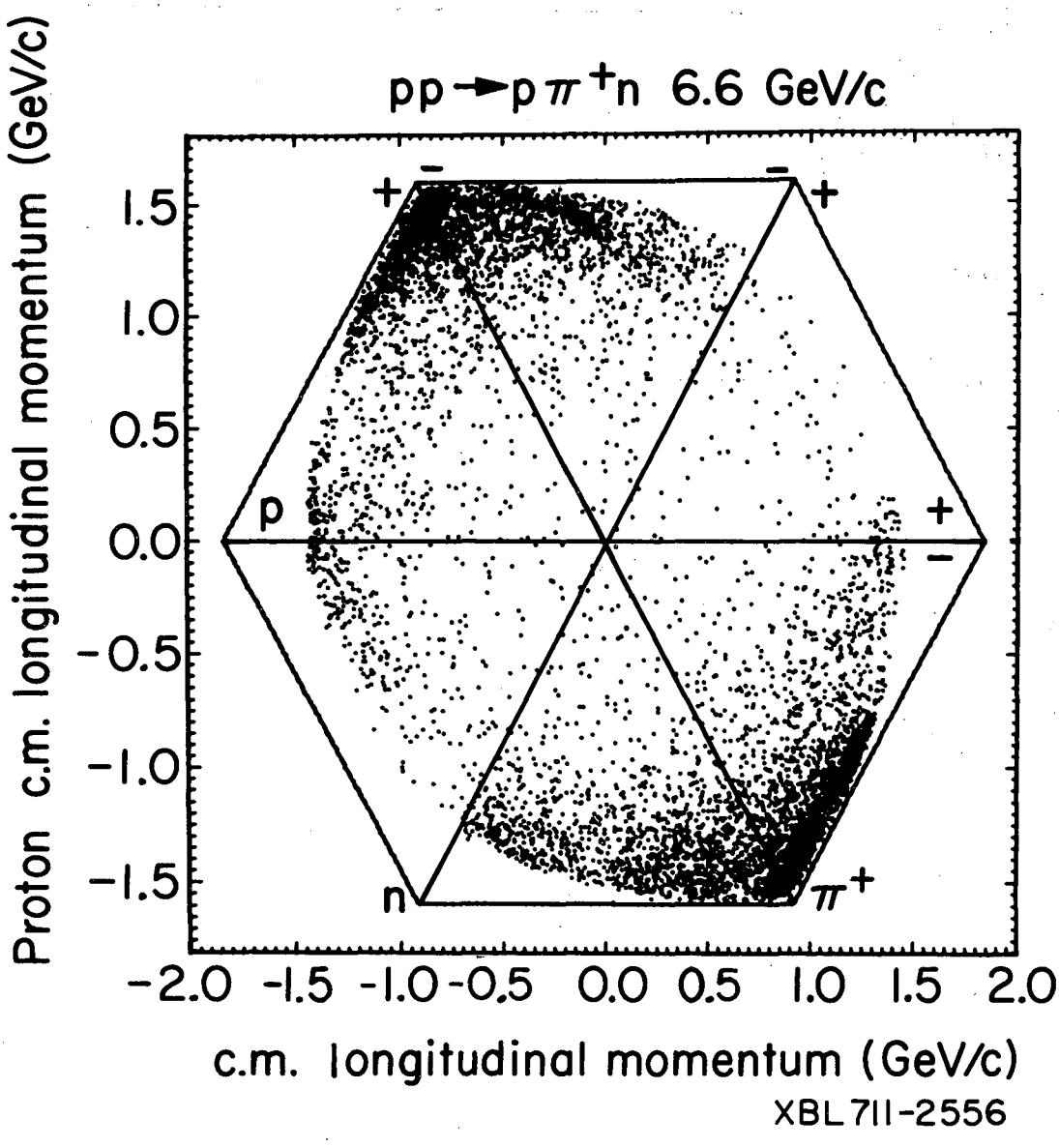
pp → pπ+n 6.6 GeV/c
Proton c.m. longitudinal momentum (GeV/c)
1.5
1.0
0.5
0.0
-0.5
-1.0
-1.5
-2.0 -1.5 -1.0 -0.5 0.0 0.5 1.0 1.5 2.0
c.m. longitudinal momentum (GeV/c)
p
n
π+
+
−
−
+
+
−
XBL 711-2556

FIGURE 11

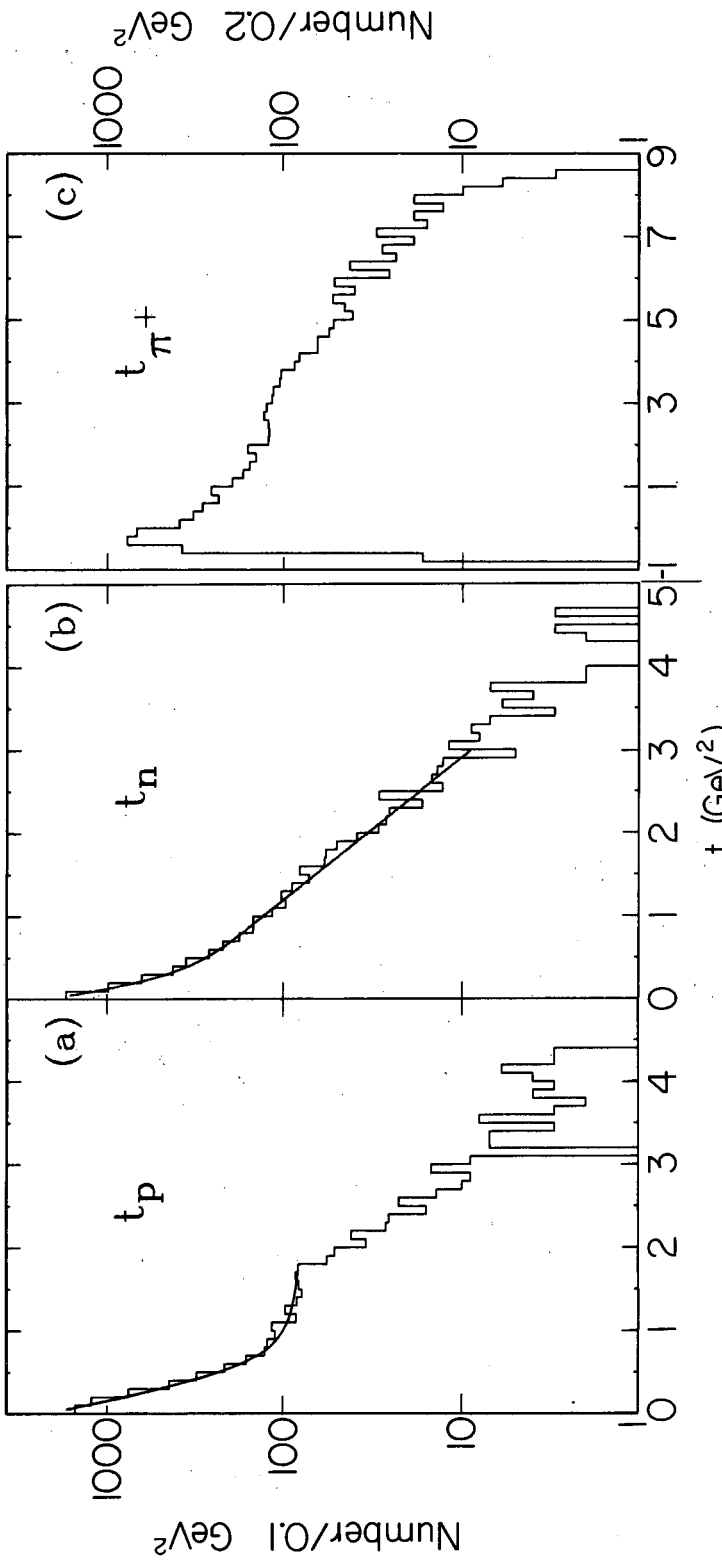

FIGURE 12

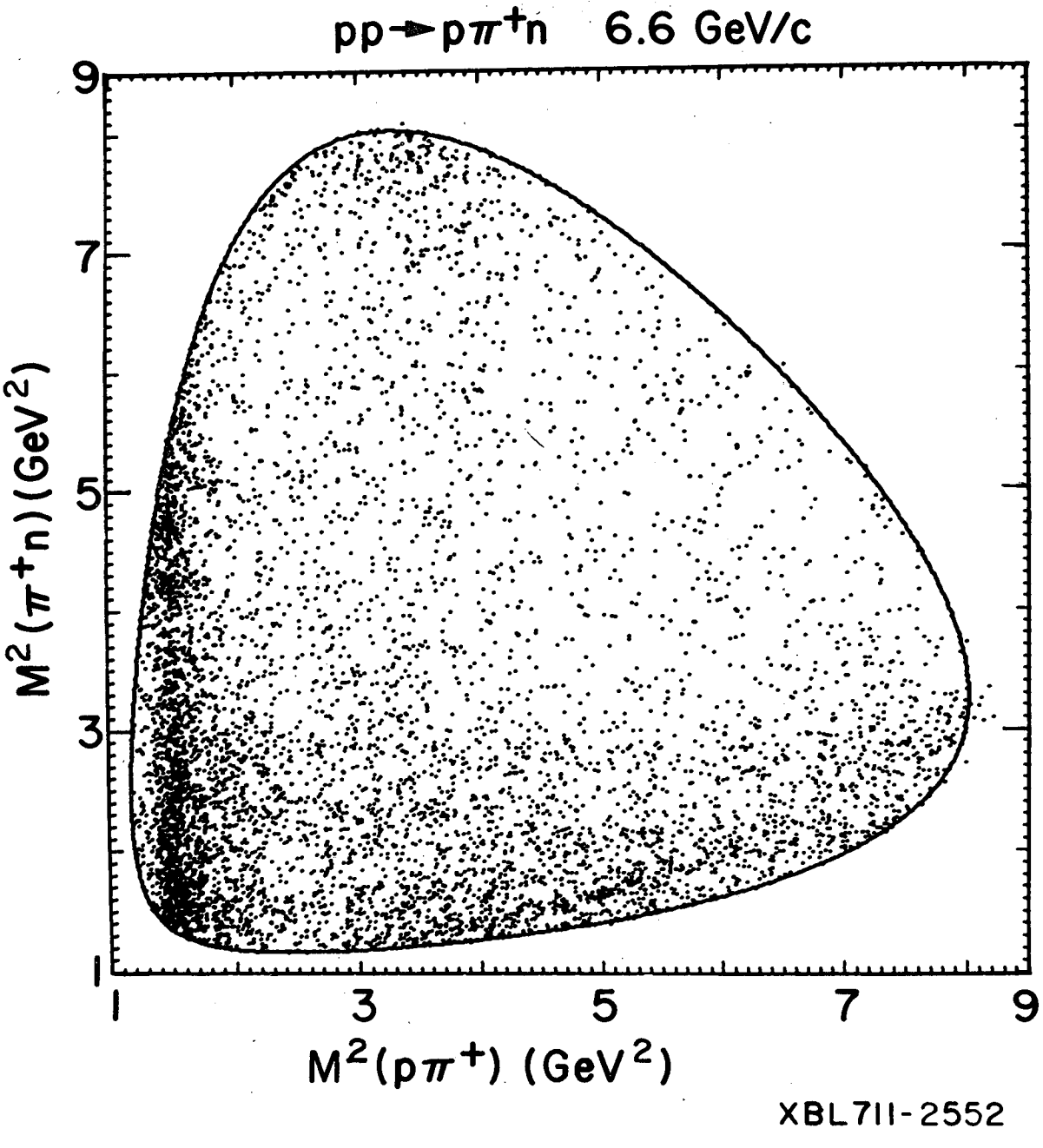

FIGURE 13

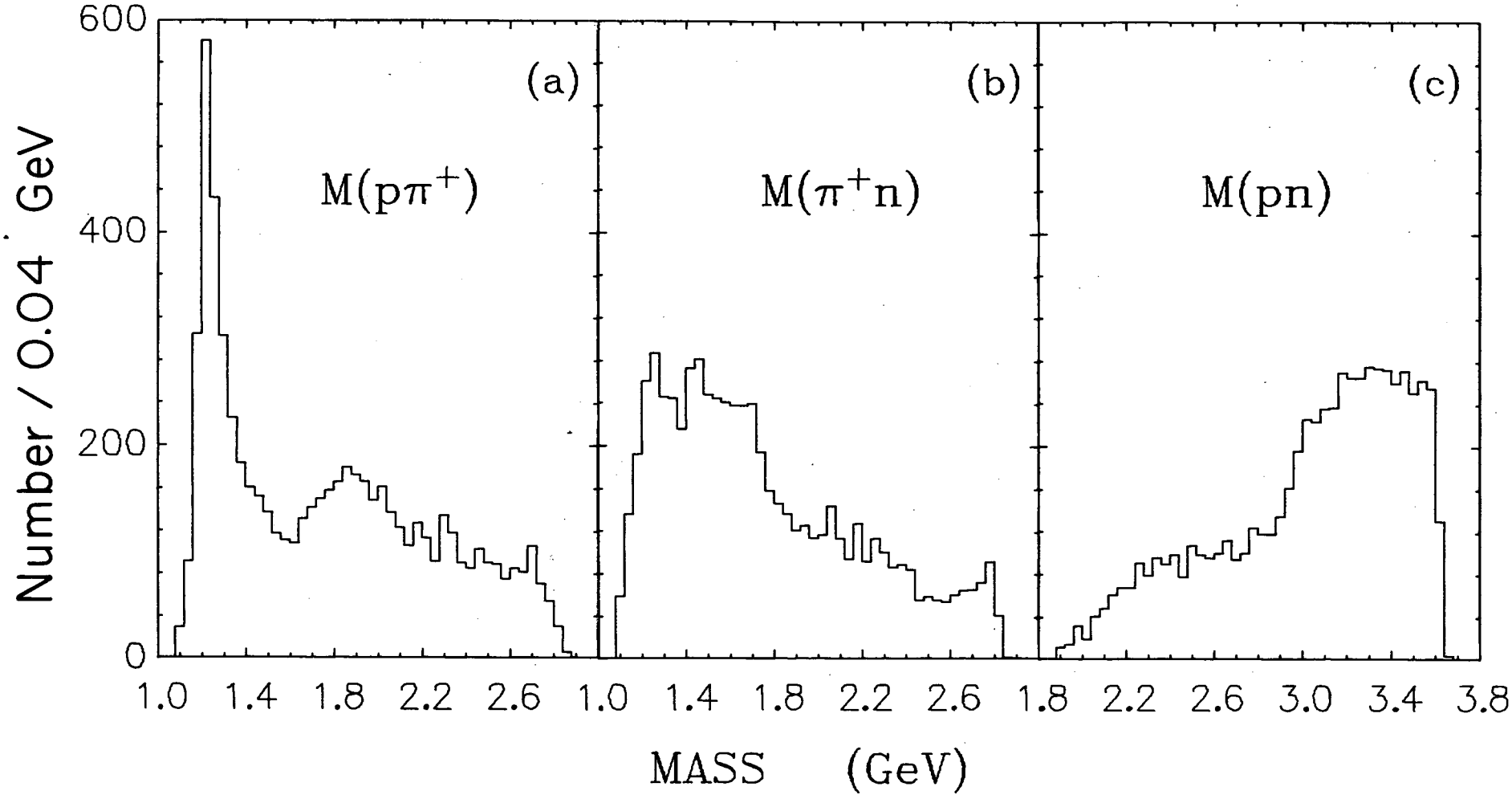

XBL711-2561

FIGURE 14

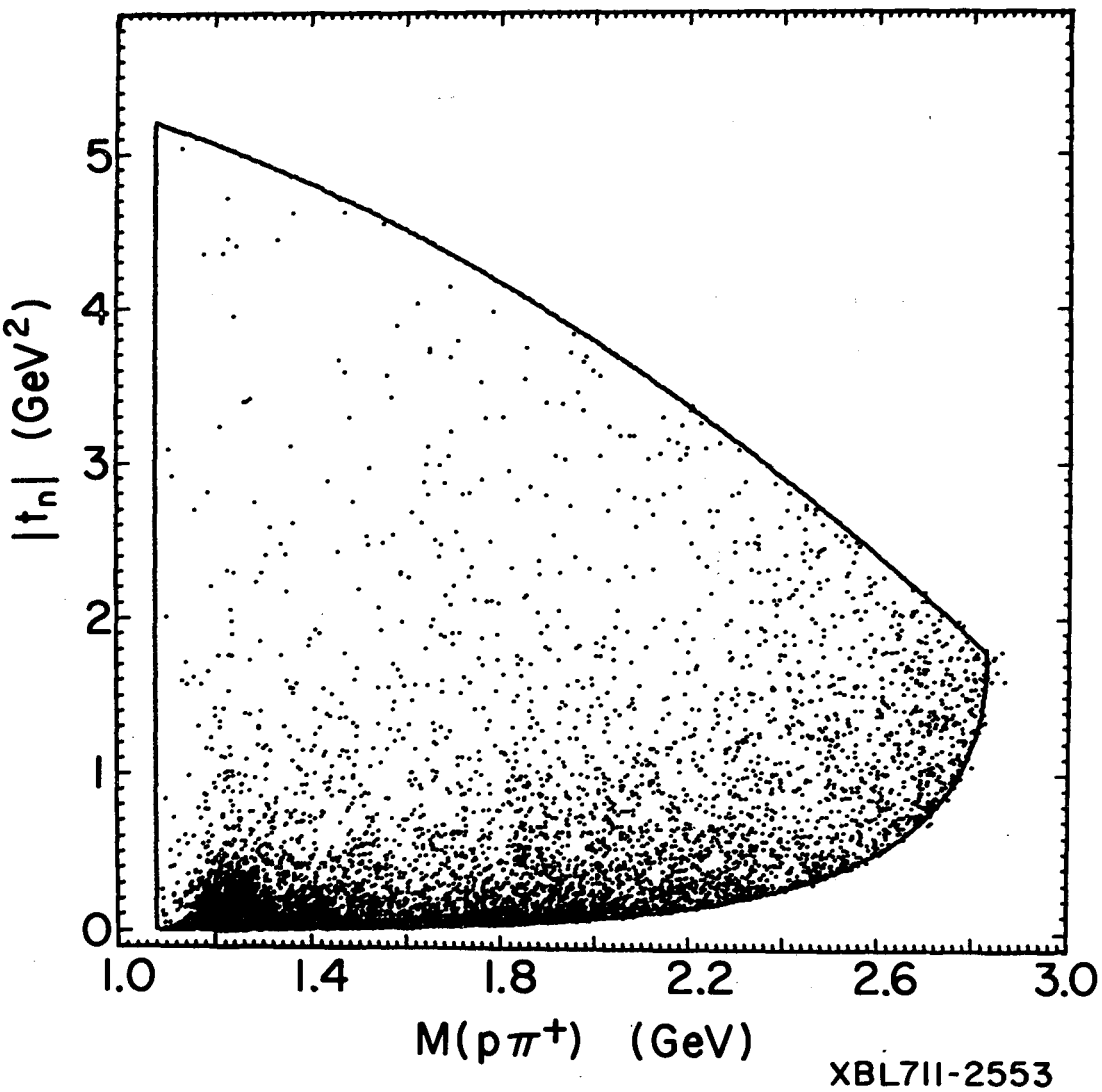

FIGURE 15

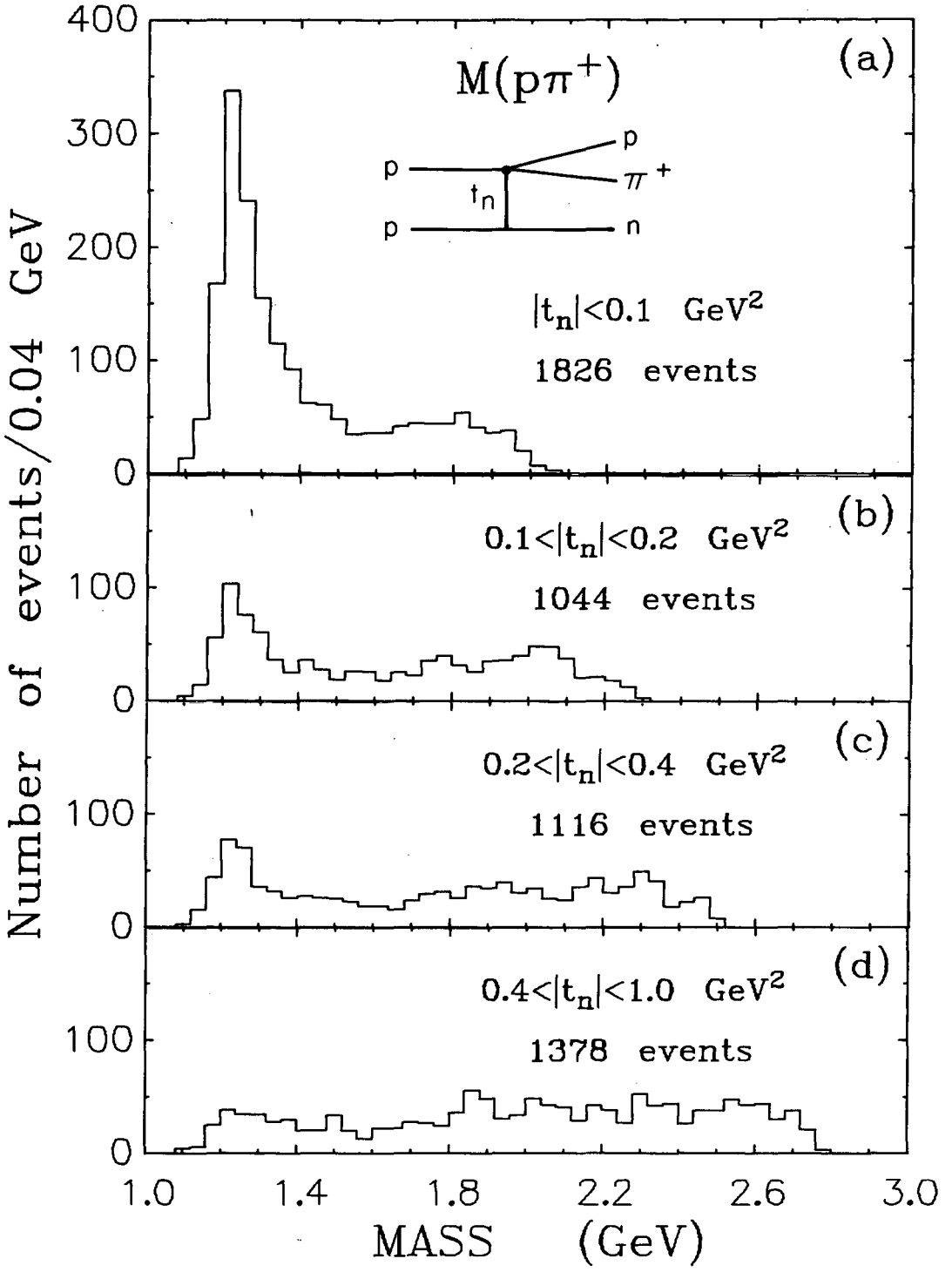
M(pπ+)
(a)
p
π +
p
tn
p
n
|tn|<0.1 GeV2
1826 events
(b)
0.1<|tn|<0.2 GeV2
1044 events
(c)
0.2<|tn|<0.4 GeV2
1116 events
(d)
0.4<|tn|<1.0 GeV2
1378 events
Number of events/0.04 GeV
400
300
200
100
0
1.0
1.4
1.8
2.2
2.6
3.0
MASS (GeV)
XBL711-2558

FIGURE 16

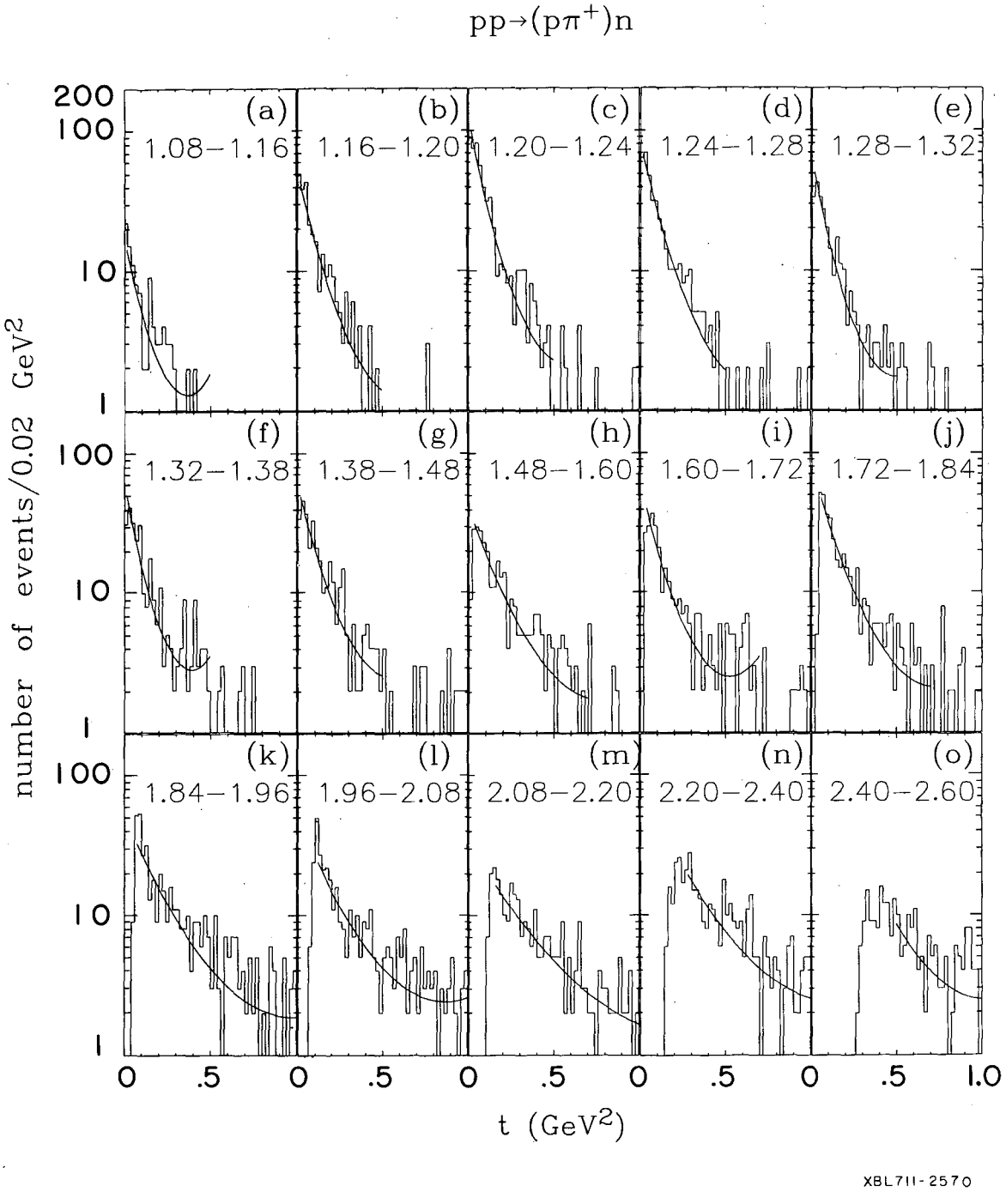
pp→(pπ+)n
(a) 1.08–1.16
(b) 1.16–1.20
(c) 1.20–1.24
(d) 1.24–1.28
(e) 1.28–1.32
(f) 1.32–1.38
(g) 1.38–1.48
(h) 1.48–1.60
(i) 1.60–1.72
(j) 1.72–1.84
(k) 1.84–1.96
(l) 1.96–2.08
(m) 2.08–2.20
(n) 2.20–2.40
(o) 2.40–2.60
number of events/0.02 GeV2
200
100
10
1
0
.5
1.0
t (GeV2)
XBL711-2570

FIGURE 17

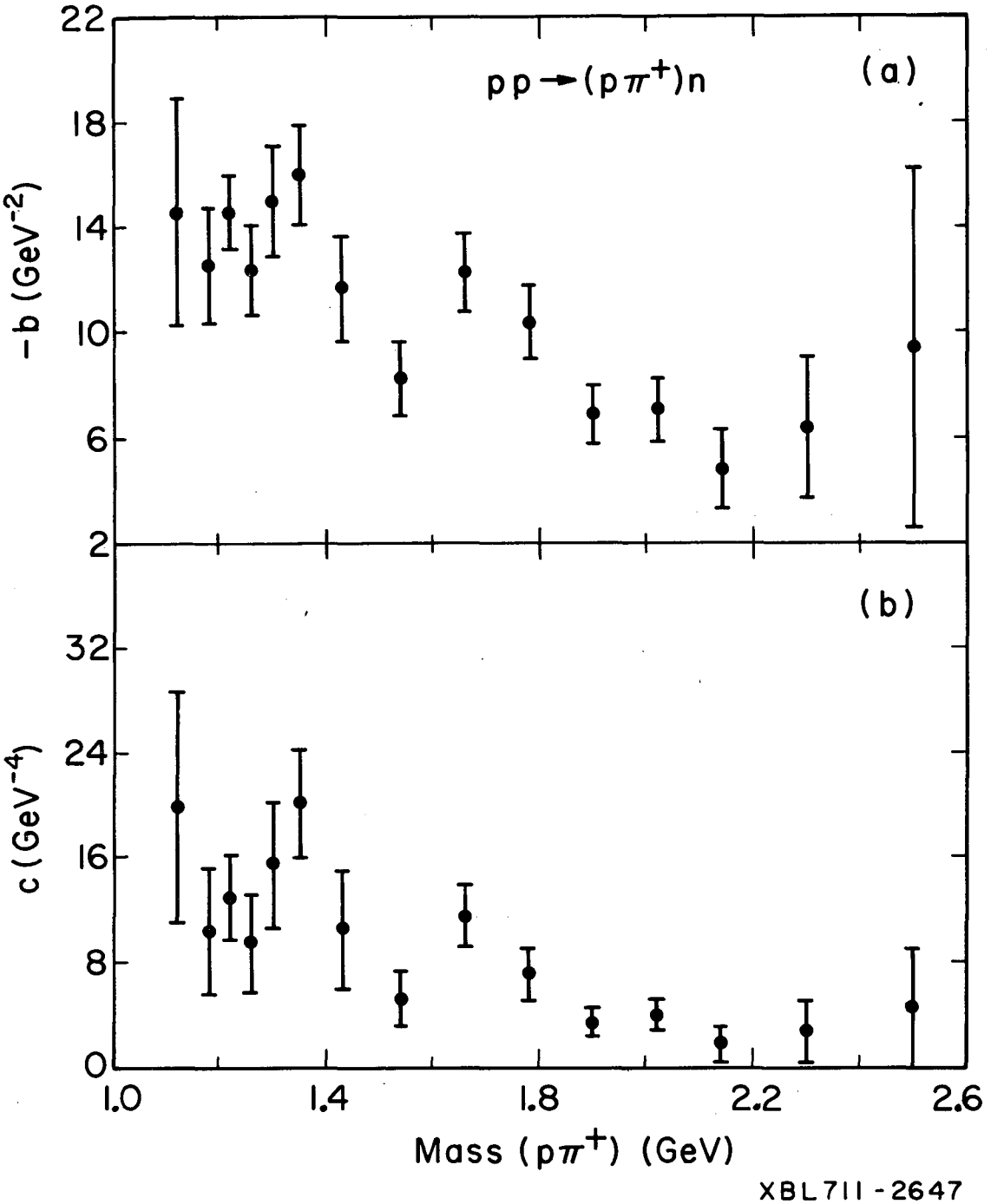
pp → (pπ+)n
(a)
(b)
-b (GeV-2)
c (GeV-4)
Mass (pπ+) (GeV)
22
18
14
10
6
2
32
24
16
8
0
1.0
1.4
1.8
2.2
2.6
XBL711-2647

FIGURE 18

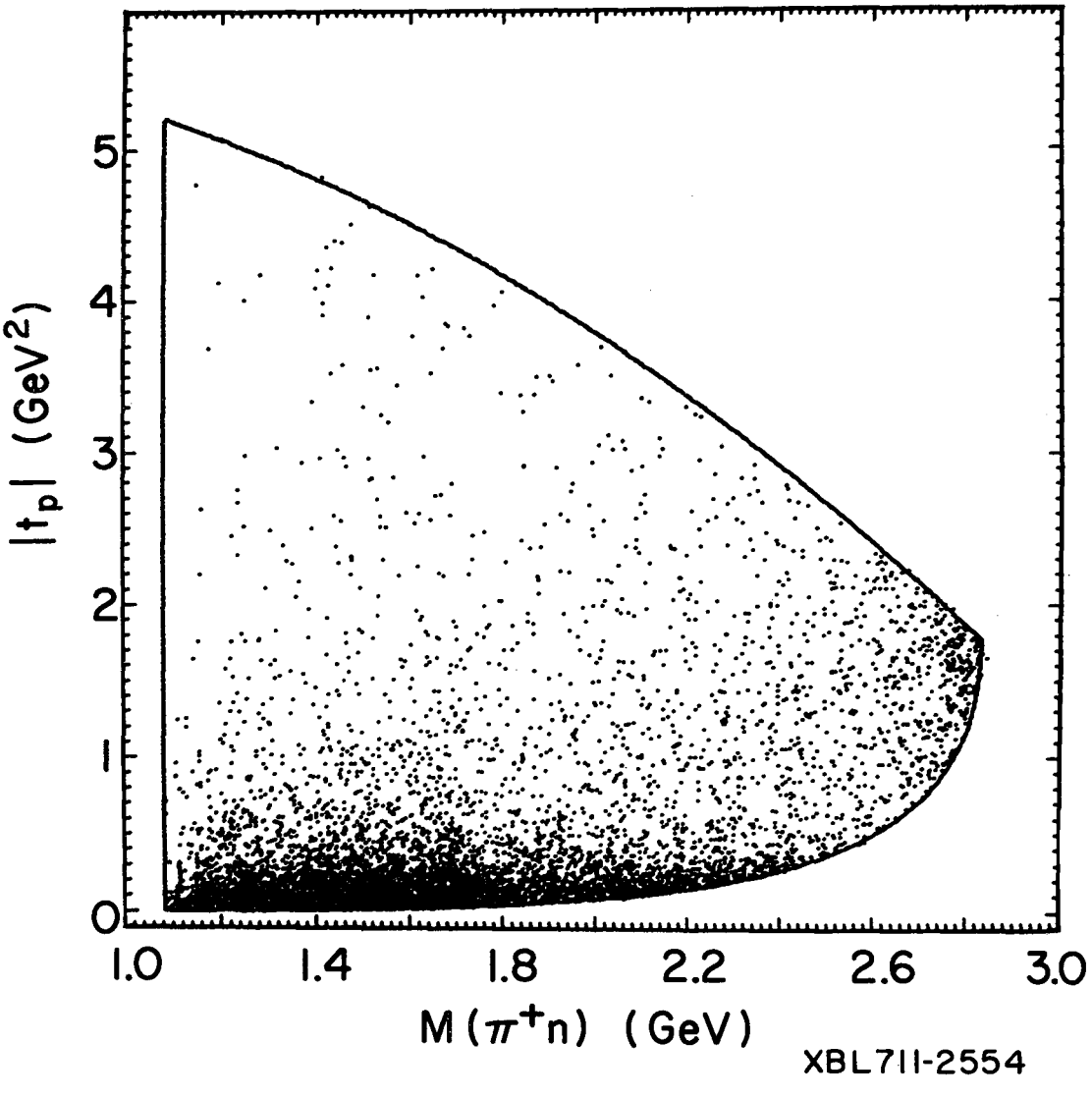

FIGURE 19

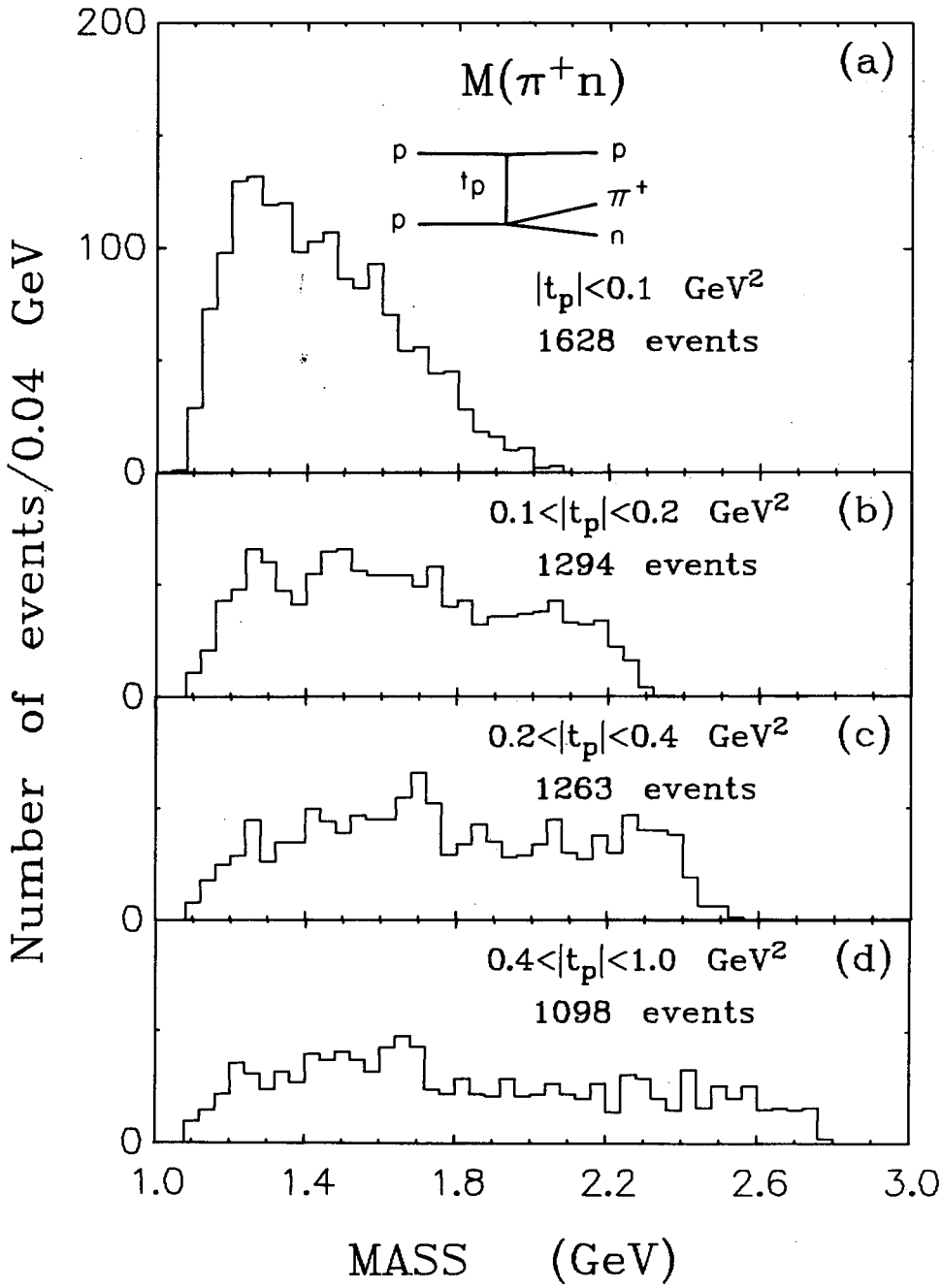

XBL711-2559

FIGURE 20

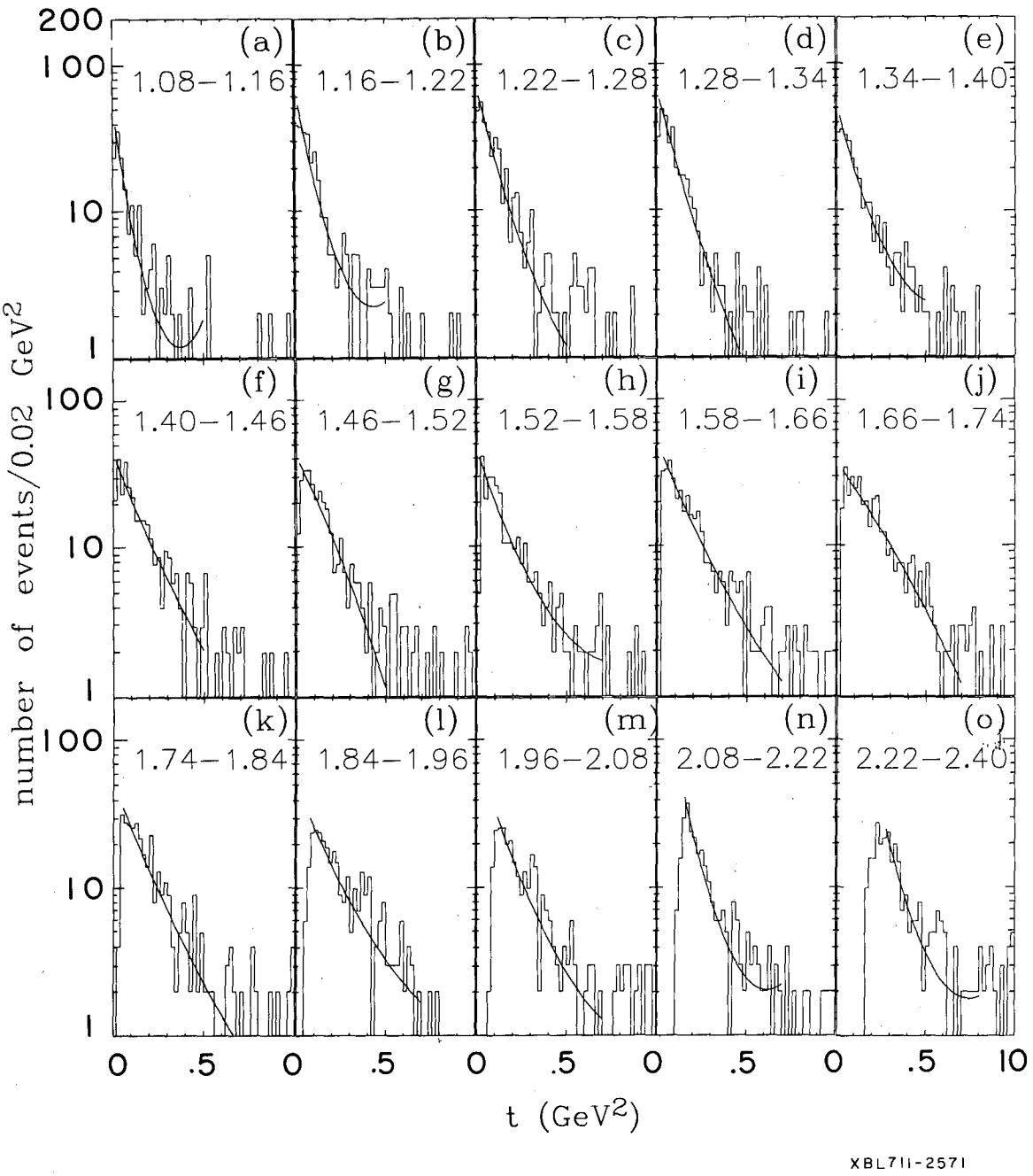
pp→p(π+n)
(a) 1.08–1.16
(b) 1.16–1.22
(c) 1.22–1.28
(d) 1.28–1.34
(e) 1.34–1.40
(f) 1.40–1.46
(g) 1.46–1.52
(h) 1.52–1.58
(i) 1.58–1.66
(j) 1.66–1.74
(k) 1.74–1.84
(l) 1.84–1.96
(m) 1.96–2.08
(n) 2.08–2.22
(o) 2.22–2.40
number of events/0.02 GeV2
200
100
10
1
0
.5
10
t (GeV2)
XBL711-2571

FIGURE 21

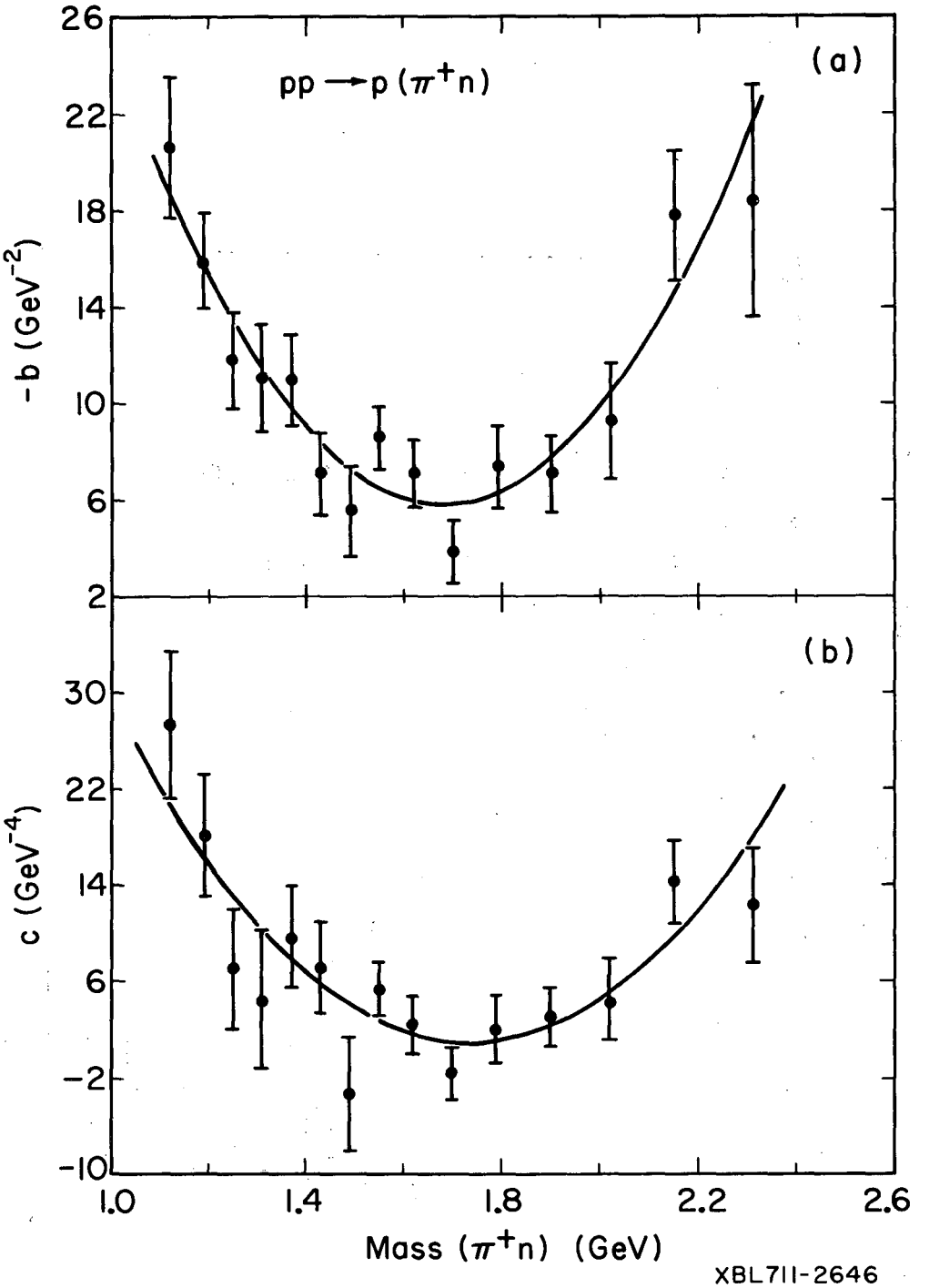
pp → p (π+n)
(a)
-b (GeV-2)
26
22
18
14
10
6
2
(b)
c (GeV-4)
30
22
14
6
-2
-10
1.0
1.4
1.8
2.2
2.6
Mass (π+n) (GeV)
XBL711-2646

FIGURE 22

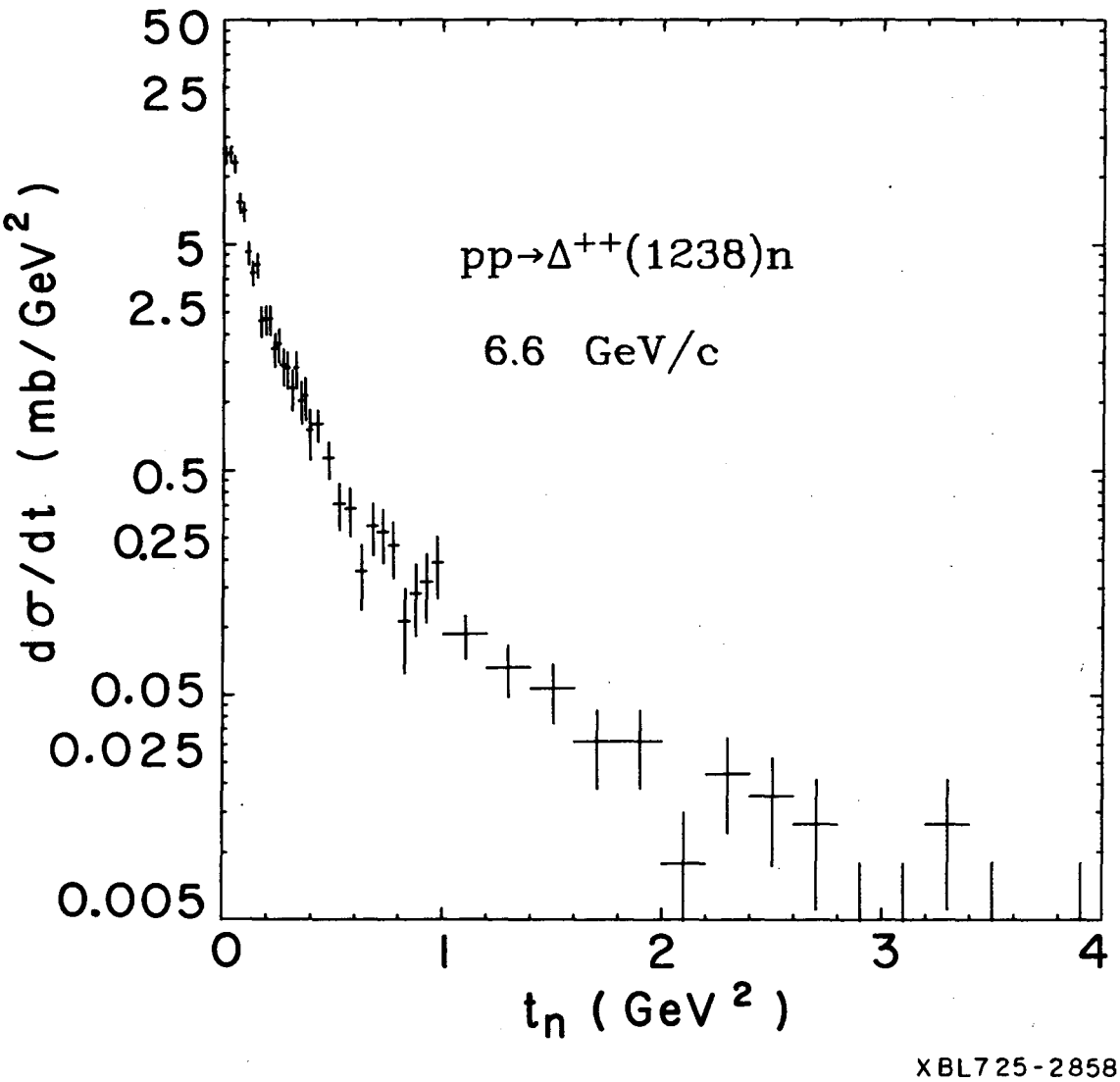
50
25
5
2.5
0.5
0.25
0.05
0.025
0.005
dσ/dt (mb/GeV²)
pp→Δ⁺⁺(1238)n
6.6 GeV/c
0
1
2
3
4
tn (GeV²)
XBL725-2858

FIGURE 23

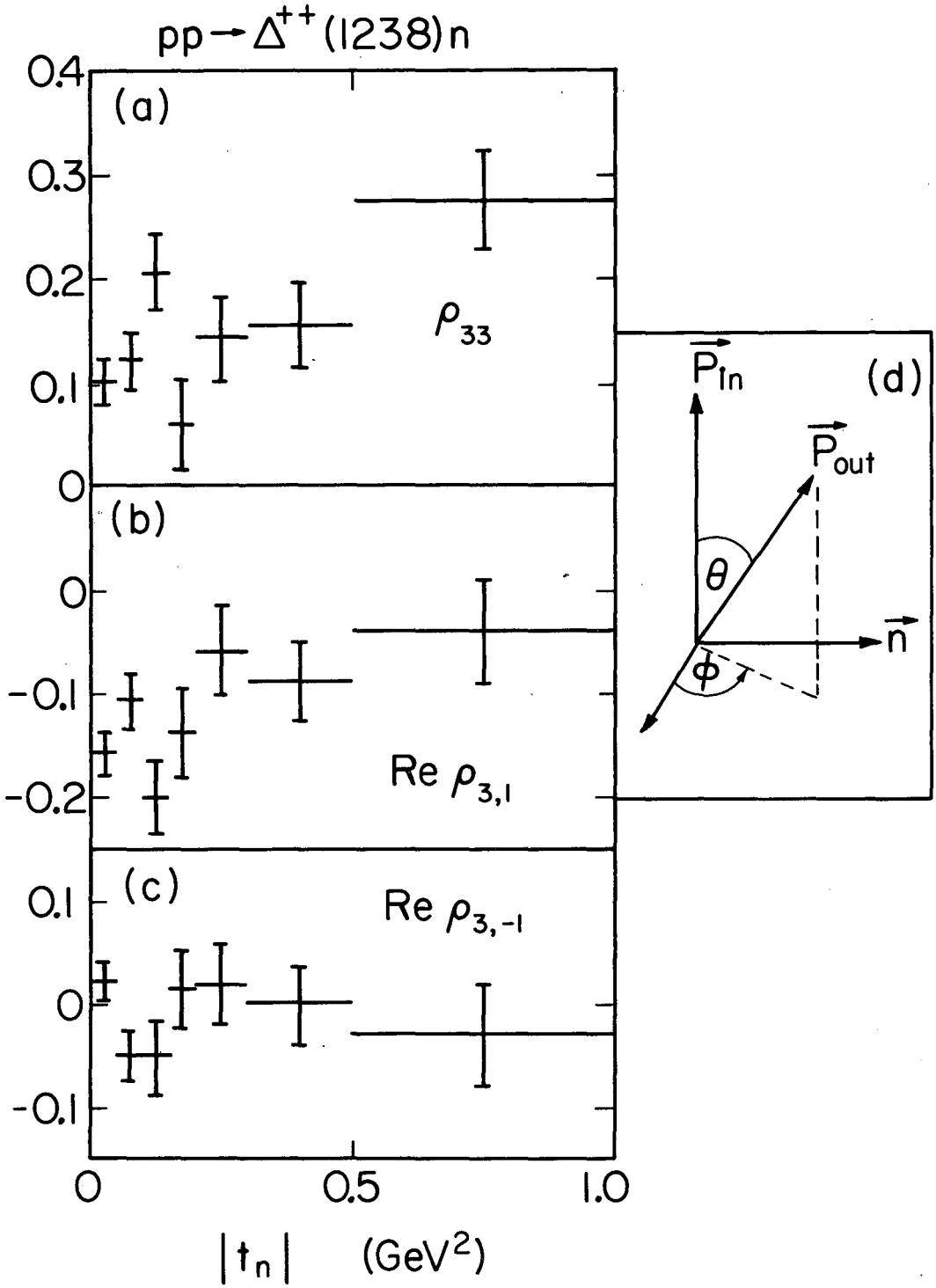

XBL 719-4435

FIGURE 24

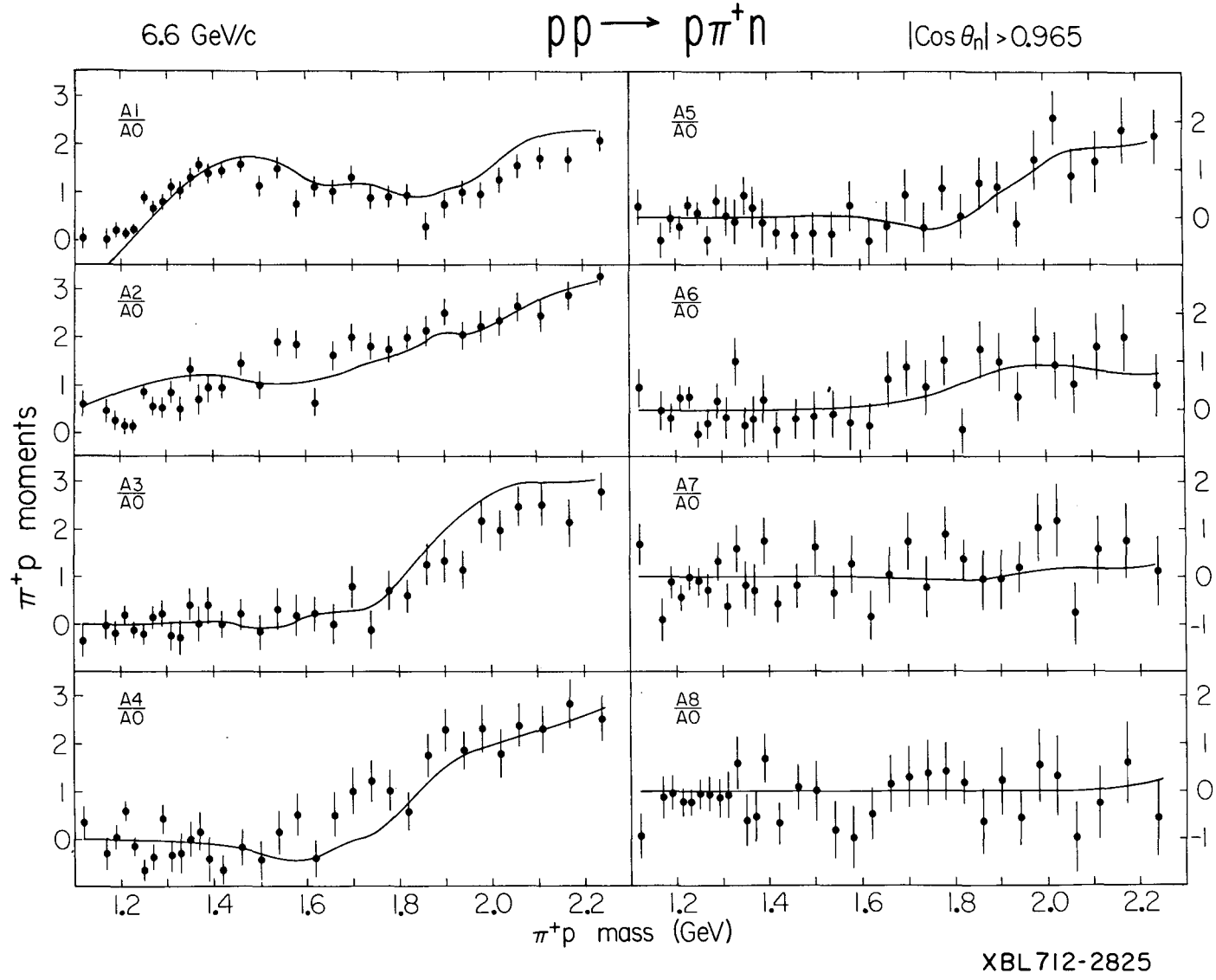
6.6 GeV/c
pp → pπ⁺n
|Cos θn| > 0.965
A1/A0
A2/A0
A3/A0
A4/A0
A5/A0
A6/A0
A7/A0
A8/A0
π⁺p moments
π⁺p mass (GeV)
XBL712-2825

FIGURE 25

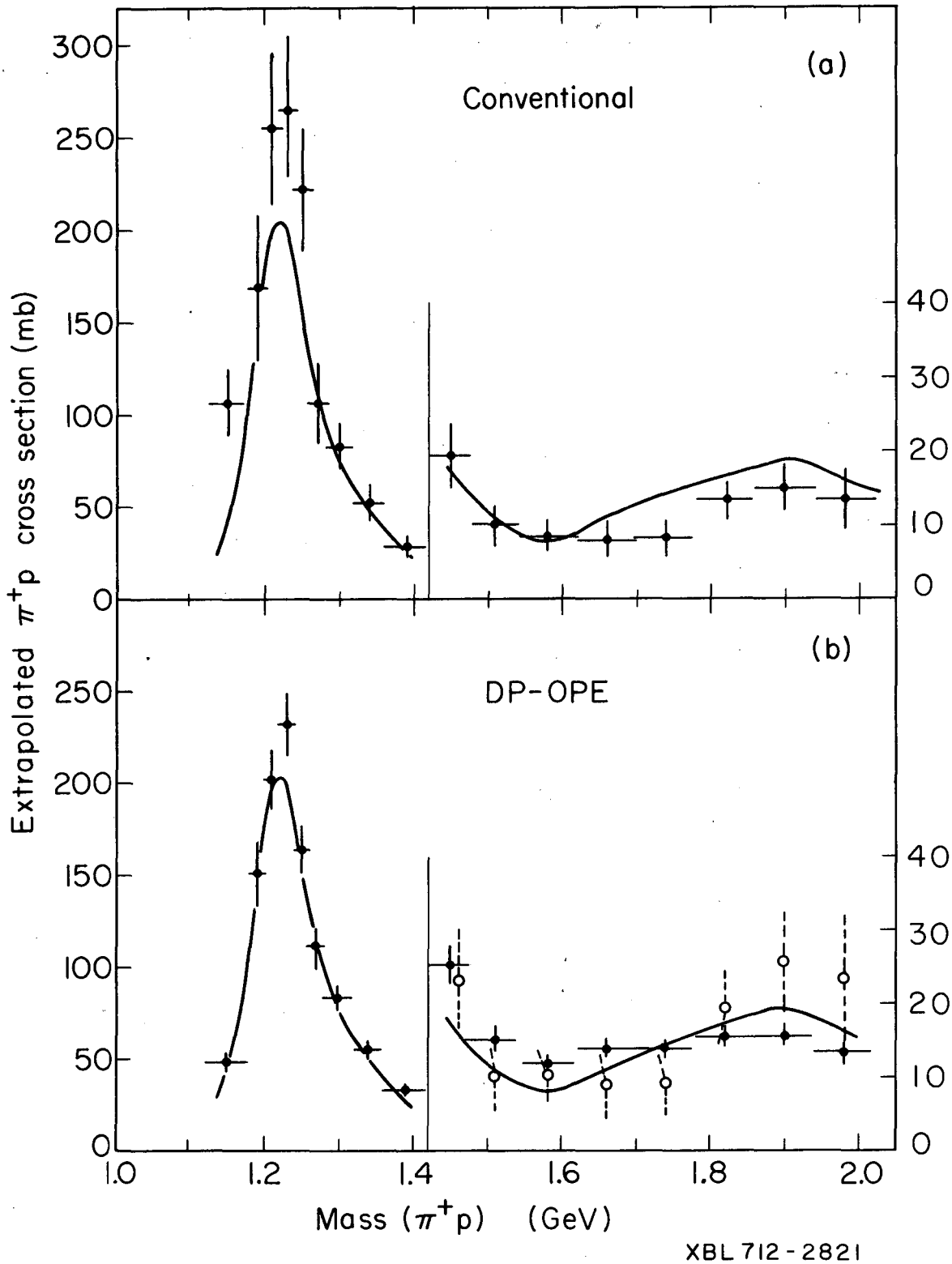
(a)
Conventional
(b)
DP-OPE
Extrapolated π^+p cross section (mb)
Mass (π^+p) (GeV)
300
250
200
150
100
50
0
40
30
20
10
0
1.0
1.2
1.4
1.6
1.8
2.0
XBL 712-2821

FIGURE 26

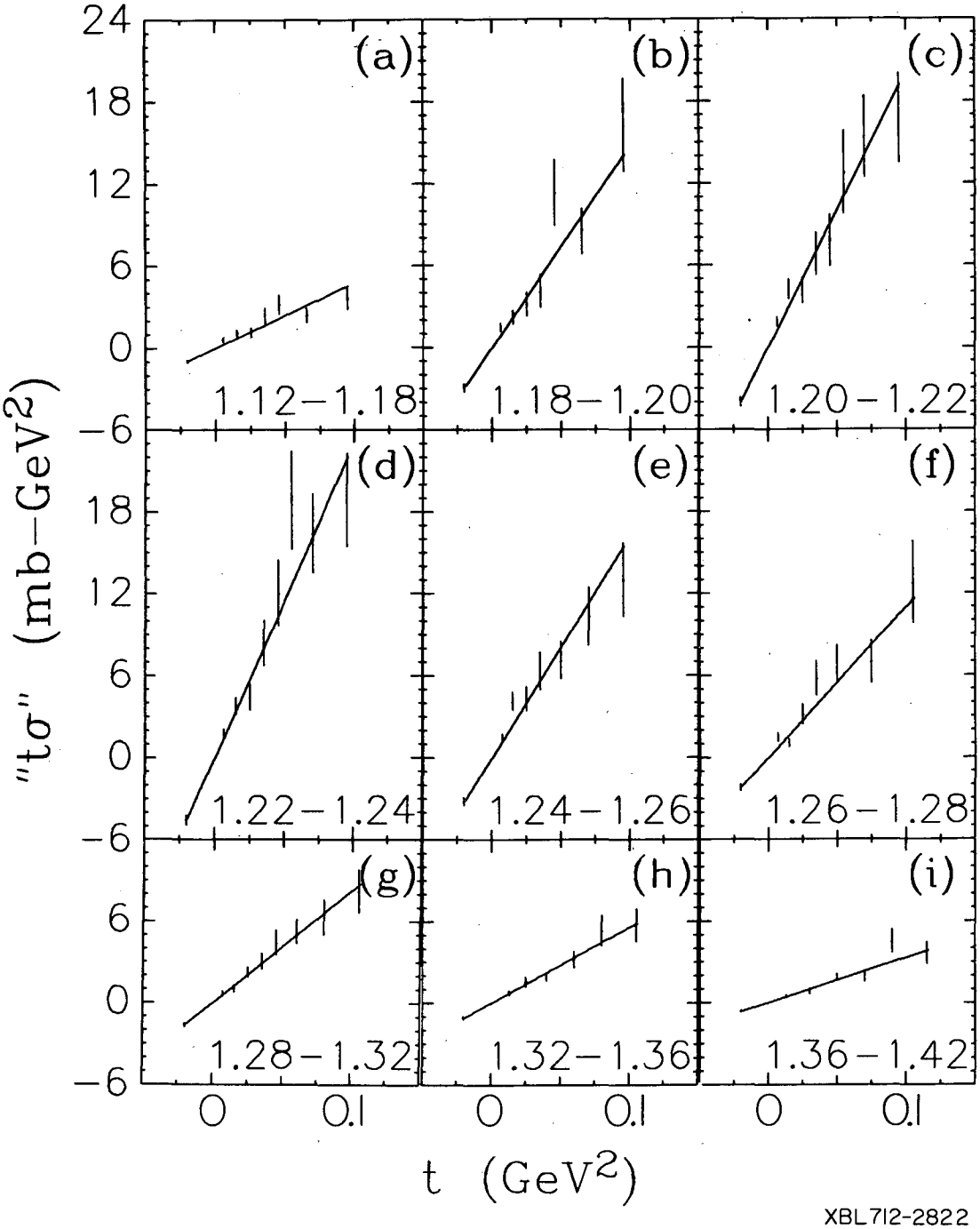
(a)
(b)
(c)
(d)
(e)
(f)
(g)
(h)
(i)
1.12−1.18
1.18−1.20
1.20−1.22
1.22−1.24
1.24−1.26
1.26−1.28
1.28−1.32
1.32−1.36
1.36−1.42
24
18
12
6
0
−6
0
0.1
"tσ" (mb−GeV²)
t (GeV²)
XBL712-2822

FIGURE 27

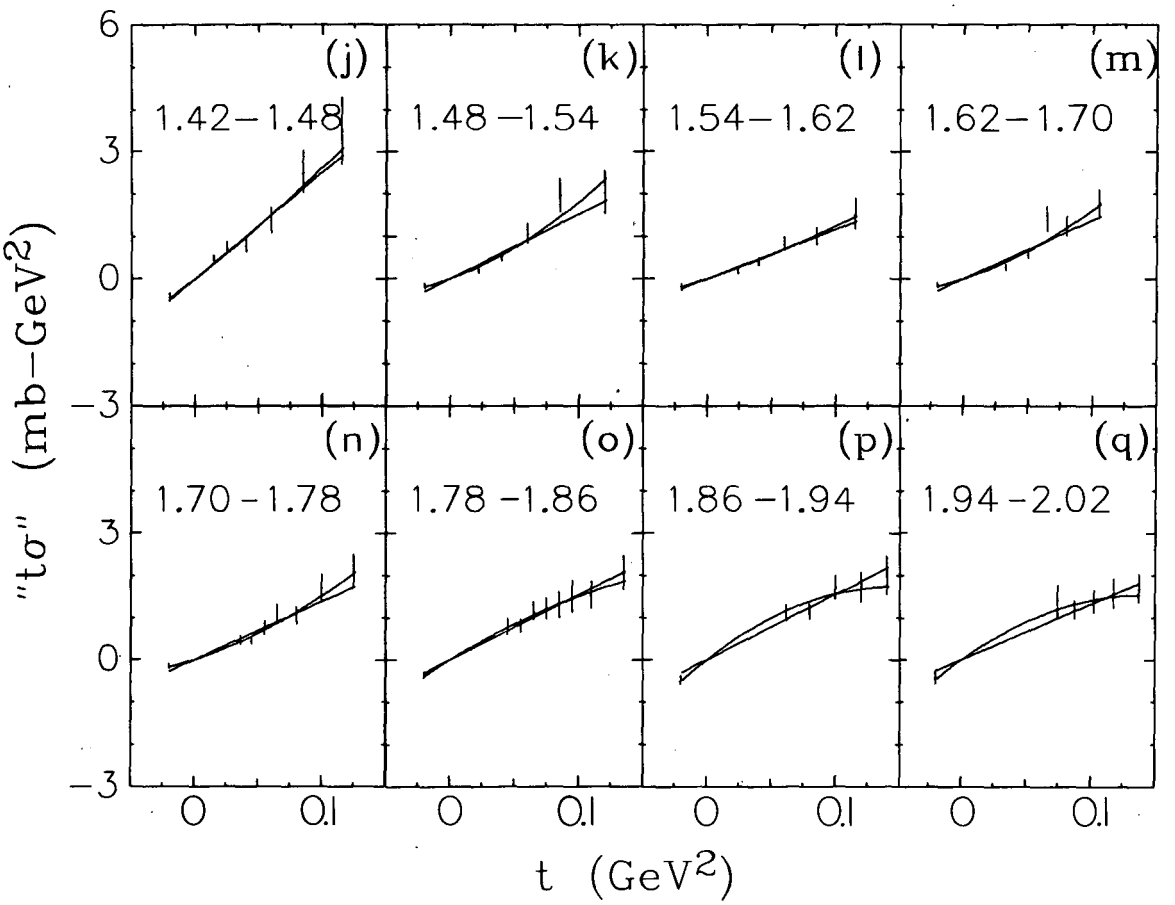
(j)
1.42–1.48
(k)
1.48–1.54
(l)
1.54–1.62
(m)
1.62–1.70
(n)
1.70–1.78
(o)
1.78–1.86
(p)
1.86–1.94
(q)
1.94–2.02
6
3
0
−3
0
0.1
"tσ" (mb–GeV²)
t (GeV²)
XBL712-2823

FIGURE 27

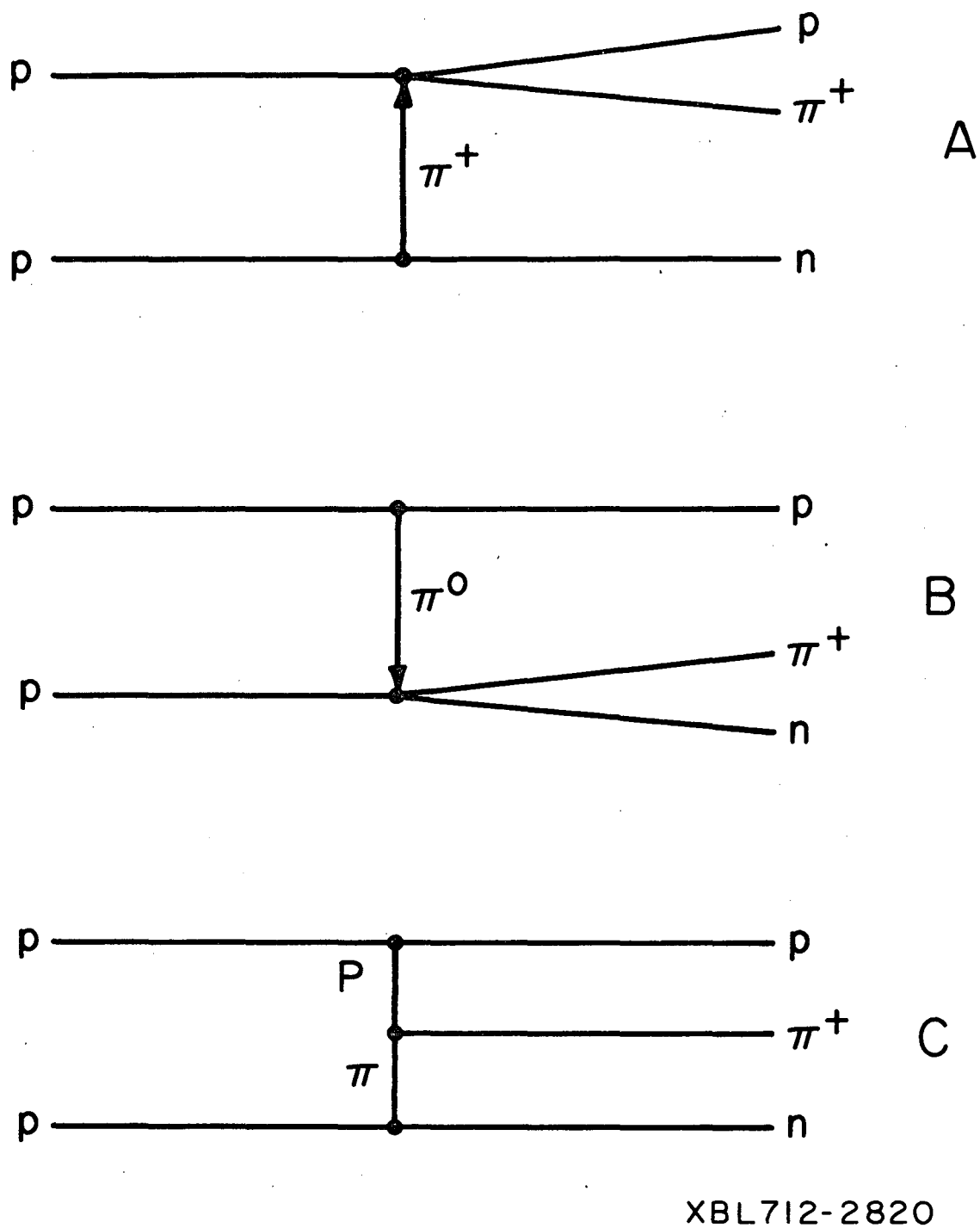

FIGURE 28

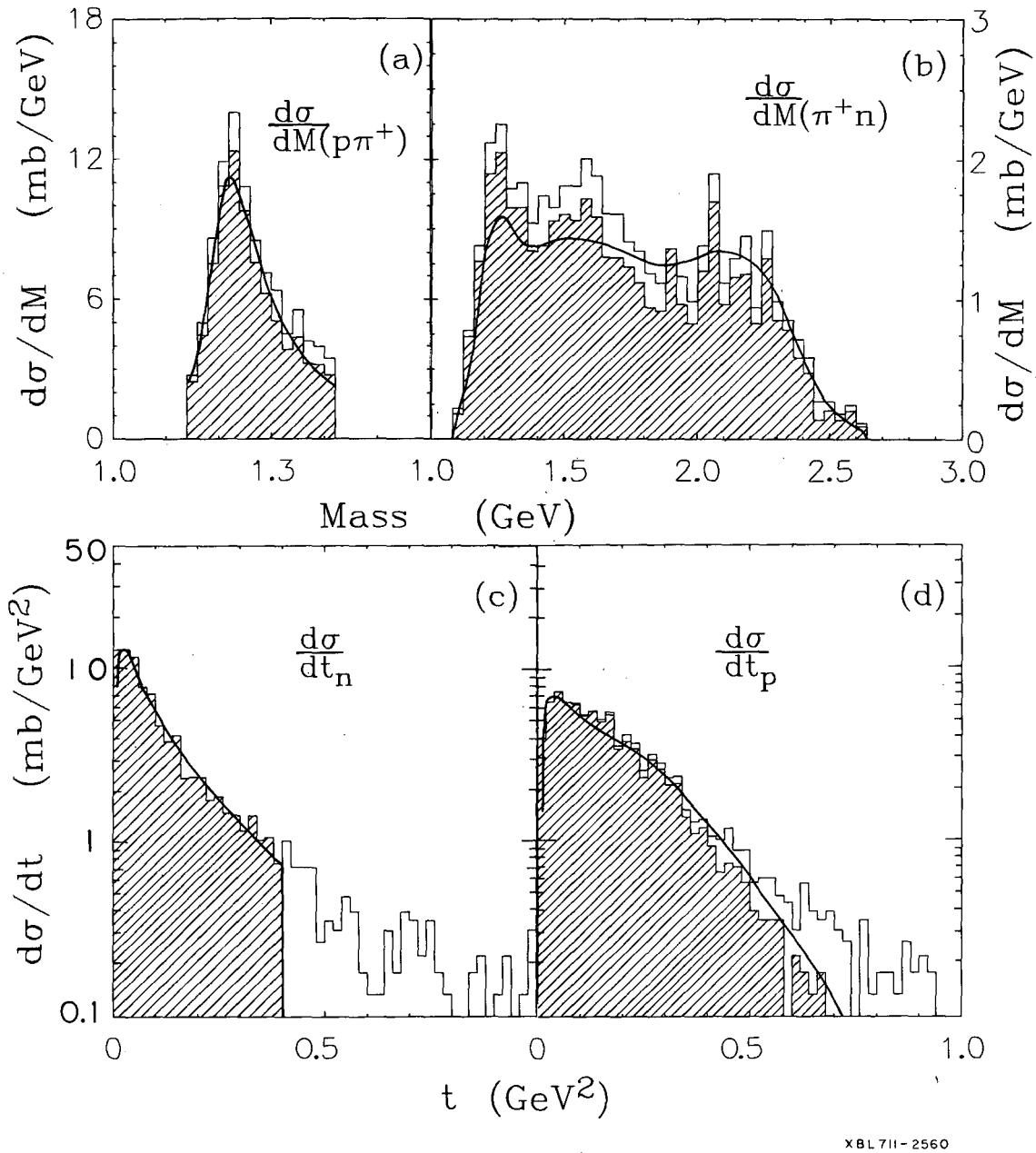
(a)
(b)
(c)
(d)
$\frac{d\sigma}{dM(p\pi^+)}$
$\frac{d\sigma}{dM(\pi^+n)}$
$\frac{d\sigma}{dt_n}$
$\frac{d\sigma}{dt_p}$
dσ/dM (mb/GeV)
dσ/dt (mb/GeV²)
Mass (GeV)
t (GeV²)
XBL711-2560

FIGURE 29

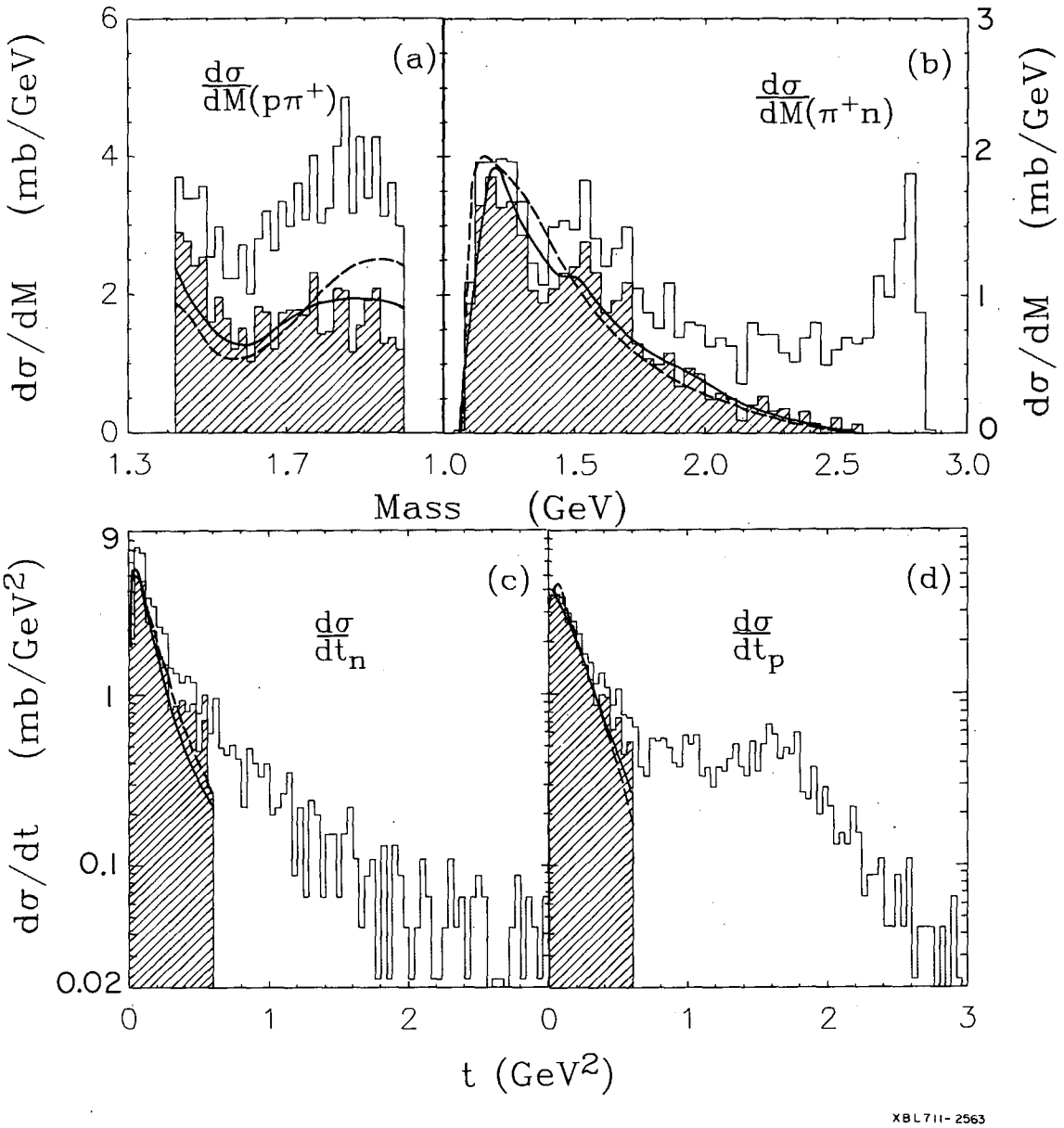
(a)
$\frac{d\sigma}{dM}(p\pi^+)$
(b)
$\frac{d\sigma}{dM}(\pi^+ n)$
$d\sigma/dM$ (mb/GeV)
Mass (GeV)
(c)
$\frac{d\sigma}{dt_n}$
(d)
$\frac{d\sigma}{dt_p}$
$d\sigma/dt$ (mb/GeV^2)
t (GeV^2)
XBL711-2563

FIGURE 30

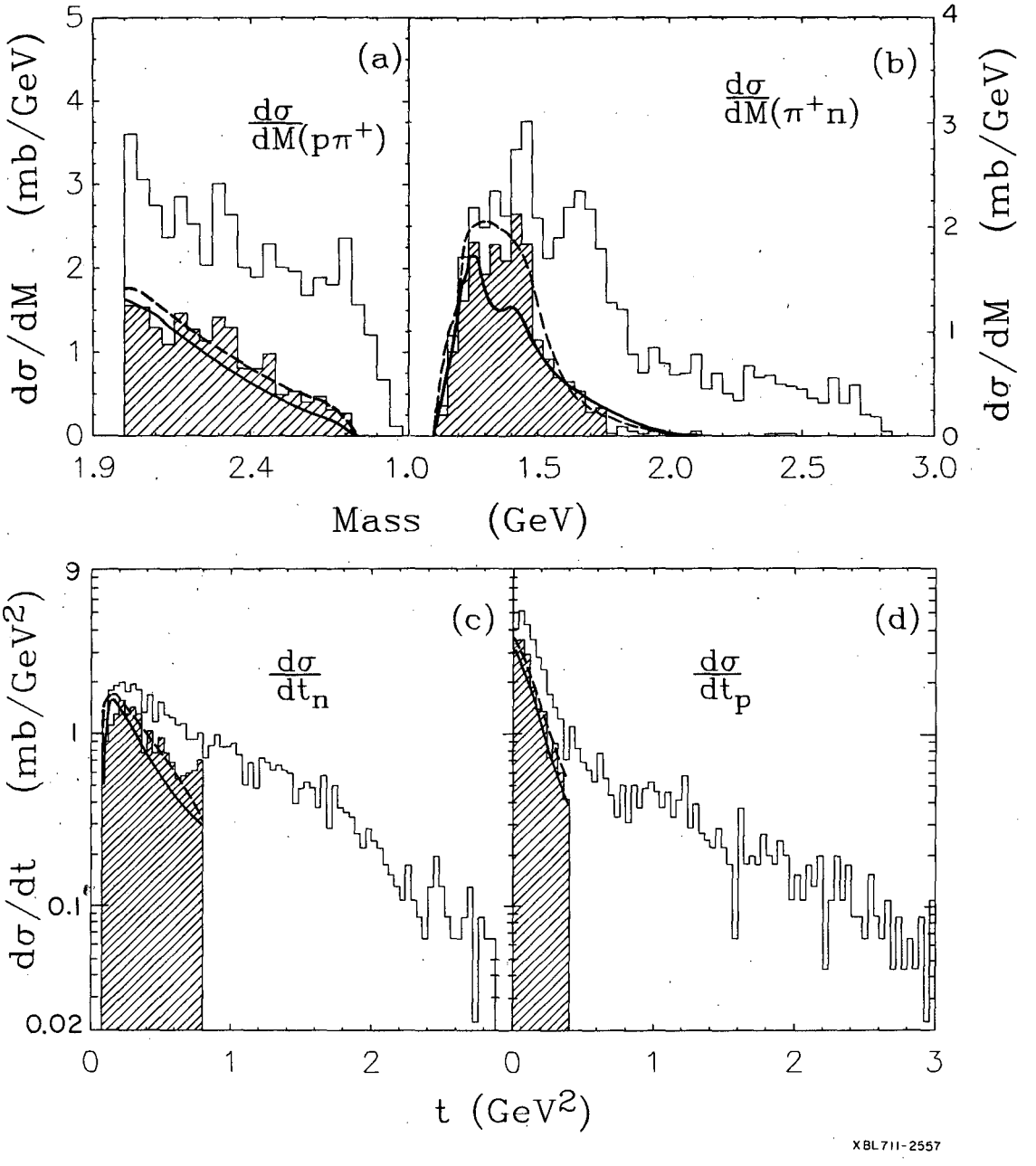
(a)
$\frac{d\sigma}{dM}(p\pi^+)$
(b)
$\frac{d\sigma}{dM}(\pi^+ n)$
$d\sigma/dM$ (mb/GeV)
Mass (GeV)
(c)
$\frac{d\sigma}{dt_n}$
(d)
$\frac{d\sigma}{dt_p}$
$d\sigma/dt$ (mb/GeV^2)
t (GeV^2)
XBL711-2557

FIGURE 31

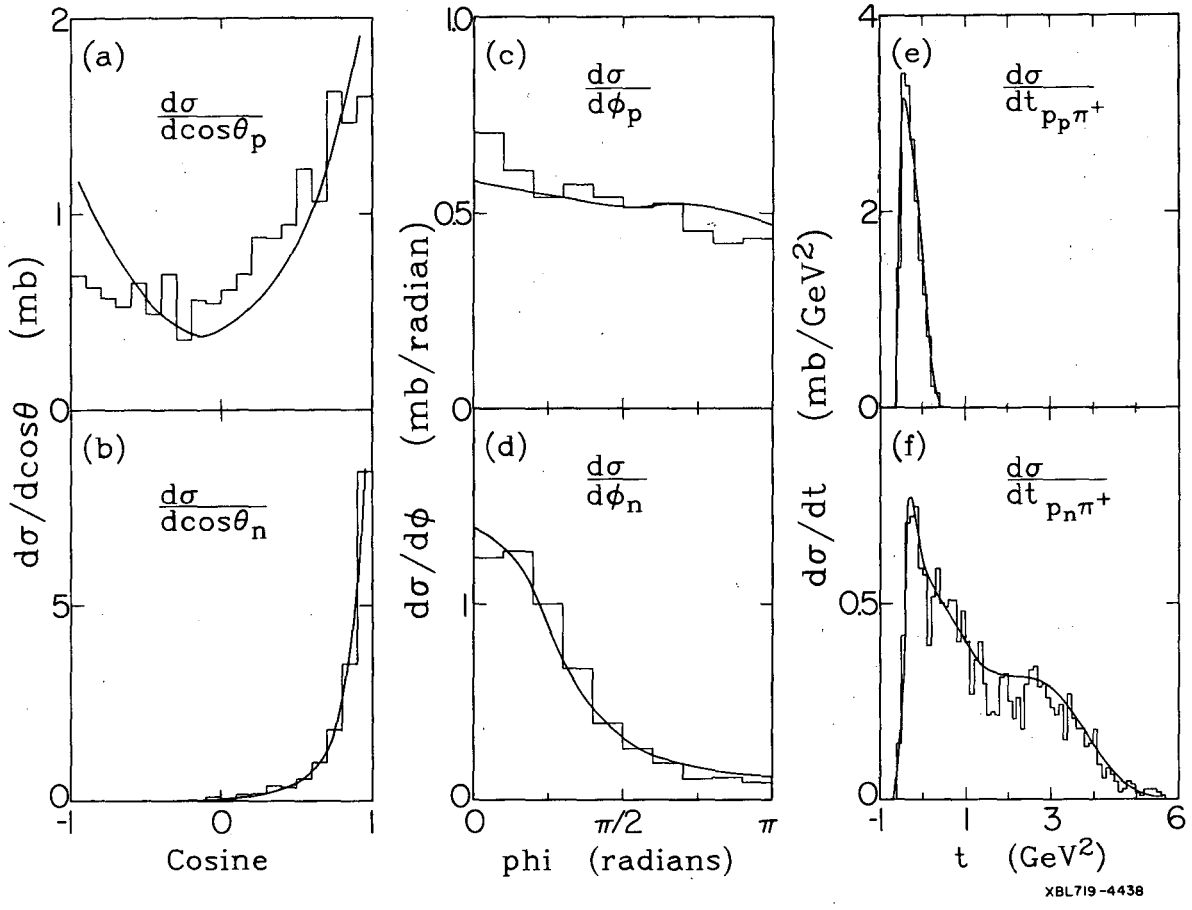
(a)
$\frac{d\sigma}{d\cos\theta_p}$
(b)
$\frac{d\sigma}{d\cos\theta_n}$
$d\sigma/d\cos\theta$ (mb)
Cosine
(c)
$\frac{d\sigma}{d\phi_p}$
(d)
$\frac{d\sigma}{d\phi_n}$
$d\sigma/d\phi$ (mb/radian)
phi (radians)
(e)
$\frac{d\sigma}{dt_{p_p\pi^+}}$
(f)
$\frac{d\sigma}{dt_{p_n\pi^+}}$
$d\sigma/dt$ (mb/GeV^2)
t (GeV^2)
XBL719-4438

FIGURE 32

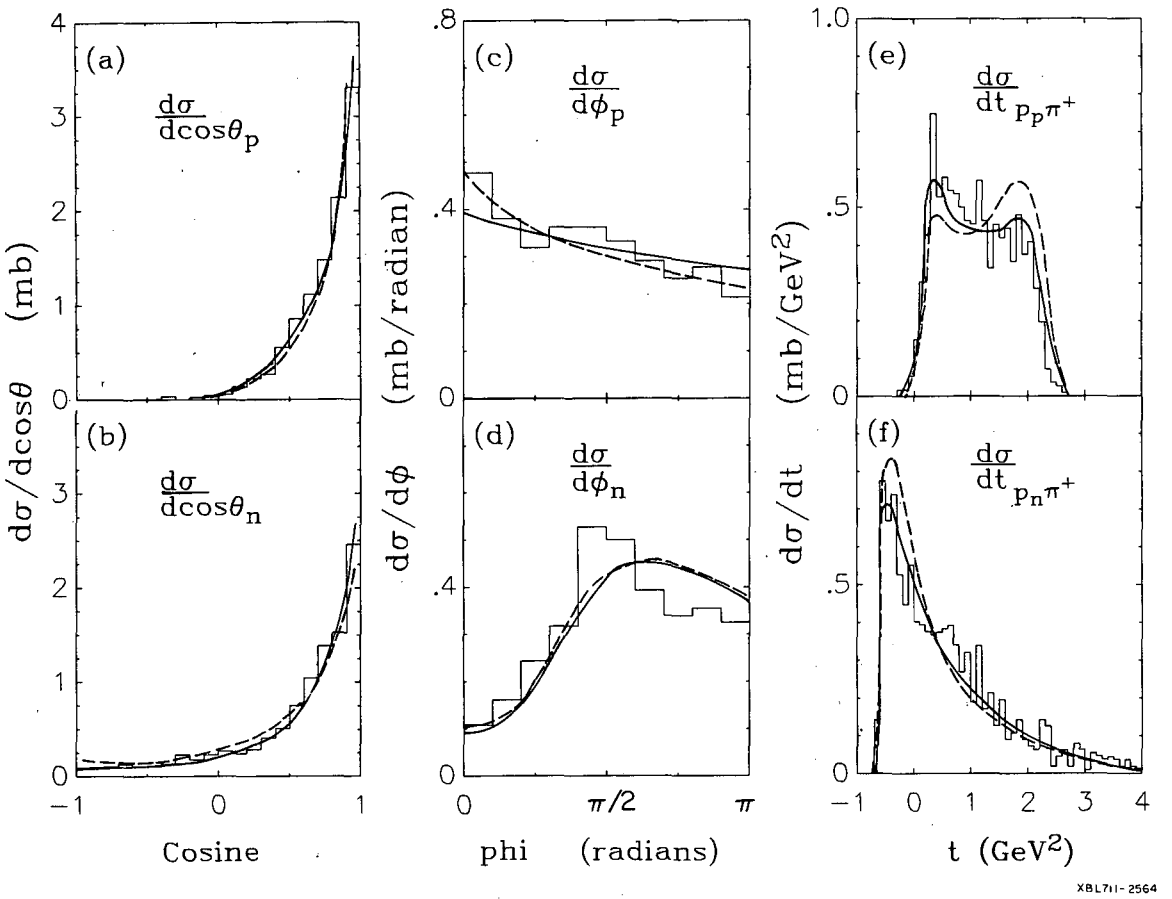
(a)
$\frac{d\sigma}{d\cos\theta_p}$
(b)
$\frac{d\sigma}{d\cos\theta_n}$
$d\sigma/d\cos\theta$ (mb)
Cosine
(c)
$\frac{d\sigma}{d\phi_p}$
(d)
$\frac{d\sigma}{d\phi_n}$
$d\sigma/d\phi$ (mb/radian)
phi (radians)
(e)
$\frac{d\sigma}{dt}_{p_p\pi^+}$
(f)
$\frac{d\sigma}{dt}_{p_n\pi^+}$
$d\sigma/dt$ (mb/GeV^2)
t (GeV^2)
XBL711-2564

FIGURE 33

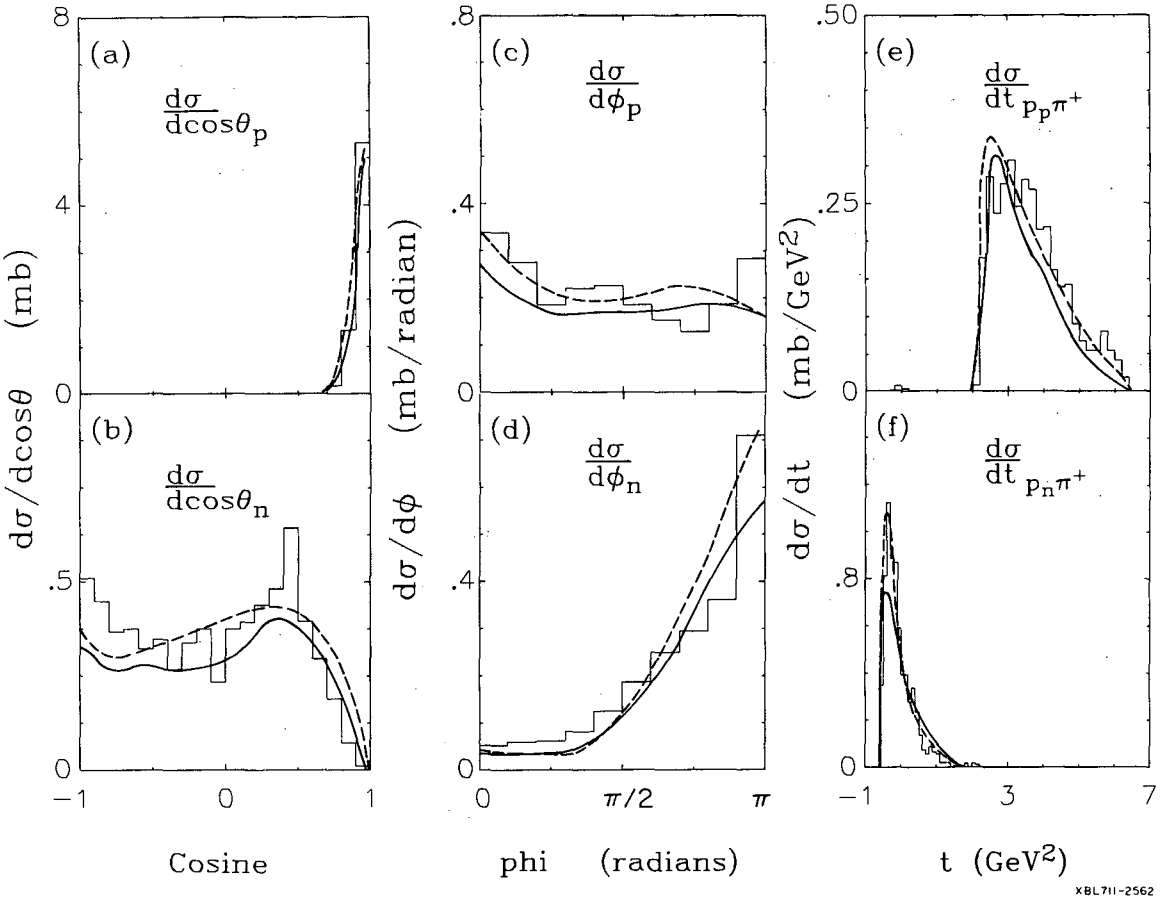
(a)
$\frac{d\sigma}{d\cos\theta_p}$
(b)
$\frac{d\sigma}{d\cos\theta_n}$
$d\sigma/d\cos\theta$ (mb)
Cosine
(c)
$\frac{d\sigma}{d\phi_p}$
(d)
$\frac{d\sigma}{d\phi_n}$
$d\sigma/d\phi$ (mb/radian)
phi (radians)
(e)
$\frac{d\sigma}{dt}_{p_p\pi^+}$
(f)
$\frac{d\sigma}{dt}_{p_n\pi^+}$
$d\sigma/dt$ (mb/GeV^2)
t (GeV^2)
XBL711-2562

FIGURE 34

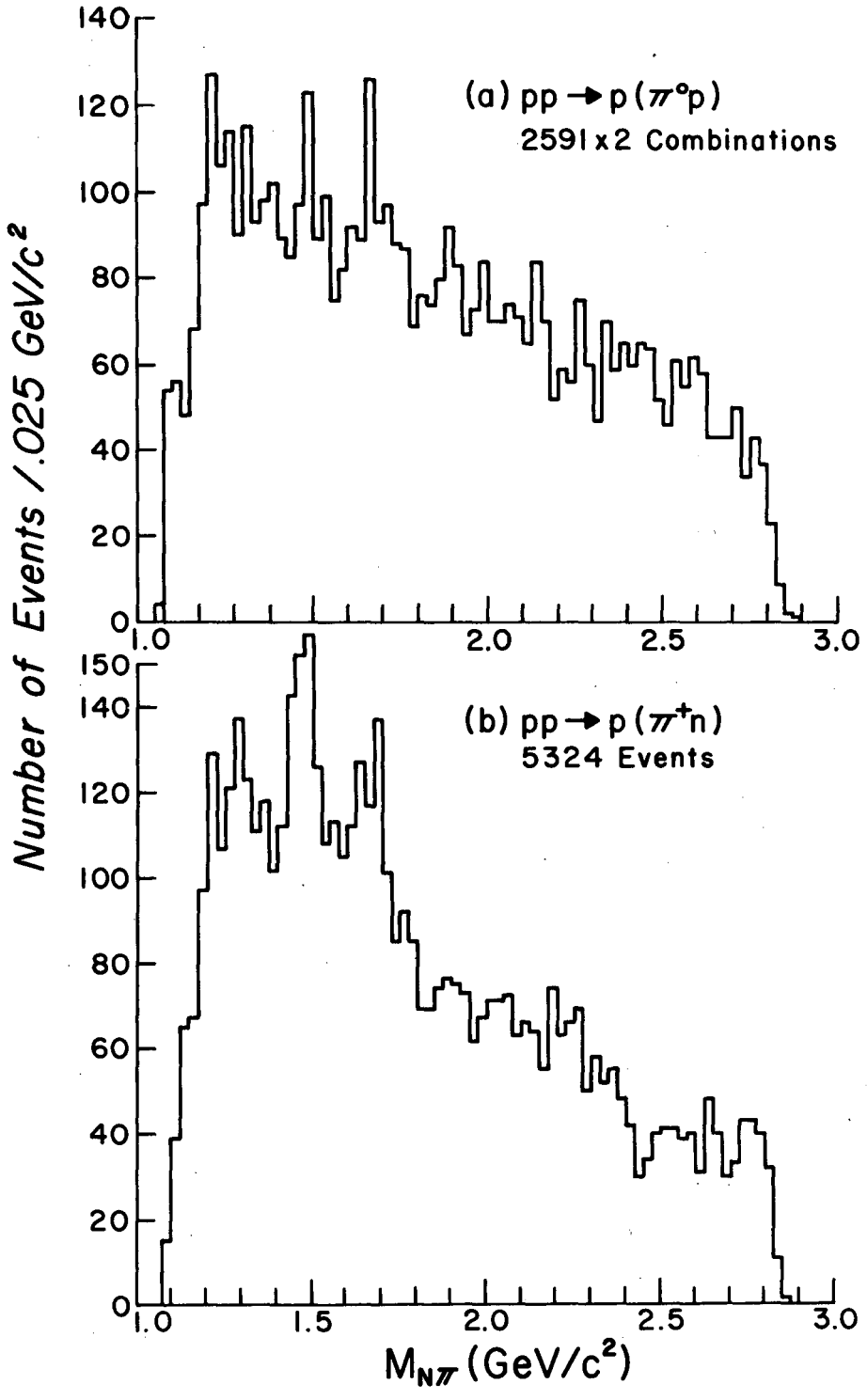

XBL 725-844

FIGURE 35

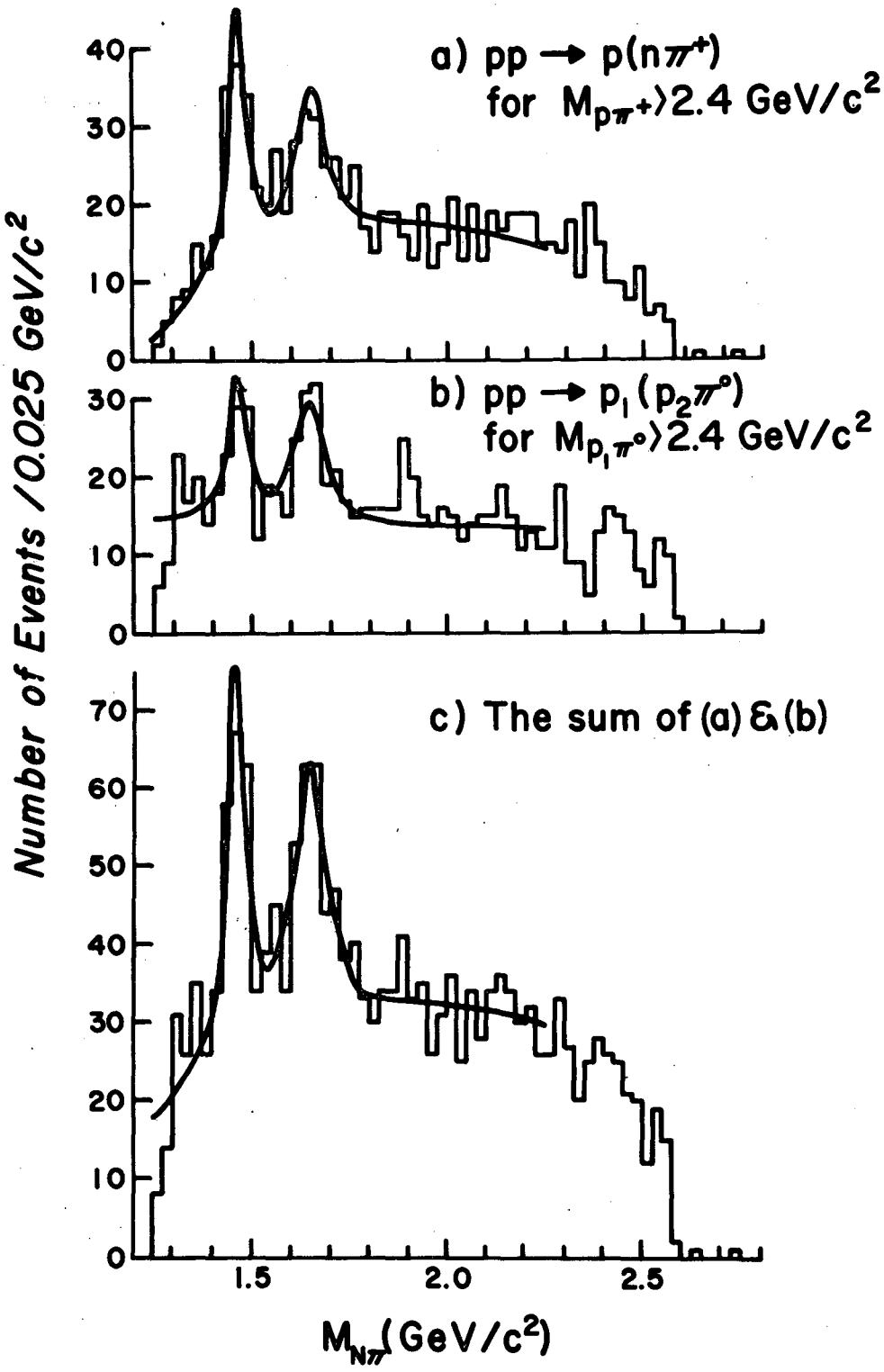

XBL 725-845

FIGURE 36

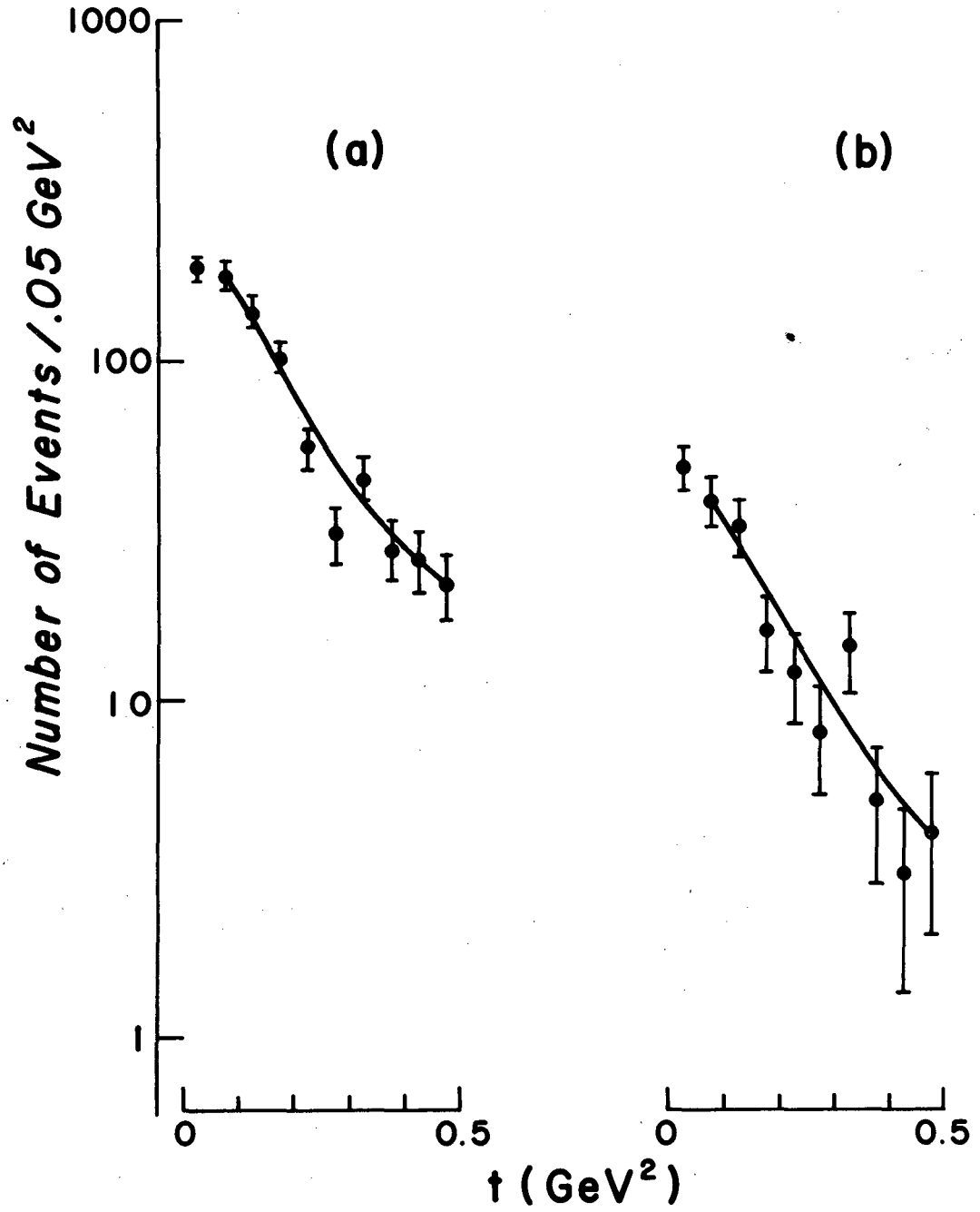

XBL 725-846

FIGURE 37

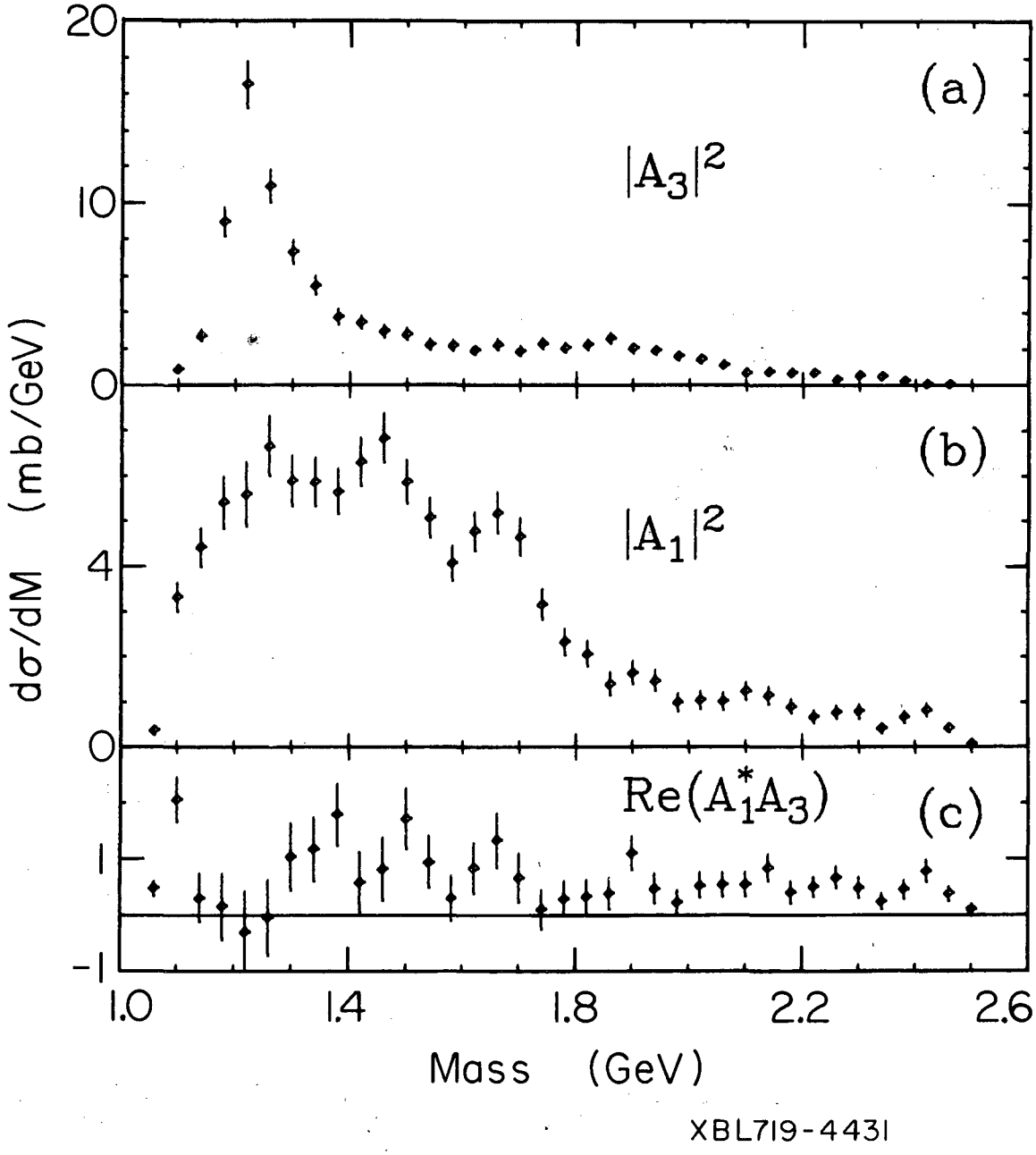
20
10
0
(a)
$|A_3|^2$
(b)
$|A_1|^2$
4
0
$Re(A_1^* A_3)$
(c)
1
-1
1.0
1.4
1.8
2.2
2.6
Mass (GeV)
dσ/dM (mb/GeV)
XBL719-4431

FIGURE 38

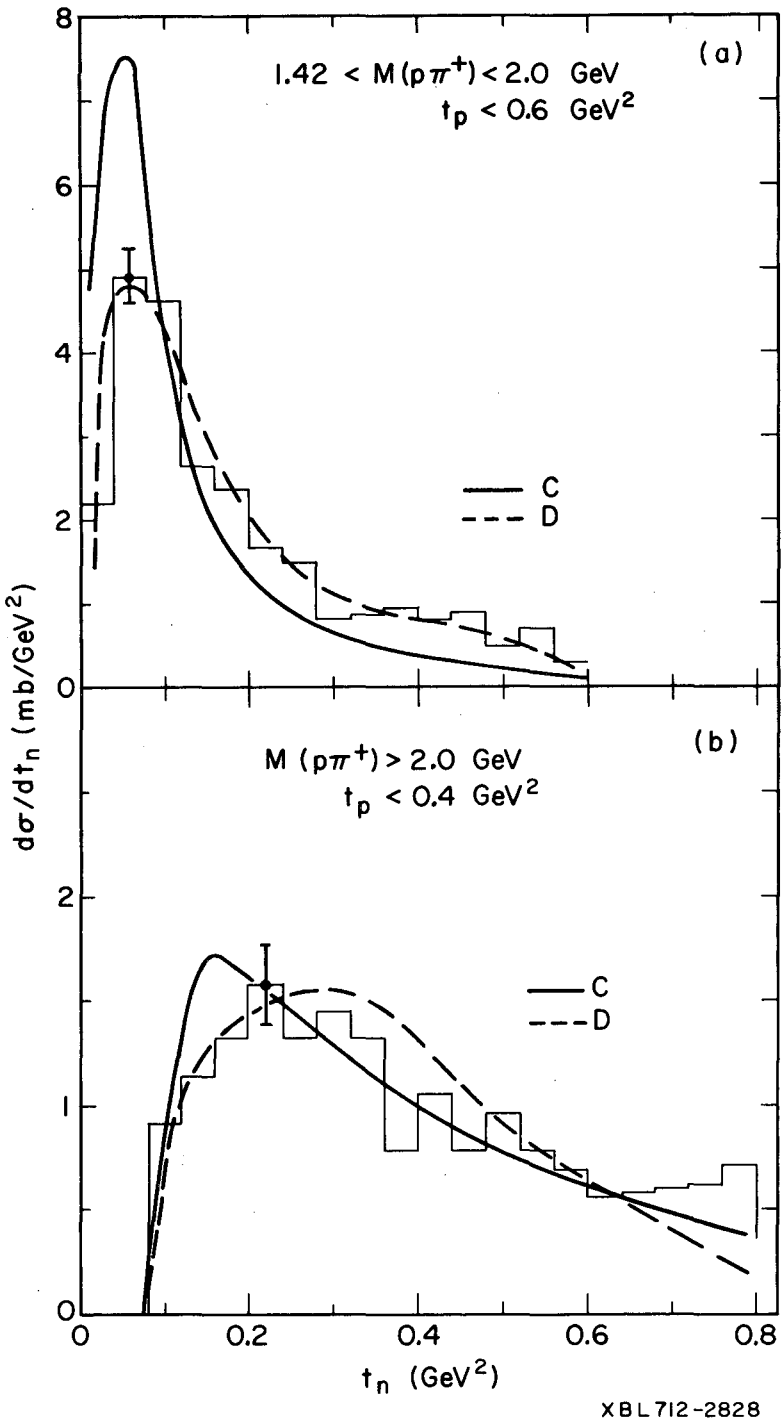
(a)
1.42 < M(pπ+) < 2.0 GeV
tp < 0.6 GeV2
C
D
(b)
M (pπ+) > 2.0 GeV
tp < 0.4 GeV2
C
D
dσ/dtn (mb/GeV2)
tn (GeV2)
XBL712-2828

FIGURE 39

TECHNICAL INFORMATION DIVISION
LAWRENCE BERKELEY LABORATORY
UNIVERSITY OF CALIFORNIA
BERKELEY, CALIFORNIA 94720